Title

The Effect of Extracellular Biophysical Cues on Cellular Signal Processing

Permalink

https://escholarship.org/uc/item/6sq5t7zz

Author

Ou, Guanqing

Publication Date

2016

Peer reviewed|Thesis/dissertation

The Effect of Extracellular Biophysical Cues on Cellular Signal Processing

by

Guanqing Ou

DISSERTATION

Submitted in partial satisfaction of the requirements for the degree of

DOCTOR OF PHILOSOPHY

in

Bioengineering

in the

GRADUATE DIVISION

of the

UNIVERSITY OF CALIFORNIA, SAN FRANCISCO

AND

UNIVERSITY OF CALIFORNIA, BERKELEY

Dedication and acknowledgements

This work is dedicated to my parents, who have been with me every step of the way and to whom I cannot express enough love and gratitude for their support.

The work described here would not have been possible without the support of many people and institutions. As such, I'd like to acknowledge:

--My Ph.D advisor, Dr. Valerie Weaver. Her mentorship and guidance throughout my time in her lab were invaluable to my development as a person and scientist. She is a beacon of enthusiasm and dedication to science and I am indebted to her for all that I have learned during my Ph.D. She supported my interest in tool development and connected me with leaders in the field. She lent her brilliant mind to my set of research interests and continuously pushed me toward greater achievement. She has been my fierce advocate since I joined the lab and for all this I will be eternally grateful.

--The strong network of mentors and collaborators in and outside of the UC-Berkeley/UCSF community. Within our program, I have benefited greatly from interactions with and mentorship under Dr. Sanjay Kumar, Dr. Amy Herr, Dr. Bo Huang, Dr. Tamara Alliston, Dr. Max Krummel, Dr. Sophie Dumont, Dr. Carolyn Bertozzi, Dr. Jay Groves, and Dr. Randy Schekman. At other institutions, I have been lucky enough to work with Dr. Ravi Radhkrishnan at the University of Pennsylvania, Dr. Jim Norman at the Beatson Institute, and Dr. Chris Chen at Boston University. They helped me think through scientific problems, offered new perspectives on research approaches, and provided thoughtful career advice. I look to them as examples of how impactful good mentors can be and I would not have grown as a problem solver without each and every one of them.

--The members of the Valerie Weaver lab. From specialists to postdocs to other graduate students, everyone in the lab helped to create an environment where expertise and insight were shared. These colleagues offered their experience in assay development, validation, and execution, as well endless feedback on experimental design, presentations, and manuscripts. Not only this, many of them contributed scientific expertise to the projects described here. Our particular blend of scientists and engineers exposed me to a variety of perspectives that facilitated the breadth of work I was able to complete during my Ph.D. I want to point out those members who have been especially helpful to me: Matt Paszek, Chris Dufort, Janna Mouw, Laralynne Pryzybyla, Fuiboon Kai, and Jon Lakins.

--Many members of the UCSF community, with whom I've interacted through participation in the Science and Health Education Program, Peer Support Groups, class activities, and research collaborations: Izzy, Alex, Harrison, Annie, Simon, Paul, Tuan, Simon, Freeman, Elena, Rob, my entire orchestra, and John.

--Alisha and Zhenya. They imbued me with a love of mechanobiology and research. They taught me how to read and write papers. They were my introduction to bioengineering and biophysics.

--My friends and family. Amanda, who sat next to me every day for two years. Arash, who was there from the beginning. Claire, who somehow continued along the same course, but we've finally diverged! Keerthik, who was far away and yet never too far. Yifan, who knew what it was like. Alyona, who always knew what to say. Sriya, who cared and loved from afar. And Charles, who supported me and encouraged me, understood and cheered and all the rest. My cousins, who will complete the family of biology Ph.Ds, and again, my parents, who always believed in me.

The Effect of Extracellular Biophysical Cues on Cellular Signal Processing
Guanqing Ou

Abstract

Cell behavior is regulated by both internal and external signals. In early biological research, studies into cell signaling focused on biochemical cues. However, in recent decades, the scientific community has come to recognize the importance of biophysical cues in determining cell fate. The extracellular matrix (ECM), in particular, has emerged as a major regulator of cell behavior and is a source of both chemical and physical cues. Extracellular matrix makeup, organization, and presentation have been implicated in influencing cell growth, migration, differentiation, and more. My doctoral work focused on dissecting the molecular mechanisms underlying biophysical regulation of cell signaling. Specifically, I examined the effect of two biophysical properties of the extracellular matrix—dimensionality and rigidity—on mammary epithelial cell growth and survival signaling. My thesis details work connecting altered ECM properties to changes in the biophysical properties of the cell, which directly influence the context and dynamics of canonical growth factor receptor and GTPase signaling to reprogram cell behavior.

CONTENTS

List of Tables:

List of Figures:

1 INTRODUCTION

Cell behavior and fate is regulated by a complex, dynamic process of cell signaling. Through the process of "signaling", cells parse and process extracellular cues, intracellular genetic programs, and complex interactions among its intracellular components to live, grow, and replicate. The extracellular matrix (ECM) plays an important role in establishing the context in which this signaling occurs.[1-3] In addition to providing physical support for cells, the ECM actively participates in the establishment, separation, and maintenance of differentiated tissues and organs by regulating the abundance of growth factors and receptors, the level of hydration, and the pH of the local environment.[1,4] The makeup, organization, presentation, and mechanical properties of the extracellular matrix are all part of the complex set of cues received and processed by the cell in determining its behavior and fate. Understanding the molecular mechanisms by which this processing occurs is vital to such diverse fields as tissue engineering, cancer biology, and regenerative medicine. My doctoral research has focused on examining how two properties of the ECM—dimensionality and rigidity—influence proliferation and survival signaling in epithelial cells.

In the following chapters, I will first present background on key molecular players in the extracellular matrix, particularly those relevant to mammary and epithelial cell biology. This will be followed a review of existing literature linking matrix dimensionality and ECM stiffness to changing cell behavior, to motivate the specific research questions I asked. The results of my work will be divided into three sections: 1) investigation of how matrix dimensionality mediates cell survival signaling via changes in the mechanical properties of the cytoskeleton and membrane; 2) preliminary studies and tool development for analysis of how changing ECM stiffness alters epidermal growth factor receptor signaling and trafficking; and 3) tool development to facilitate super-resolution imaging on mechanically tunable substrates.

Together, the work I report here represents a step forward in elucidating the precise molecular mechanisms by which a cell processes and transmits information about the properties of the extracellular matrix. I identify two unique ways in which the ECM changes the context in which molecular interactions take place and thus alter cell signaling and fate.

2 THE EXTRACELLULAR MATRIX

KEY MOLECULAR PLAYERS IN THE ECM

Our understanding of the composition, structure and function of the ECM is continuously evolving, aided by the discovery of novel ECM molecules, the mapping of internal sites within ECM proteins that are crucial for self-assembly and for interactions with other ECM components, the characterization of the proteases and the protease inhibitors that are responsible for ECM degradation and turnover, and the identification of novel receptors and signaling mechanisms that mediate cellular responses to the ECM[1–3]. The architecture of the ECM is highly organized, arising partly from the innate properties of its constituent molecules and their interactions, and from the activities of the resident cells. Interactions between cells and the environment created by the ECM in turn play important roles in directing processes in development, homeostasis, and pathogenesis. Here, we define the ECM generally as all secreted molecules that are immobilized outside of a cell, including growth factors, cytokines and cell adhesion molecules, although we will focus primarily on particular macromolecules largely responsible for extracellular structure and architecture.

The protein and non-protein constituents of the ECM vary not only in terms of their functional roles, but also in terms of their structure. The polypeptide chains of ECM macromolecules often consist of numerous individual domains, with even homologous domains between macromolecules having sequence and structural differences that impart different functions. Individual ECM macromolecules rarely exist in isolation but, instead, often integrate into supra structures containing more than one molecular species that differ in both identity and relative abundance. The ECM is composed primarily of two main classes of macromolecules, fibrous proteins (including collagens and elastin) and glycoproteins (including fibronectin, proteoglycans (PGs) and laminin)[1].

Fibrillar collagens. Collagens are major proteins of the ECM and arguably the most dominant. Decades of research have uncovered 28 different collagen types to date, with each type comprised of homo- and

heterotrimers formed by three polypeptide chains (α chains)(Figure 2.1). More than 40 distinct polypeptide chains (α chains) are known in humans, with multiple other proteins containing collagen-like domains[5,6]. The structural hallmark of all collagens is the triple helix, a tight right-handed helix of three α chains, each of which contains one or more regions characterized by the repeating amino acid motif (Gly-X-Y), where X and Y can be any amino acid[7]. Some collagen molecules assemble as homotrimers, while others assemble as heterotrimers, with two or three distinguishable chain types. The increasing family of collagens and proteins with collagenous domains reveal the collagen triple helix to be a basic motif adaptable to a range of proteins and functions. Its rod-like domain has the potential for various modes of self-association and the capacity to bind receptors, other proteins, glycosaminoglycans (GAGs), and nucleic acids.

Proteoglycans. In contrast to the predominantly fibrillar structure of collagens, PGs form the basis of higher order ECM structures around cells. The primary biological function of PGs derives from the biochemical, hydrodynamic characteristics of the glycosaminoglycan (GAG) components of the molecules, which bind water to provide hydration and compressive resistance. As such, PGs are found abundantly in cartilage and neural ECM[8,9]. Proteoglycans are characterized by a core protein that is covalently linked to GAGs — long, negatively-charged, linear chains of disaccharide repeats. They are currently classified into subtypes based on the structure of these GAG carbohydrate chains, as well as the distribution and density of these chains along the core protein[10,11]. Major GAGs include heparin sulfate (HS), chondroitin sulfate (CS), dermatan sulfate (DS), hyaluronan, and keratin sulfate (KS) (HS and CS structures are shown in Figure 2.2d)[10,12–14].

a Standard collagen molecule

1 — N terminal propeptide | Gly-X-Y repeats | C terminal propeptide

3 α chains (2 α1, 1 α2)

2 — C-terminal propeptide initiates triple helix formation in the rough ER

3 — Procollagen — Procollagen is secreted into the extracellular space

4 — Collagen — Enzymes cleave propeptides to form collagen

b FACIT and related collagens

Gly-X-Y interruption

Non-collagen
Collagen

Figure 2.1. Collagen structure.

a) *The standard fibrillar collagen molecule is characterized by amino- and carboxy-terminal propeptide sequences, which flank a series of Gly-X-Y repeats (where X and Y represent any amino acids but are frequently proline and hydroxyproline) (step 1). These form the central triple helical structure of procollagen and collagen. Three α-chains (the illustration shows two α1-chains and one α2-chain, which is representative of type I collagen) are intracellularly assembled into the triple helix following initiation of this process by the C-terminal domain (step 2). Procollagen is secreted by cells into the extracellular space (step 3) and converted into collagen by the removal of the N- and C-propeptides via metalloproteinase enzymes (step 4).*

b)| Fibril-associated collagens with interrupted triple helices (FACIT) and related collagens have a different structure to standard fibrillar collagen; they contain non-collagenous regions — that is, non-triple helical sequences. These lead to kinks in the resulting macromolecular structure that straighten under small strains.
*Figure part **a** is modified, with permission, from REF 135 © 2012 Fan et al.; licensee BioMed Central Ltd, and from REF. 136, Klug, William S.; Cummings, Michael R., Concepts of Genetics, 5th Edition, © 1997. Reprinted by permission of Pearson Education, Inc., Upper Saddle River, NJ. Figure part **b**: this Figure was originally published in Biochem. J. Jäälinoja, J., Ylöstalo, J., Beckett, W., Hulmes, D. J. S. & Ala-Kokko, L., Trimerization of collagen IX alpha-chains does not require the presence of the COL1 and NC1 domains. Biochem. J. 2008; 409: 545–554 © the Biochemical Society.*

Heparan sulfate proteoglycans (HSPGs) are a major part of the basement membrane, a type of ECM structure (see next section for description). Their GAG chains are comprised of highly sulfated chains of hexuronic acid and d-glucosamine disaccharide repeats. HSPGs can be cell-surface bound, like syndecans and CD44v3, glycophosphatidylinositol (GPI)-linked, like glypicans, or secreted ECM proteins, like agrin, collagen XVIII and perlecan[15]. Variety in HSPGs is introduced through splice isoforms that control GAG chain lengths, the spacing of GAG chain attachments, and the extent of sulfation and epimerization of the sugars within the GAG chains[14,15]. Resulting PGs exhibit different binding affinities for molecules within the ECM. Fibroblast growth factors (FGFs), for example, are particularly sensitive to the spacing and sulfation of GAG chains on HSPGs[16]. HSPGs have high negative charges that allow them to easily bind other proteins, including growth factors like fibroblast growth factor (FGF), chemokines, other ECM proteins like laminin and fibronectin, and cell-surface receptors[15,17,18]. As such, they have been implicated in regulating many cellular processes, including cell growth and migration[15,19,20].

Chondroitin sulfate proteoglycans (CSPGs) can be found in cartilage and neural ECM. CSPGs are functionalized with sulfated polysaccharides with repeating disaccharides of glucuronic acid and *N*-acetylgalactosamine[20]. Lecticans, also called hyalectins, are the most common CSPGs in the neural ECM[20,21]. This family consists of four members: aggrecan, neurocan, veriscan and brevican[13,21]. The core protein is highly homologous across lecticans, which are characterized by globular domains at both the N- and C-terminal ends. Lecticans contain binding domains for hyaluronic acid (HA, a common glycosaminoglycan in cartilage and the nervous system), lectins, and growth factors[8,21,22]. As with HSPGs, alternative splicing and different densities of GAG chains on the core protein leads to significant variations in the properties of these proteins[8].

In addition to being dominant components of the ECM, proteoglycans can also serve as accessory proteins in tissues rich in other matrix proteins. The small leucine-rich repeat proteoglycans (SLRPs), for instance, are a family of proteoglycans that have been implicated in fibrillar collagen assembly[23]. All SLRPs have

two regions—a variable N-terminal domain that contains sulfated tyrosines or acidic amino acid residues and a conserved C-terminal containing the leucine-rich repeats (LRRs) for which the family was named (Figure 2.2c)[23,24]. These core proteins can then be functionalized with GAG chains[23]. The LRRs contain collagen-binding regions and have been well characterized owing to this property, while the function of the N-terminal domains is less extensively understood[23]. Elucidation of the crystal structure of decorin suggests that these N-terminal domains act as a capping mechanism, whereby cysteines within this domain form disulfide bonds that link back to the C-terminus via leucines in the consensus sequence[25].

So far, five classes of SLRPs have been established, and each class is distinguished by their homology on the protein and genomic levels, the presence of N-terminal cysteine-rich clusters, and chromosomal placement. Classes I-III are so-called "canonical" classes, distinguished by the relative abundance of data describing the function and localization within the body, while IV-V have only been recently described and are associated with many unanswered questions about their function. A full listing and description of SLRPs is beyond the scope of this Review, but such information can be found in references[26,27]. The Class I SLRPs decorin and biglycan have been extensively studied and participate in collagen fibrillogenesis[9,28]. Not only do these proteins facilitate the formation of collagen fibrils, they also regulate fibril width and growth through mechanisms that have not been fully elucidated[27]. In addition to their roles as structural proteins in ECM assembly, SLRPs are considered "active" members of the ECM and participate in cell signaling. Recently, binding sites for growth factors, cytokines, and ECM proteins other than collagen have been found on SLRPs[24].

CONNECTORS IN THE ECM

Collagen, proteoglycans, and HA represent major structural components within the extracelluar matrix. They provide much of the supportive framework within which other ECM components and cells interact. Additional ECM components, such as laminin or fibronectin, act as bridges between structural ECM molecules to reinforce this network, as well as to connect the ECM to cells and soluble molecules within

the extracellular space. These connectors tend to be multi-domain glycoproteins that contain binding motifs for other ECM proteins, growth factors, and cell-surface receptors.

Laminins. Laminins are a family of large, mosaic glycoproteins composed of globular, laminin type EGF-like repeats and α-helical domains (Figure 2.2a). They are primarily located in basal lamina and some mesenchymal compartments. Interactions between modular domains within the laminin molecule and other proteins allow laminins to mediate interactions between cells via cell-surface receptors (such as integrins and dystroglycan) and other components of the ECM (such as nidogens, perlecans and collagens) (Figure 2.2a)[29].

Laminins consist of $\alpha, \beta,$ and γ chains that combine via the triple α-helical coiled-coil domain in the center of each chain to form structures with a cruciform (cross-shaped), Y-shaped (three arms), or rod-shaped (single arm) structure[29] (Figure 2.2a). Different chain isoforms combine to generate distinct assembled heterotrimers[29]. These laminins are described by their combined chain numbers; for instance, $\alpha1\beta1\gamma1$ is known as laminin 111. This nomenclature was preceded by single number assignments, when there were fewer known isoforms. The original designations remain preferred in some settings, so it is possible to find references to laminin-5 ($\alpha3A\beta3\gamma2$), for instance. For a useful table that cross-references these different systems, see [30]. So far, five α (α1-α5), four β (β1-β4), and three γ (γ1-γ3) chains are known, and they combine to form 16 different laminin heterotrimers[30,31] Although laminin 111, for instance, has been shown to self-assemble into aggregates, laminins primarily serve as bridges between other molecules[32,33].

Fibronectin. Many of the previously described ECM proteins interact with cells through crucial connections with the multidomain protein fibronectin (FN) to regulate cell adhesion, migration, and differentiation[34]. FN is secreted as a large ECM glycoprotein that assembles via cell-mediated processes into fibrils and meshed structures around cells[35]. Each fibronectin subunit consists of three modules of

repeating units, each of which has distinct structures: type I hexagons, type II squares, and type III cylinders (Figure 2.2b)[34,35] These modules contain binding motifs that are important in facilitating the interaction of fibronectin with cell-surface receptors like integrins, collagen and gelatin, and intramolecular units that facilitate self-assembly of the molecule[35,36]. Intramolecular disulfide bonds between each type I and type II module stabilizes the FN subunit's folded tertiary structure and fibronectin dimers form via antiparallel disulfide bonds at the C-terminus[35].

Fibronectin fibril assembly involves interactions between its RGD and synergy binding sites with cell-surface receptors (e.g. integrins)[34,35,37]. Initial binding between fibronectin dimers and integrins leads to the activation and clustering of these receptors[35]. Integrin clustering is thought to promote further FN-FN intermolecular interactions and tethering of FN molecules to the cell surface allows cell-mediated contractility to exert force on FN and change its conformation[34]. This change in conformation exposes cryptic binding sites within the FN molecule and also allows it to take a form more conducive to self-assembly and packing. The maturation and movement of fibrillar adhesions within the cell is thought to guide the formation of FN fibrils[35,38]. Generation of force along these adhesions further shape the assembly FN network and maturation of multiple clusters of integrin-based adhesions bring nascent FN bundles together to form a larger structure[35,38].

In addition to the key molecular players we have described here, the ECM is composed of many other classes of macromolecules. I have chosen only to highlight those that are abundant in mammary tissue, or that are key to formation of basal lamina. For brief descriptions of other macromolecules, their chemical makeup, and where in the body they may be found, as well as excellent references that may enrich the readers' understanding of these important components, please refer to reference [39].
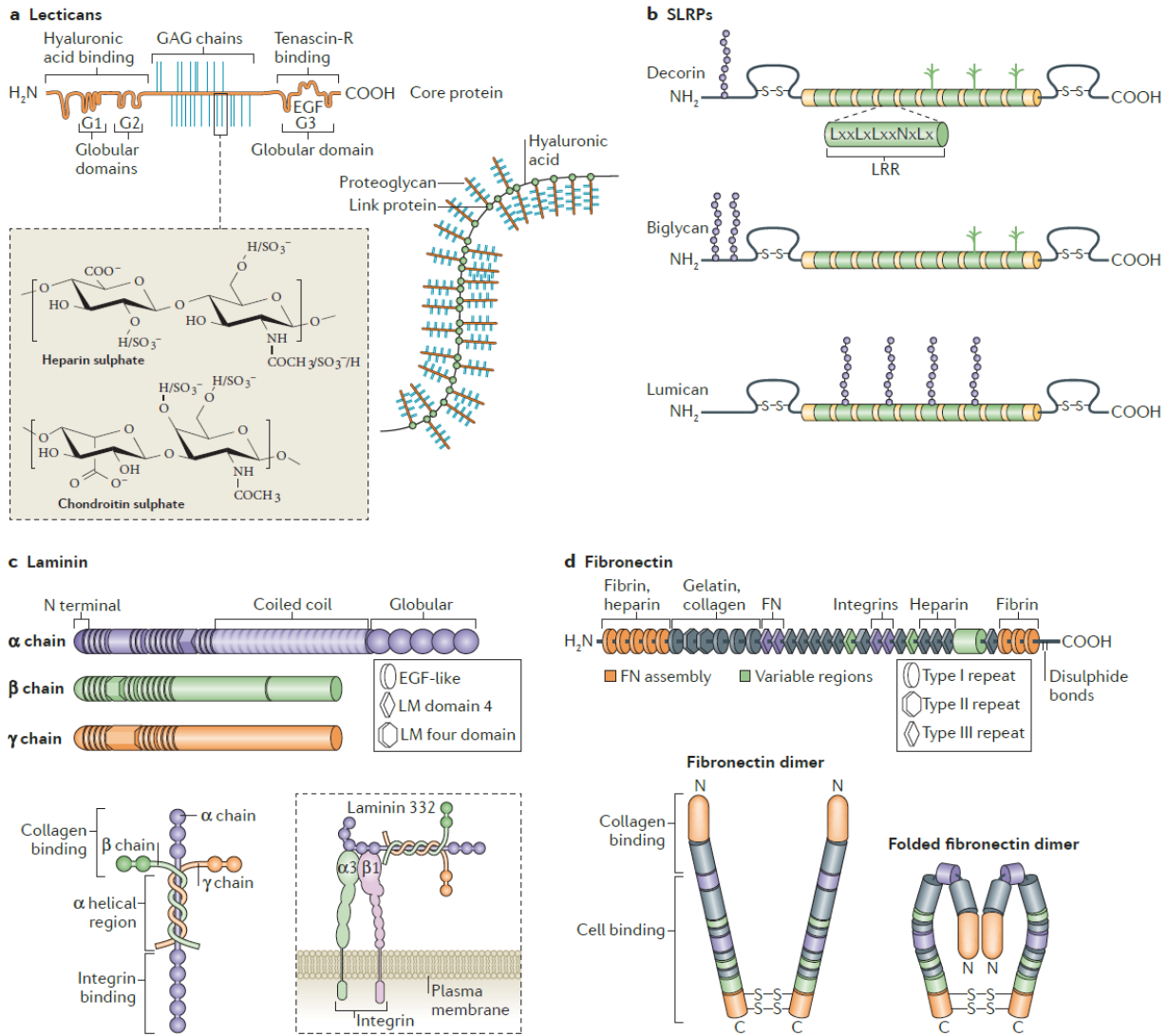
Figure 2.2. Non-collagenous molecules of the ECM.

*Lecticans (aggrecan is shown; part **a**) and small leucine-rich repeat proteoglycans (SLRPs; decorin, biglycan and lumican are shown; part **b**) are major proteoglycans (PGs). The SLRPs are characterized by differences in their amino terminus structure and highly conserved leucine rich repeats (LRR) in the core molecule. Lecticans have a core protein with binding domains for glycosaminoglycan (GAG) chains flanked by globular domains that interact with hyaluronic acid (at the N terminus) and tenascin R (at the carboxy terminus). Common GAGs include chondroitin sulphate and heparan sulphate, the chemical structures of which are depicted.*

*The assembled bottle-brush-like aggrecan–link protein–hyaluronic acid structure is shown. Laminins are formed by the incorporation of α, β and γ chains into a cruciform, Y-shaped or rod-like structure (part **c**). These chains are characterized by different domains, as shown. The domain structures depicted represent only one isoform for each chain type, but major differences between the basic composition of the chains (such as the lack of globular regions in β and γ chains) are also present in the other isoforms. Laminins interact with cell surface receptors, such as integrins, primarily through globular domains in the chain. Fibronectin domain structure and the domains to which extracellular matrix (ECM) molecules and cell surface receptors bind are indicated (part **d**). The fibronectin molecule forms a dimer through disulphide bonds on its C terminus. The folded fibronectin molecule forms via ionic interactions between type III domains of neighbouring molecules and is deformed by mechanical force to reveal cryptic binding sites for other fibronectin molecules and cell surface receptors when interacting with cells.*

11

3   MATRIX DIMENSIONALITY AND ITS EFFECTS ON CELL BEHAVIOR

The following chapter has been adapted from previously published work: Ou G[*], Rubashkin MR[*], Weaver VM. Deconstructing signaling in three dimensions. *Biochemistry* **53** (2078-2090), 2014.

Matrix Dimensionality and "3D"

Cells *in vivo* exist within the context of a multicellular tissue, where their behavior is governed by homo- and heterotypic cell−cell interactions, the material properties of the extracellular matrix, and the distribution of various soluble and physical factors. Most methods currently used to study and manipulate cellular behavior *in vitro*, however, sacrifice physiological relevance for experimental expediency. The fallacy of such approaches has been highlighted by the recent development and application of three- dimensional culture models to cell biology, which has revealed striking phenotypic differences in cell survival, migration, and differentiation in genetically identical cells simply by varying culture conditions. These perplexing findings beg the question of what constitutes a three-dimensional culture and why cells behave so differently in two- and three-dimensional culture formats. In the following section, I dissect the fundamental differences between two- and three-dimensional culture conditions. I begin by establishing a basic definition of what "three dimensions" means at different biological scales and discuss how dimensionality influences cell signaling across different length scales. I identify which three-dimensional features most potently influence intracellular signaling and distinguish between conserved biological principles that are maintained across culture conditions and cellular behaviors that are sensitive to microenvironmental context. Finally, I highlight state-of-the-art molecular tools amenable to the study of signaling in three dimensions under conditions that facilitate deconstruction of signaling in a more physiologically relevant manner.

It is important to begin this discussion of signaling in three dimensions ("3D") by defining what constitutes 3D. To understand 3D, it is helpful to first define "2D", which has most frequently been used to refer to monolayer culture of cells plated on polystyrene or glass surfaces. On these conventional 2D substrates, the cell interacts with a basal extracellular "matrix" and with neighboring cells via lateral cell-cell junctions. Due to equal exposure to the bulk culture medium, there is assumed to be uniform nutrient distribution. The term "3D" was initially used to contrast 3D culture from monolayer culture. In one definition, 3D culture consists of a cell embedded within and surrounded by an extracellular matrix, such

that the cell is able to encounter its extracellular microenvironment within a 3D volume of space.[40] Another definition suggests 3D refers to the specific topological features and 3D organization of the extracellular matrix.[41,42] One common feature of these systems is the exposure of the cell to matrix and/or cell-cell interactions in all directions. Regardless, early studies using these various 3D culture systems demonstrated dramatic differences in cell behavior and signaling between cells grown in 2D versus 3D. Cells in 3D respond differently to exogenous growth factors and are highly resistant to apoptosis.[43,44] Consistently, gene expression in a variety of cells types, including glomerular, endothelial, and melanoma cells, is altered in 3D culture.[45–47] Moreover, cell-matrix adhesions in 3D can be composed of different proteins from those in 2D, resulting in altered metabolic activity and nuclear architecture.[41,48,49] These observations suggest that the cells undergo a profound but systematic rewiring when they transition from a 2D to a 3D context. However, while these experimental observations emphasize how cellular context can profoundly modify a plethora of cellular behaviors, the precise mechanism by which dimensionality induces these changes is unclear. Indeed, "3D" can mean different things at different biological scales. Within a cell, 3D is felt through changes in cell shape and volume, in the organization of the cytoskeleton and in the distribution of signaling components throughout the cell. At the cellular level, 3D means that the cell is exposed to stimuli on all sides, whether from the ECM or neighboring cells. On a multicellular level, 3D manifests in the structural organization of units like lobules, ducts, and vessels. These factors all influence the manner in which signaling takes place in distinct ways, as overviewed in Figure 3.1. In the following review, we discuss how signaling is influenced by dimensionality at each of these scales and highlight novel tools to aid in further elucidation of these relationships.
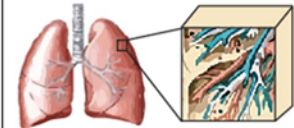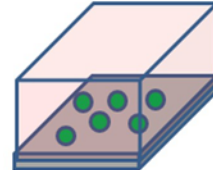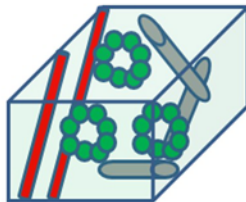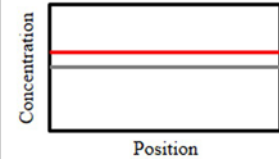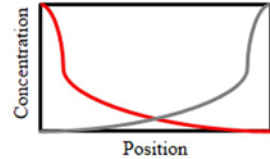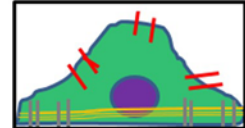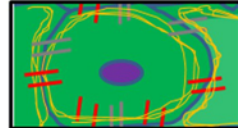
Figure 3.1. Comparison of 2D vs 3D.

The environment in which the cell is cultured differs dramatically between 2D and 3D.

Conventionally, signaling events within the cell are modeled as concentration-dependent biochemical reactions. This paradigm assumes that signaling molecules are freely diffusing and uniformly distributed in the cytoplasm and has resulted in a "whole-cell" perspective on signaling, where the cell is considered the reaction vessel in which given concentrations of signaling molecules react with each other. A large body of evidence has arisen to suggest, however, that the localization of a specific signaling molecule within a cell greatly impacts the magnitude and the effect of the resultant signaling event.[50,51] Signaling molecules can be constrained in space by barriers to free diffusion, scaffolded into multi-protein complexes, or tethered to 2D membranes. Each of these situations significantly alters the diffusivity of signaling molecules, which in turn changes the frequency, speed, and duration of biochemical reactions.

Barriers to Diffusion: Scaffolding Proteins

Scaffolding proteins can nucleate large, multi-protein complexes that accelerate reaction kinetics. By bringing multiple components of a signaling cascade together, these proteins alter the reaction kinetics governing a specific signaling cascade. β-arrestin, for example, can bind several components of the MAPK pathway, including RAF, MEK, and ERK.[52,53] By clustering these proteins, β-arrestin eliminates RAF-MEK binding as a rate-limiting step. Following MEK sequestration by β-arrestin, MEK phosphorylation by RAF occurs at a constant rate.[52] Physiologically, *β*-arrestin enhances ERK activation downstream of growth factor receptor signaling by prolonging RAF-MEK-ERK interaction time in the cytoplasm.[52,54]

Similarly, paxillin serves as a scaffold for proteins at sites of integrin mediated cell-matrix adhesions. These adhesion complexes connect the cytoskeleton to proteins within the extracellular matrix (ECM) and are critical sites for transduction of mechanical inputs to intracellular signaling.[55] Notably, activated paxillin increases the frequency of interaction between protein kinases such as focal adhesion kinase and Src, which can control downstream Rac activity and increase cell motility.[56,57] Thus, paxillin mediates mechanotransduction by connecting adhesion proteins with signaling pathways governing motility and proliferation.

Scaffolds can also serve to reduce signaling in specific pathways. LKB-1 interacting protein 1 (LIP-1) is a scaffolding protein that sequesters the transcription factor Smad4 from binding to TGFβ or BMP promoter sequences, thereby acting as a tumor suppressor.[58] Depending on availability, scaffolding proteins may serve either enhancing or inhibitory functions. An elegant example of this may be found in the MAPK pathway. Kinase suppressor of Ras-1 (KSR1) can scaffold all members of the MAPK cascade.[59,60] Titrating KSR1 concentration reveals its cooperative role in the pathway until a certain threshold is reached, after which the concentration of scaffolding protein exceeds "signaling-competent complexes" and sequesters individual proteins from interacting with others in the cascade.[53] In general, however, there is no doubt scaffolding proteins influence signal transduction kinetics by altering the interaction dynamics of signaling components.

Barriers to Diffusion: The Cytoskeleton

When cells are in a 3D environment, the cytoskeleton is usually non-uniform in shape and composition. For example, cells in collagen matrices often exhibit actin cytoskeleton alignment with fibers within the ECM.[61,62] Changes in cytoskeletal organization, in turn, influence intracellular signaling by acting as barriers to diffusion. The cytoskeleton can be a passive barrier, where increased cross-linking represents more obstacles to free diffusion. Computational molecular models have predicted that components of the MAPK, protein kinase A (PKA) and PI3K-Akt-mTOR pathways have reduced diffusion due to increased molecular crowding.[50] Alternatively, cytoskeletal proteins can act as scaffolds to promote or inhibit interaction of signaling molecules. Nanoclustering of epidermal growth factor receptor (EGFR) at the cell periphery can be due to high actin activity at these sites.[63] Altered clustering and diffusion of receptor tyrosine kinases has been proposed as a molecular mechanism employed by cells in 3D environments to resist drug therapies, such as resistance to HER2 targeting agents in breast cancer via increased HER2 dimerization in 3D.[64,65] Thus, external stimuli leading to changes in actin density can alter the spatiotemporal behavior of intracellular signaling.

Altered Dimensionality: Membrane Sequestration

In some cases, transition from 3D diffusion in the cytoplasm to 2D diffusion in a membrane can enhance cellular signaling. A good example of this is given by the BCL-2 family of proteins, which mediate caspase-driven apoptosis by regulating cytochrome c release from mitochondria.[66] Bax, a BCL-2 protein typically found freely diffusing in the cytoplasm, activates mitochondrial membrane permeabilization via oligomerization. When cytokine activation of apoptosis occurs, Bax is recruited to the mitochondrial membrane surface via upstream signaling events.[67] When Bax is in the cytoplasm, diffusing in a 3D environment, the probability that it will oligomerize with itself is quite low to negligible. However, once it is limited to 2D diffusion in the mitochondrial membrane, the likelihood of interaction with other Bax proteins also anchored in the membrane greatly increases.[67] This leads to Bax oligomerization, release of cytochrome c, and progression of apoptotic signaling.

Novel Tools for Characterization of Spatial Control of Signaling
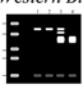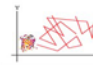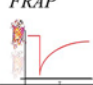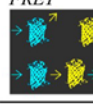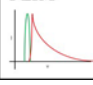
As can be seen, the spatial organization of signaling molecules can greatly impact the dynamics of intracellular signaling. Moreover, there are many mechanisms by which the molecular localization can be affected. Traditional biochemical assays like Western blots and ELISAs lack the subcellular resolution to capture this information (Table 4.1A). Electron microscopy has long been used to characterize the molecular organization of the cytoskeleton, membranes, and organelles in 2D and 3D, including changes in epithelial cell structure after hormone stimulation or altered mechanical properties of the ECM [68–70] (Table 4.1B). However, 3D samples must be fixed, dehydrated, and sectioned, prohibiting studies of spatial or temporal dynamics of cells in 3D environment. Light microscopy, on the other hand, is highly conducive to characterizing how protein localization influences cellular signaling. To empirically determine the diffusion coefficients and dissociation constants, fluorescence recovery after photobleaching (FRAP) can be used. FRAP involves tagging a protein of interest with a fluorescent molecule, taking an image of the basal fluorescence level, photobleaching a specific area of interest with high intensity laser illumination, then quantifying the recovery in fluorescence in intensity as unbleached molecules switch places in the area

of interest with the bleached molecules (Table 4.1D). FRAP is a technique that can be used to measure the ensemble change in protein behavior at a region of interest and has been used to great advantage to determine the binding kinetics of transcription factors and the mobility of receptors in the plasma membrane (Table 4.1E).[71,72]

To study protein-protein interactions, techniques like Förster Resonance Energy Transfer (FRET) and Fluorescence-Lifetime Imaging Microscopy (FLIM) can be used. FRET imaging involves using the energy transfer between fluorophores as a proxy for distance between fluorescently tagged molecules; it is sensitive within the 5-10nm range and is often used as an indication of protein-protein binding (Table 4.1E). FRET has been used to study receptor-ligand binding at the membrane as well as protein conformation.[73,74] Grashoff *et al.* demonstrated the use of an intramolecular FRET probe that allowed detection of vinculin stretching under cytoskeletal tension.[75] FLIM, on the other hand, takes advantage of the sensitivity of a fluorescent molecule's lifetime—the exponential rate of decay of its fluorescence—to its environment to characterize protein-protein interactions. Unlike FRET or FRAP, which require a genetically encoded probe or fluorescent antibody, FLIM can use the inherent fluorescence of specific molecules such as NADPH or collagen and is a promising technique for analysis of unmodified and untagged human cancer cells in the future(Table 4.1F).[76]

The impact of 3D and subcellular distribution of signaling molecules on intracellular signaling is not often discussed despite the fact that localization can profoundly affect cell and tissue behavior and fate. Nonetheless, as new technologies that allow us to peer into the cell emerge, the need to understand the role of protein localization in signaling cannot be ignored.

Table 3.1. Quantitative Techniques for Determining Reaction Kinetics.

	Experiment	Methodology	Sample Needed	Scale Context	Temporal Dynamics	Spatial Dynamics	3D Amenable	Experimental Constraints	Materials / Cost
A	*Western Blot*	Biochemical, antibody	~10^6 Cells	Tissue				Difficult to analyze membrane proteins, cross-reactivity of antibodies	Chemi-luminescent imager - $
B	*Electron Microscopy*	Microscopy of endogenous structure or antibody-Au	~100 Cells	Submolecular			√	Dehydration is standard, but liquid imaging in special environmental chambers is possible	Scanning or Transmission Electron Microscope - $$$
C	*Single Molecule Tracking*	Microscopy of GEP (genetically encoded probe), Quantum Dot	10-1000 labeled proteins per cell	Single Protein	√	√		Low signal to noise ratio, restricted to molecules at the plasma membrane	Total Internal Reflectance Microscope (TIRF) - $$$
D	*FRAP*	Microscopy of antibody/GEP	>10000 labeled proteins per cell	Subcellular	√	√	√	Laser damage to protein of interest and entire cell	Laser Scanning Microscope - $$$
E	*FRET*	Microscopy of antibody/GEP	>10000 labeled proteins per cell	Subcellular	√	√	√	1-10nm resolution,	Widefield Micrscope - $$
F	*FLIM*	Microscopy of endogenous structure/ antibody/GEP	>10000 labeled proteins per cell	Subcellular	√	√	√	Special cases: No antibodies or GEP	Pulsed Laser Microscopy - $$$$

THE CELL IN 3D—CELL AND MATRIX INTERACTIONS

As we zoom out to examine the cell, we must consider it in its natural context. Within the body, cells interact in 3D with the extracellular matrix (ECM) and neighboring cells. Through these interactions, cells gather information about their surroundings, which is integrated to determine cell behavior and fate. In addition, a cell's 3D environment affects the organization of intracellular components and thus the context in which signaling occurs. This section will feature how intracellular signaling is dependent on the context of cell shape, barriers to intracellular diffusion, and protein localization.

Adhesions and Junctions: Gathering Information from the Environment

Cell adhesion to the external environment can dictate cell shape, growth, proliferation, and apoptosis signaling.[77,78] Cells attach to neighboring cells and to ECM molecules, including secreted proteins (i.e. collagens and laminins), proteoglycans (heparin and chondroitin sulfate), and glycosaminoglycans (hyaluronic acid). Cells attach to these extracellular molecules via a plethora of adhesion receptors, including integrins, cadherins, selectins, discoidin receptors, and syndecans.[79–81] These adhesion receptors bridge the connection between the extracellular environment and the intracellular cytoskeletal and signaling machinery.

Engagement of the ECM in all three dimensions, compared to only at the basal side of cells as in conventional culture, significantly influences cell behavior. Depending on whether cells are cultured in 3D vs. 2D, a cell's response to a given signal can be significantly altered.[49,82,83] Mammary epithelial cells with intact cell-cell junctions in 3D hydrogels are more resistant to apoptosis inducing factors like tumor necrosis factor alpha (TNF-α) when compared to cells in 2D or cells in 3D lacking cell-cell junctions.[49] This resistance highlights the importance of cell-cell interactions in 3D and implies a connection between adhesion-dependent signaling and intracellular signaling directing cell fate.[49] Culture in 2D vs. 3D also alters cell spreading and traction force.[83] When fibroblasts are plated onto closely spaced small pillars (5um), cells form adhesions on the top and side of the pillars, simulating a 3D environment.[83] Under these conditions, fibroblasts pull with high levels of force on the external environment.[83] Conversely, if the cells

are on pillars with increased surface area (15μm) that are widely spaced, simulating a 2D environment, cells do not form adhesions on the sides of the pillars and traction on the external environment is decreased.[83]

The dimensionality, rigidity, and topology of the external environment have been implicated as a regulating factor in cytoskeleton assembly and metabolism.[82] Through the use of polymeric hydrogels, researchers can control rigidity by altering the ratio of crosslinker to monomer ratio in the gel solution. When fibroblasts are seeded in 3D silicone microwells of varying stiffness, they exhibited a range of novel behaviors compared to 2D environments. In soft 3D environments, fibroblasts downregulate actin filament assembly and upregulate mitochondrial activity, in contrast to in compliant 2D, stiff 2D, or stiff 3D environments.[82]

Altered Extracellular Context Leads to Cytoskeletal and Membrane Reorganization

Many of the affected cell behaviors associated with 3D culture have been attributed to altered cell shape. Altered cell shape leads to reorganization of the cytoskeleton as well as changes to membrane tension, curvature, and composition, changing the context in which intracellular signaling takes place.

Cell shape directly influences the organization of the cytoskeleton, which can have profound effects on intracellular signaling. In mesenchymal stem cells (MSC), cell spreading leads to RhoA activation of Rho activated kinase (ROCK), myosin light chain kinase phosphorylation, elevated myosin contractility, increased traction forces to the external environment, and differentiation to an osteoblast phenotype.[84] Conversely, if MSCs are rounded or express a dominant negative RhoA, these cells differentiate into an adipocyte phenotype.[84,85]

Cell shape, in combination with ECM stiffness, governs membrane properties like curvature and tension.[86,87] These characteristics of the plasma membrane, in turn, determine membrane composition, membrane protein distribution, and intracellular trafficking rates.[87,88] Several families of proteins, including the FERM (4.1 protein, Ezrin, Radixin, and Moesin) and BAR (Bin/amphiphysin/Rvs) domain proteins,

have molecular motifs that are sensitive to membrane curvature. Proteins containing these domains, which include the ARF (adenosine-ribosylation factor) family,[89,90] small GTPases like Rac,[89,91] and guanine exchange factors,[92] can assemble multi-protein complexes and preferentially target these complexes toward a curve membrane, thereby affecting protein localization and signaling. Similarly, membrane tension is a key regulator of endo- and exo-cytosis.[87,88] Increased membrane tension decreases the probability of vesicular budding and favors exocytic merging of vesicles with the plasma membrane.[88] This affects the overall balance of vesicular trafficking within the cell, which can influence such diverse signaling pathways as growth factor receptor signaling, reactive oxygen species production, and phagocytosis.

The composition and organization of the plasma membrane is different between 2D and 3D, including cholesterol and sphingomyelin content and organization.[93] This membrane reorganization can alter the distribution of lipids and lipid rafts in the membrane.[84,94,95] These differences can then affect lipid-dependent signaling, such as signaling through the PI3K-Akt-mTOR pathway, which regulates cell metabolism, migration, and apoptosis.[96] The PI3K-Akt-mROR pathway is initiated by phosphatidylinositol 3-kinase (PI3K) recruitment to the membrane and the generation of lipid rafts with phosphatidylinositol-3,4,5-trisphosphates (PtdIns(3,4,5)P_3 and is attenuated by phosphatase and tensin homolog (PTEN).[97] PI3K and PTEN are usually sequestered in distinct lipid groups in the membrane which display limited diffusion and mixing between lipid rafts.[98] This lipid raft-induced segregation of PI3K and PTEN is exacerbated in spread cells, where increased adhesions lead to lipid raft formation in the plasma membrane via microtubules and Arf6 recycling.[99] When cells are rounded via cytoskeletal disruption or via micropatterned surfaces, lipid rafting is decreased, PI3K and PTEN interactions are increased and PI3K signaling is attenuated.[100,101] When cells are spread and PtdIns(3,4,5)P_3 lipid rafts are present, downstream Akt activity leads to differences in BCL-2 mediated apoptosis and cell migration.[101,102]

When cells transit from a rounded to spread morphology, the Rnd family of proteins is targeted to lipid rafts via the KERPA (Lys-Glu-Arg-Pro-Ala) sequence at their N-terminus.[103] Rnd proteins recruit p190RhoGAP to lipid rafts at the plasma membrane, leading to increases in Rho activity that is mediated

by filamin cross-linking of the actin.[103,104] This behavior can be ablated through inhibition of actin polymerization and filamin dependent actin crosslinking.[104]

The pattern of cell-ECM and cell-cell adhesions can dictate the landscape in which other signaling molecules may interact on the cell membrane. Ephrin signaling, for example, is sensitive to the spatial organization of ephrin receptors on the cell membrane.[105] Salaita *et al.* restricted ephrin receptor diffusion in the membrane and showed obstacles to receptor oligomerization and dramatically influence intracellular signaling. Specifically, limiting ephrinA1 movement led to changes in cytoskeletal organization and metalloprotease secretion in cancer cells.[106] As many membrane-bound proteins act by forming protein complexes, the organization of adhesions on the cell membrane can greatly influence the dynamics of these signaling events.

Adhesions and Junctions: Mediating Cell Response to Dynamic Input

In addition to transducing static information about its environment, adhesion molecules can mediate dynamic cellular responses to external input. In 3D environments like the lumen of a blood vessel, signaling at endothelial cell-cell and cell-ECM junctions regulate vessel integrity and leukocyte extravasation from the vasculature. Upon application of fluid shear stress in vitro, endothelial cells in culture undergo filamentous actin and focal adhesion remodeling in the direction of flow in a VE-cadherin dependent manner.[107,108] Downstream, this results in Rho GTPase activation, which works in conjunction with vascular endothelial growth factor receptor 2 (VEGFR2) to activate p38 MAPK pathway activity.[109,110] Thus, endothelial cells sense dynamic changes in the environment and feed this information into existing intracellular signaling to influence cell behavior.

The need to process information about the extracellular environment is even more relevant for migrating cells. Leukocyte transit from the vasculature to the subendothelial matrix, for example, relies upon mechanically activated adhesion receptors gathering information about the vascular endothelium upon which leukocytes travel. Endothelial presentation of selectins may be recognized by white blood cells flowing through the blood. Ligation of P-selectin glycoprotein ligand-1(PSGL-1) with glycoprotein ligands

on the surface of a rapidly moving leukocyte can result in strengthening of the P-selectin-PSGL-1 catch bond, leading to leukocyte deceleration.[111,112] While P-selectin and PSGL-1 bonds are transient on the scale of ~0.5 seconds, they enable stronger, longer lasting integrin-ECM bonds to form.[111,112] These cell-ECM adhesions then lead to leukocyte polarization, accumulation of the membrane lipids phosphatidylinositol-3,4,5-trisphosphates (PtdIns(3,4,5)P$_3$), activation of Rac1 and Akt, cytoskeletal remodeling, and transmigration of the endothelium.[111,113]

Novel tools to study signaling in 3D matrices:
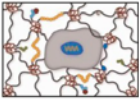
To study cell adhesion in 3D environments, many techniques have been developed to encapsulate cells in hydrogels, hydrated polymer networks that behave as viscoelastic solids (Table 2). Commonly used polymers in hydrogels include naturally derived materials including collagen, proteoglycan such as hyaluronic acid, fibrin gels, cellulose; and synthetic polymers such as polyethylene glycol (PEG), poly-vinyl-alcohol (PVA), poly lactic-glycolic-acid (PLGA), and engineering peptide based biomaterials. Peptide hydrogels are a useful system to study cell signaling in 3D as they allow tuning of individual environment parameters including matrix elasticity, cell adhesion binding sites, and degradation.[114] Examples of different peptides used include elastin and silk like polypeptides, or novel repetitive peptide sequences that form fibrils in ionic environments such as 'KFE' gels, which are ((acetyl)-FKFEFKFE-CONH2).[114,115] By modifying these gels with arginine-glycine-aspartic acid (RGD) sequences for integrin binding and changing the concentration of peptide, KFE gels can be fabricated to allow tuning of cell binding, matrix compliance and pore size.[115] When these gels are optimized, they enable formation of cell-ECM and cell-cell connections that promote endothelial tube formation, facilitating the study of 3D endothelial cell signaling in an *in vitro* system that far more accurately resembles a capillary bed compared to 2D culture.[115]

The 3D microenvironment can be specifically controlled *in vitro* by embedding cells in a hydrogel with specific molecular composition and concentration. Individual cells can be placed in self-assembling peptide gels, cross-linked collagen matrices or reconstituted basement membrane hydrogels such as Matrigel.[116]

Breast cancer cells such as MDA-MB-231, for example, alter their morphology and adhesion in response to altered ECM properties, while MCF10a cells create stable spheroids in compliant, but not stiff collagen matrices.[116,117] Furthermore, cell behavior can be influenced by controlling ECM properties like stiffness, which, in the case of collagen gels, can be modulated by increasing collagen concentration or via inhibition of lysyl oxidase mediated collagen crosslinking.[118,119]

The effect of altered cell-matrix and cell-cell interactions on intracellular signaling is undeniable. The cell is continuously gathering information about its surroundings and incorporating this information into its decision making circuits. As such, researchers need to be particularly aware of their phenomena of interest and how cellular context can introduce confounding factors into their studies. Culturing cells in 2D vs. 3D, or one ECM component vs. another, results in such cell-wide changes that choices of experimental conditions must be thoughtfully made.

Table 3.2. Summary of 3D Culture Systems.

Method	Type	Example(s)	Benefits	Constraints
Hydrogel Systems Further reading: [118,127,128]	Natural	Collagen, Matrigel, chondroitin sulfate, hyaluronic acid, chitosan, cellulose, alginate, fibrin, elastin[129]	Can be derived from polymers naturally found in-vivo in a tissue of interest, degradable	Polymer variability with heterogeneous ligand presentation and matrix properties.
	Biomimetic	Poly(ethylene glycol) (PEG), poly(vinyl alcohol) (PVA), poly(hydroxyethyl-methacrylate), (poly(HEMA)), self assembling peptide gels (SAP)[130]	Permits extensive chemical functionalization and better control of mechanics and architecture	Cell toxicity, biocompatibility issues
	Biosynthetic	Collagen peptide Arg-Gly-Asp (RGD) conjugated biomimetics, and matrix metallo-proteinase (MMP) sensitive biomimetics[130]	Can combine positive features of natural and biomimetic scaffolds	Often difficult and expensive to synthesize
Tissue-Specific Microfabricated Culture Systems Further reading: [131]	Geometric mimicry	Liver Subunit[117]	Allows dense hepatocyte culture	Requires micro-fabrication facilities and constant perfusion; elastomeric materials not always representative of ECM components and properties; difficult to scale size of culture
		Vascular Beds[122]	Controlled geometry and cell seeding; coculture	
	Functional mimicry	"Lung on a chip"[123]	Simulated "breathing" via pressure-mediated dilation of PDMS membrane	

3D SIGNALING AT THE MULTICELLULAR LEVEL

Cells in the body exist in a three-dimensional environment. They interact on all sides with other cells, the extracellular matrix, and interstitial fluid. These interactions provide input that the cell then integrates to determine behavior and fate. At the tissue level, two major factors influence cell behavior--local gradients in signaling molecules and multicellular structures. The following section highlights molecular gradients in development and duct-like multicellular structures.

Molecular Gradients in Multicellular Structures:

Sources and sinks for signaling molecules, combined with interstitial pressure, serve to establish molecular gradients that can differentially influence cells within a tissue based on their location. These gradients are established through a combination of cell secretion, protein diffusion, proteoglycan-mediated stabilization, and endocytic depletion in neighboring cells.[120–122] Some source, or collection of cells secreting the morphogen, acts as the focal point from which diffusion distributes the morphogen. Proteoglycans in the extracellular matrix, like glycosaminoglycans (GAGs), sequester and maintain local supplies of morphogen.[19] Finally, depletion of the morphogen from interstitial fluid occurs via receptor-binding, endocytosis, and degradation.[122,123]

Many examples of molecular gradients can be found in development. In the early *Drosoophila* embryo, before nuclei are separated by cell membranes, a Bicoid (Bcd) gradient governs the expression of gap genes.[124,125] These genes dictate the anteroposterior patterning of the embryo, and if mutated, can lead to a loss of continuous segments in the developed organism.[124,125] At later stages of development, Decapentaplegic (Dpp) and Wingless (Wg) gradients in the wing imaginal disc have been linked to proper segmentation and wing development.[122,126] In the imaginal disc, the Dpp gradient arises through a combination of changes to Dpp secretion, diffusion, stabilization and depletion. Dpp at the cell surface is captured at the surface of a cell via low-affinity interactions with heparin sulfate proteoglycans, decreasing the diffusion of Dpp. Improved availability of Dpp leads to increased interactions with its receptor, resulting in amplified intracellular signaling.[127,128]

Similarly, gradients of the vertebrate Dpp homolog, bone morphogenetic protein (Bmp), is vital for dorsal/ventral patterning.[129,130] High local BMP levels specify ventral tissues, while low BMP signaling leads to development of dorsal tissues.[129] Sonic hedgehog (Shh), transforming growth factor-β (TGFβ), and fibroblast growth factor, gradients have similar effects on developing cells.[131,132] In all these cases, progenitors have concentration-dependent responses to morphogens. In chicks, for example, the duration of neural cells' responses to Shh is directly proportional to its local concentration.[120] This Shh response controls the expression of important transcription factors, which in turn direct differentiation into specific neuronal subtypes.[132]

While simple model organisms like *D. melanogaster* and *C. elegans* make investigation of the effects of these morphogen gradients possible, translation and extension of this work into more complex specimens is a major challenge. The deterministic pattern of development in *C. elegans* and the small number of cells in the developed organism, for example, facilitate reliable lineage tracing, where transfection of specific cells with genetic markers allows identification of their progeny.[133] This can be combined with secondary markers that indicate the relative expression of genes responsible for driving different cell fates.[133] The resilience of *D. melanogaster* permits the use of simple knockout systems to identify the role of genes like Dpp and Wg. These and other methods have led to enormous strides in understanding the processes governing development. However, the same techniques cannot be applied to understand the establishment and effect of molecular gradient in more complex systems. Many knockouts are embryonic lethal in mammals, precluding analysis of their effects on development. Further, many of these model organisms are transparent and thus particularly amenable to imaging approaches. Most tissues are not transparent and preclude the use of common visualization techniques. The increased genomic complexity of higher order organisms makes systematic screening an often untenable challenge. These factors have hampered researchers' investigation and left an important facet of biological function largely unexplored. While hints of the role of molecular gradients have arisen in studies of human embryonic development, little is known about their importance in normal tissue function. Yet, given that many of the same mechanisms that apply

to morphogen gradients apply in normal tissues, it is probable that gradients play an equally important role in signaling in tissues.

Transport phenomena in tissues:

A key indication that molecular gradients exist in tissues, and must therefore be processed by cells, is the myriad convective transport phenomena known to be at play in tissues. These transport processes generate interstitial flow that would result in local gradients in signaling factors. A major driver of convective flow is interstitial pressure. Interstitial pressure results from hydrostatic pressure and osmotic pressure differences among the vasculature, interstitium, and lymphatics.[134] Positive pressure from blood vessels, combined with leaky capillaries, pump fluid and soluble factors into the tissue. Negative pressure gradients between the tissue and lymphatic system is maintained by pumping in the draining lymphatic capillaries.[134] Tissue stretching and compression due to regular movement can also cause transient interstitial flow. These patterns are altered in tumors, where leaky vasculature and increased interstitial pressure inhibit leakage from capillaries into the interstitium. This altered transport can contribute to oxygen deprivation within the tumor, creating hypoxic conditions that activate HIF-1 (hypoxia-inducible factor 1), a transcription factor implicated in control of metabolism, invasion, and apoptosis.[135] HIF-1 upregulation, in turn, has been strongly implicated in increased tumor aggression and therapeutic resistance.[136,137]

In addition to pressure differences, ciliary movement in the lung and intestines can also drive interstitial flow. These small convective flows have been demonstrated to govern normal branching morphogenesis in the embryonic lung by directing points at which splitting should occur.[138] Interstitial flow has been demonstrated to allow generation of pericellular gradients, where directional flow around a cell secreting some signaling factor leads to asymmetrical distribution of that factor around the cell, thereby facilitating generation of an autologous chemotactic.[139] On a larger scale, immune cells use molecular gradients established by interstitial flow to home to the lymphatic system. While these chemotactic behaviors are well documented, there is no doubt that non-motile cells are similarly affected by gradients established by interstitial flow. The presence of extracellular signaling factors and the factors influencing differential

exposure to these factors within a multicellular structure are, therefore, relevant aspects to include if we are to gain a full picture of the dynamic nature of signaling *in vivo*.

Cell Organization and Signaling in Multicellular Tissues:

Cellular localization is an important aspect of signaling at the multicellular level, affecting its exposure to other cells, the ECM, and soluble signaling molecules within the interstitial fluid. In contrast to monolayer culture, where all cells have essentially the same relationship with one another and the nutrient source, multicellular structures can dramatically alter the environment in which a cell receives signals. In human breast ducts, for example, luminal and myoepithelial cells encounter dramatically different environments. Whereas the inner luminal epithelial cells are exposed to the hollow duct and lined with myoepithelial cells, the myoepithelial cells are sandwiched between the luminal epithelial cells and the basal lamina. Thus, myoepithelial cells are subject to more ECM signals than the luminal epithelial cells. Yet this complexity is not captured in conventional culture of these cells, which could lead to artifactual observations that do not translate to *in vivo* behavior. Culture of transformed mammary epithelial cells in 3D matrix can suppress proliferation and reestablish cell polarity, while oral squamous cell carcinoma cells exhibited higher angiogenic potential under 3D conditions.[140,141]

Similarly, the importance of paracrine signaling from neighboring cell types has been highlighted by the necessity for feeder culture of stem cells. Since the early 1950s, maintenance of the undifferentiated state of embryonic stem cells *in vitro* has been achieved via co-culture with fibroblasts.[142,143] Recently, this has been substituted with culture of conditioned media containing fibroblast-secreted factors like BMPs and leukemia inhibitory factor (LIF) or 3D culture of stem cells.[144–146] Cells are rarely in isolation in the body; there is no doubt that many other such mechanisms of cell control have been lost in the transition to *in vitro* culture.

A functional example of the importance of multicellular structures may be found in the brain, where neuron-glia networks cooperate to transduce signals.[147–149] Neurotransmitters secreted by neurons can initiate signaling in glial cells, which then secrete neuromodulatory factors that act on neurons within the

31

synapse, including glutamate and thrombospondin.[147,149–151] Glial cell morphology allows them to contact multiple neuronal cell bodies and extend into thousands of synapses, making them uniquely positioned to act as an integrator and modulator of neuronal activity.[149] As such, the specific positional relationships among neurons and glial cells within a network can be key to how that network responds to and propagates stimuli.

In addition, multicellular structures often optimize cellular access to nutrients. In particular, hepatocytes are known for their sensitivity to *in vitro* culture. Compared to the dense populations found *in vivo*, hepatocytes lose viability or transdifferentiate at high densities in monolayer culture[152–154] This can be partially addressed by culturing them in a microfluidic device with a geometry that maximizes cell access to a central fluidics chamber that mimics the hepatic artery.[155] This enhanced proximity to nutrients via altered organization allowed high-density hepatocyte culture closer to *in vivo* conditions.[152]

Cells do not signal in isolation within the body. They are parts of multicellular structures exposed to gradients of signaling molecules and physical forces. Their positions within a highly organized structure dictate their exposure to a specific set of signaling inputs, which may differ from those of neighboring cells. This organization and coordination permits these cells to work as a unit to perform a biological function. Accordingly, a full understanding of cell signaling requires studying the cell as part of a larger unit.

Novel techniques to study multicellular structures in 3D

Many of the conditions that may govern signaling in 3D have eluded researchers due to inadequacies in culture methods. Recent recognition of the importance of the context in which signaling occurs, including molecular gradients, cell-ECM interactions, and multicellular organization, has led to the development of novel culture techniques that seek to recapitulate 3D conditions seen *in vivo* (Table 4.2).

The most basic of these is 3D encapsulation culture. This involves embedding cells in a hydrogel composed of ECM components to better mimic the immersive environment of the body. This technique has spawned the development of many biomimetic or biosynthetic materials, including Matrigel™, hyaluronic acid,

collagen, and alginate.[156] However, except in cases of self-organization, this method still fails to recapitulate the complex organization of cells and the ECM *in vivo*.

Soft lithography, on the other hand, is proving to be a boon for researchers seeking more precise control of their culture conditions. This family of methods adapts approaches used in manufacturing microelectronic chips to fabricate or replicate nanometer scale structures and patterns on elastomeric materials like polydimethylsiloxane (PDMS).[157] These methods offer unprecedented control over features in a culture system, including geometry, patterns of ECM protein functionalization, and application of flow.[157,158] Soft lithography has been used to generate features that mimic the layout of a blood vessel, or facilitate multi-cell type culture.[159,160] The open design aspect of soft lithography also allows researchers to model *in vivo* multicellular organization, leading to fabrication of devices that recapitulate the shape and layout of major organ subunits within the liver and lung.[155,161,162] In addition, microfluidic culture permits introduction of flows, in contrast to conventional static culture. This allows recapitulation of both vascular flow and interstitial flow, facilitating the establishment of molecular gradients.[163,164] 3D printing confers even greater control over culture conditions, allowing layer by layer construction of extracellular matrix and cells. Biodegradable carbohydrate scaffolds can be used to create architecturally complex "organs". Miller *et al.* used this method to create 3D cylindrical networks of cells within an ECM network .[160]

While these novel microfabrication approaches are both powerful and versatile, in many ways, they are still in their infancy. The elastomeric materials used in soft lithography have a limited range of mechanical properties that may not reflect *in vivo* conditions. Further, while proof of concept cell studies usually accompany technical descriptions of these systems, extensive analysis of intracellular signaling in these culture settings has not been performed. Finally, application of these systems requires a minimum level of commitment and investment that may not be feasible for everyone. Nonetheless, the field is a rapidly growing one with exciting potential.

Studying multicellular structures *in vitro* has only recently become a reality. However, single cell level studies cannot impart information about emergent properties of the organized system. As such, in order to achieve a more thorough understanding of functions within the human body and to design drugs in an

informed manner, researchers should test their hypotheses in higher order systems. This step is unnecessary for many—there remain myriad unsolved mysteries within the cell that would not benefit from introduction of the multicellular context. For others with their eye on physiological relevance and translational applications, however, it is entirely apropos.

CONCLUSION

As researchers' understanding of cellular behavior in 3D progresses, studying signaling in the appropriate context has become essential. From intracellular localization of signaling molecules to molecular gradients at the tissue level, it is apparent that signaling is influenced by a myriad of factors and is a far more complex process than the simple interaction of reactants to form an end product. This recognition has spurred the invention of new technologies to facilitate investigation of signaling in 3D contexts. At the cellular level, novel superresolution imaging tools allow unprecedented characterization of protein localization and interaction dynamics. Bioengineered materials serve as in vitro mimics of complex tissue ECM, helping to elucidate the role of cell-matrix interactions in governing intra- and intercellular signaling. Finally, microfabrication and 3D printing permits recapitulation of multicellular structures, bringing multiple cell types together in physiologically relevant ways and revealing emergent properties at the tissue level. Results from the application of these tools has demonstrated that cell behavior can change dramatically based on the conditions under which they are studied. As such, it is no wonder the biomedical field has been faced with unprecedented failure rates in translating hard-earned discoveries into clinical progress. Therefore, it has never been more urgent for both basic science and translational research to be conducted in the appropriate context. With the adoption of new methods, findings from the laboratory will become more transferable to improve human health.

4 Matrix Dimensionality Mediates Enhanced Survival Signaling in 3D via Cytoskeletal Tension and GTPase Signaling

The following work was performed in collaboration with:

Fuiboon Kai[1*], Christian Frantz[1], Julie Friedland[1], Richard Tourdot[2], Alexandra Long[3], Brendan Baker[4], Johnathon N. Lakins[1], Wei Guo[5], Christopher Chen[4], Sophie Dumont[3,6], Ravi Radhakrishnan[2], Valerie M. Weaver[1,7]

---

[1] *Center for Bioengineering and Tissue Regeneration, Department of Surgery, UCSF, San Francisco, CA, USA.*
[2] *Department of Chemical and Biomolecular Engineering, University of Pennsylvania, Philadelphia, PA, USA.*
[3] *Department of Biophysics, UCSF, San Francisco, CA, USA.*
[4] *Department of Bioengineering, Boston University, Boston, MA, USA*
[5] *Department of Biology, University of Pennsylvania, Philadelphia, PA, USA.*
[6] *Department of Cell and Tissue Biology and Department of Cellular and Molecular Pharmacology, UCSF, San Francisco, CA, USA.*
[7] *Department of Anatomy, and Department of Bioengineering and Therapeutic Sciences, Eli and Edythe Broad Center of Regeneration Medicine and Stem Cell Research, Helen Diller Comprehensive Cancer Center, UCSF, San Francisco, CA, USA*

Introduction

As indicated in the previous chapter, matrix dimensionality is a property of the extracellular matrix (ECM) that directs cell signaling and fate, including cell polarity[141,165,166], capacity to differentiate[167,168], and migration mode[169,170]. However, the mechanisms by which dimensionality regulates these processes are largely unknown. There are clear signs that the cell undergoes gross biophysical changes in response to altered matrix dimensionality, including reorganization of the actin cytoskeleton[61,171,172]. Cytoskeletal rearrangement is implicated in regulating signaling scaffold formation, protein trafficking, and membrane dynamics, all of which can influence the subcellular localization of proteins. Hence, we asked whether matrix dimensionality regulates cell behavior and fate via spatial regulation of signaling molecules. Here we show that apoptotic signaling can be strongly countered by three-dimensional exposure to ECM via modulation of actin cortical tension. We demonstrate the importance of cortical tension-driven membrane curvature differences in enhancing cell survival in three-dimensional, laminin-rich ECM via altered GTPase signaling. Using a combination of biophysical characterization, computational modeling, and cell biology, we implicate decreased cortical tension in 3D in exclusion of positive membrane curvature-sensitive GTPase-activating proteins (GAPs) from the plasma membrane, promoting GTPase activation and cell survival. Our results point to the importance of studying cell behavior in physiologically relevant contexts and provide a mechanism by which biophysical changes lead to altered intracellular signaling. This has implications for such fields as tissue engineering and cancer biology, where promising *in vitro* results have failed to translate in practice and would benefit from mechanistic understanding of how extrinsic cues influence existing knowledge of device function or therapeutic efficacy.

BIOPHYSICAL CHARACTERIZATION OF CELLS IN 2D AND 3D CONTEXTS

There are major phenotypic and functional differences between cells grown within a three dimensional ECM and those grown on two dimensional substrates. Many effects of culture in 3D may be reverted to resemble 2D phenotypes with perturbation of cell adhesion molecules, such as overexpression of focal adhesion kinase (FAK).[173] Altered integrin activity due to changes in matrix dimensionality can be linked
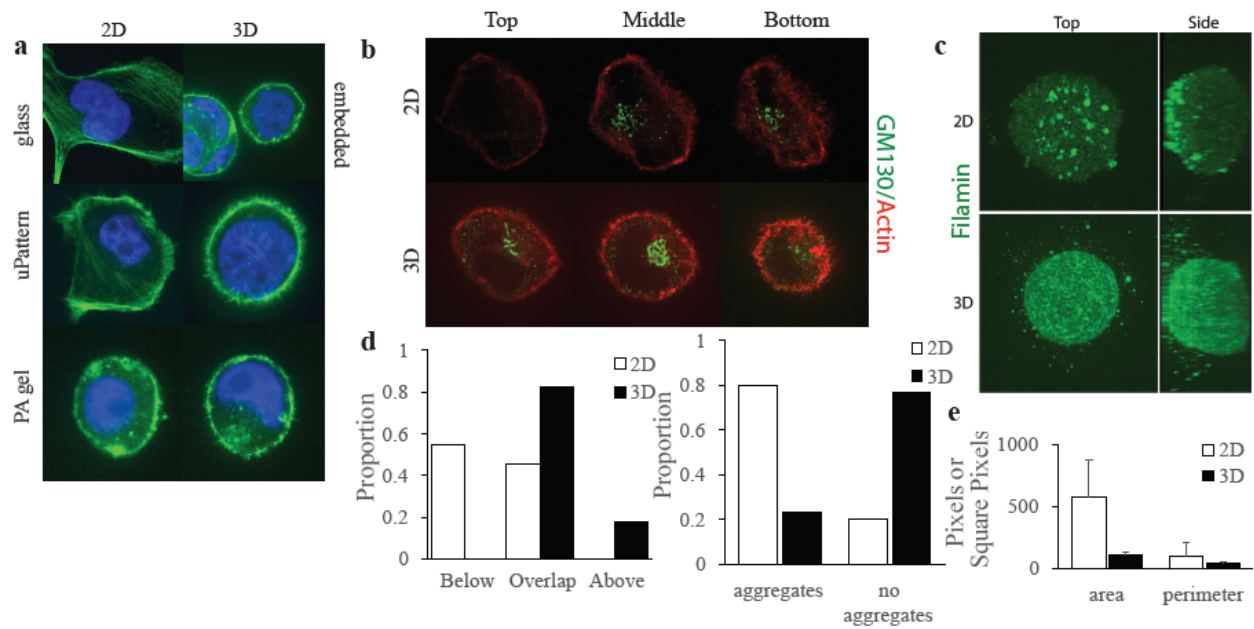
Figure 4.1. Polarity in 3D.

a) Comparison of cell morphology and actin organization in cells in 2D and 3D conditions on glass, micropatterned surfaces, and polyacrylamide gels. Green: phalloidin, blue: DAPI. b) Immunofluorescence images of Golgi polarization in cells in 2D and 3D. c) Immunofluorescence images of filamin polarization in cells in 2D and 3D. d) Quantification of proportion of cells with Golgi below, overlapping, or above the nucleus (left) and proportion of cells with large filamin aggregates (right). e) Quantification of filamin aggregate area and perimeter.

to altered gene expression,[165] cell growth,[44,165] cell morphology,[41] and motility[41] in cells. Modes and mechanisms of motility in cells in 3D matrices, in contrast to those on 2D substrates, are indicative of dramatic cytoskeletal and cellular reorganization[41,170,174]. Petrie *et al.* implicated lack of polarized signaling in the employment of a distinct mode of migration unique to cells in 3D contexts[170].These observations suggest that cell adhesion signaling and the cytoskeleton are significantly affected by altered dimensionality and that these changes propagate to influence other aspects of cell behavior.

To investigate how these structural changes might influence cell signaling and behavior, we first sought to validate loss of polarity in 3D culture using organelle positioning[175]. Using immunofluorescence imaging, we found that mammary epithelial cells (MECs) on 2D, 75Pa polyacrylamide (PA) hydrogels exhibited consistent polarized distribution of the Golgi apparatus relative to the nucleus. Specifically, the Golgi was found below the nucleus in 54% of cells (Figure 4.1b). In contrast, cells cultured in 3D reconstituted basement membrane (rBM) on top of a 75Pa PA gel was characterized by more random Golgi positioning (Figure 4.1b). We extended our investigation into cytoskeletal components and found that filamin, an actin crosslinker, is found in large aggregates at the top of cell in cells on 2D substrates and diffusely distributed in cells on 3D (Figure 4.1c). Quantification indicates that aggregates were found in nearly 80% of cells in 2D and were at least five times larger than those found in 3D (Figure 4.1d and e). Given filamin's known role in force generation and active mechanical stiffening by cells[176–178], we tested whether cell traction force generation is dependent on matrix dimensionality. Traction force microscopy indicated that cells on 2D substrates exert an average of 76Pa traction stress compared to an average of 57Pa for cells in 3D (p<<0.01, Figure 4.2a and b). Using atomic force microscopy (AFM), we tested whether cellular stiffness was affected by polarized filamin distribution and confirmed that cells in 2D are nearly twice as stiff as cells in 3D (Figure 4.2c). Further, we established that this difference in cell stiffness is dependent on the actin cytoskeleton, as inhibition of acto-myosin mediated contractility via treatment with blebbistatin (70μM for 10 minutes) decreased cell stiffness and equalized stiffness measurements across samples (Figure 4.2c). Consistently, blebbistatin treatment lowered traction force generation to less than 35Pa and removed differences between 2D and 3D (Figure 4.2b).
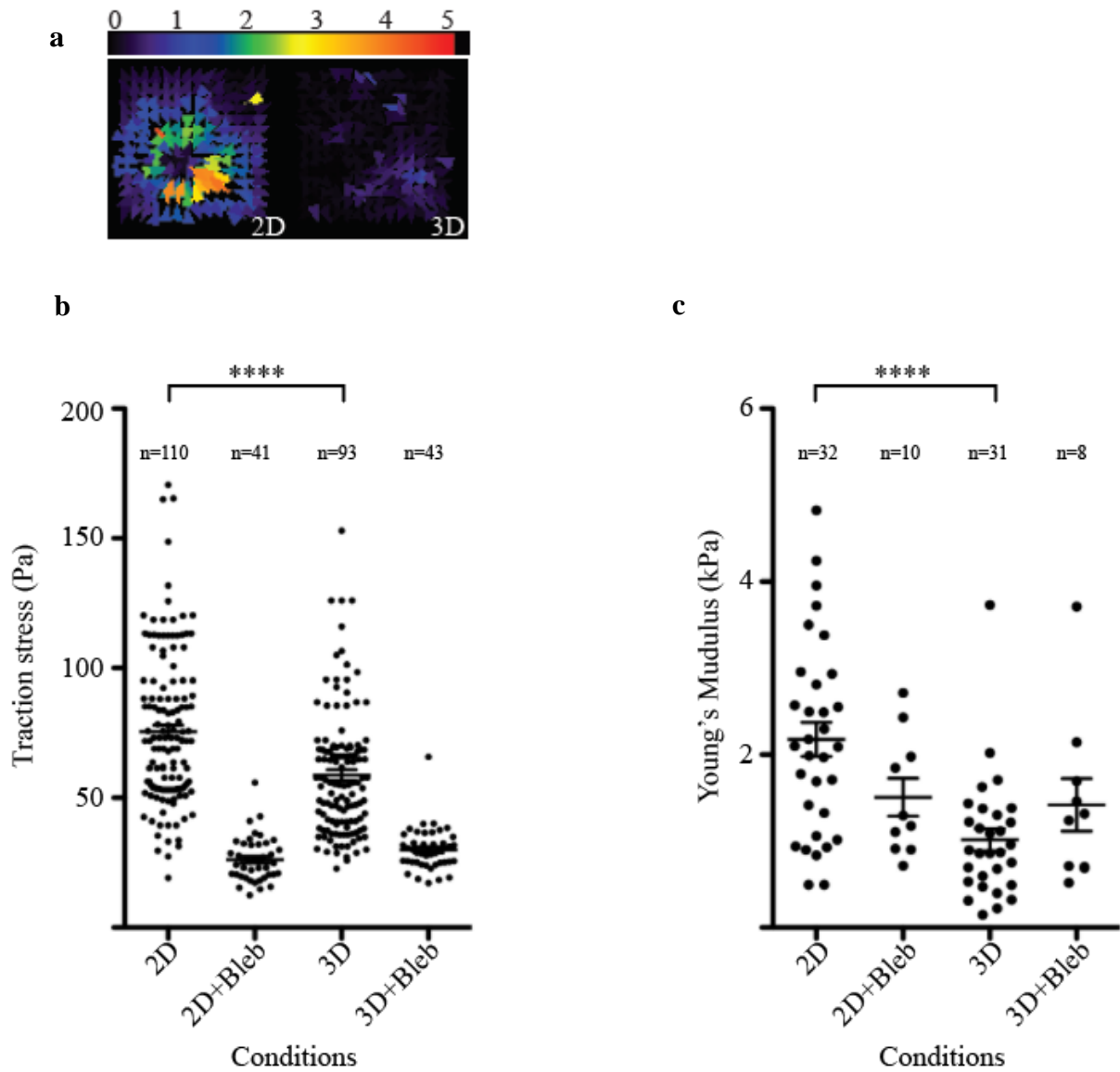
Figure 4.2. Traction force and atomic force microscopy analysis of cells in 2D and 3D.

a) Example traction force maps of cells in 2D and 3D. b) Quantification of whole cell traction in 2D and 3D, with and without blebbistatin treatment. c) Quantification of Young's modulus of cells in 2D and 3D, with and without blebbistatin treatment. **** indicates p<0.01.

To probe the impact of matrix dimensionality on cortical tension in particular, we employed targeted laser ablation of the actin cortex in MECs expressing Lifeact-RFP or –GFP and observed resulting bleb formation. Previously published work by Tinevez *et al.* suggested that this assay acts as a proxy for measuring membrane tension.[179] Specifically, Tinevez *et al.* validated that there exists a cortical tension (measured by micropipette aspiration) threshold above which cells, when ablated, will form blebs. Below this threshold, membrane tension is enough to counter the pressure released when actin cortex integrity is perturbed, preventing bleb formation. In our studies, cells on 2D substrates consistently formed blebs immediately following ablation, while greater than 90% of cells in 3D failed to bleb (Figure 4.3). This is consistent with previous studies that postulate a positive correlation between cortical tension and bleb formation rate. To test this theory in our system, we treated cells with blebbistatin and observed a decrease in bleb formation rate in 2D (Figure 4.3). Together, these biophysical measurements indicate that matrix dimensionality has a direct effect on acto-myosin mediated cell stiffness, traction force generation, and cortical tension.
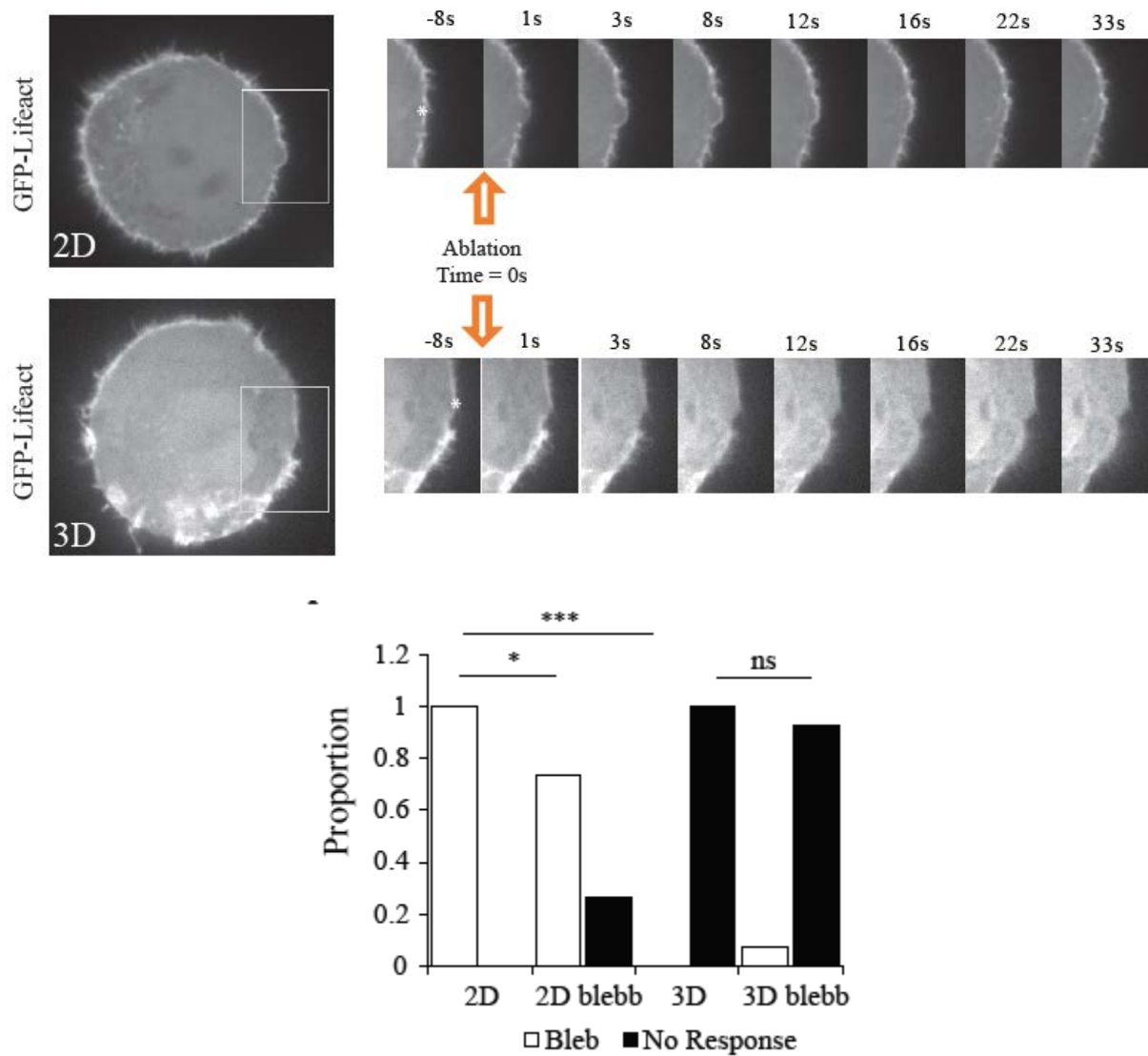
Figure 4.3. Traction force and laser ablation.

Top: Example snapshots of GFP-lifeact expressing MCF10As before and after laser ablation, in 2D and 3D. Bottom: quantification of proportion of cells that formed visible blebs after ablation in 2D and 3D, with and without blebbistatin treatment.

MATHEMATICAL MODELING OF MEMBRANE BEHAVIOR

Based on prior investigations linking cortical tension with overall membrane tension, we postulated that matrix dimensionality may influence membrane tension. While micropipette aspiration is typically used to measure membrane tension, technical challenges precluded its use in our experimental system. The presence of a 3D rBM overlay interfered with application of micropipettes. In lieu of direct measurements, we employed mesoscale modeling of membrane behavior under different tensions. By comparing predictions from computational modeling with experimental observations, we could then gain clues as to the effect of matrix dimensionality on membrane tension.

We explored the morphological conformational space of planar to highly curved membranes using the dynamically triangulated Monte Carlo technique[180]. Detailed implementation of this method has been previously validated[181,182] and is described in the supplementary information (S1-S3, Figure 4.9). Based only on our assertion that membrane tension is different between 2D and 3D contexts and parameters in literature, our model predicted that actin-mediated protrusions would exhibit dramatically different characteristics in 2D vs. 3D. Specifically, we computed the Helmholtz free energy of protrusion assembly as a function of membrane excess area (Figure 4.4b). Our results imply that for cells under small excess area (A/A_p), corresponding to high membrane tension, would form less stable protrusion assemblies when compared to cells under low membrane tension. The membrane deformation free energy, intriguingly, suggests that the density of shallow protrusions formed in cells with high membrane tension should be higher (owing to lower deformation free energy). In contrast, cells with low membrane tension are expected to be relatively longer but less dense (Figure 4.4c). Together, these suggest that actin-mediated protrusions are small, dense, and transient in 2D and long, sparsely distributed, and stable in 3D.

Based on these differences in membrane dynamics, we further asked whether a difference in membrane tension would lead to differences in protein recruitment to the membrane. We computed the excess chemical potential (or the free energy to add/recruit a protein) to three spatial regions of the membrane (Figure 4.4d) as a function of the membrane area (A/A_p). A lower value for excess chemical potential

signifies a more favorable recruitment of the protein to a given membrane location and higher local protein density. Figure 4.4e depicts the computed excess chemical potential of negative curvature inducing protein domains, showing such domains prefer to be localized to the site of protrusions and that such a segregation is much more favorable under regimes of low membrane tension (or 3D-like environment). Figure 4.4f depicts the computed excess chemical potential of positive curvature inducing protein domains and shows the opposite trend, namely, that such domains are depleted from protrusion regions and the propensity of segregation between basal and protrusive regions increase with decreasing tension. Our calculations also suggest that even basal recruitment of the curvature-sensing domains is higher under conditions of lower tension, suggesting that cells can employ dimensionality-sensitive mechanisms mediated by curvature-sensing proteins.
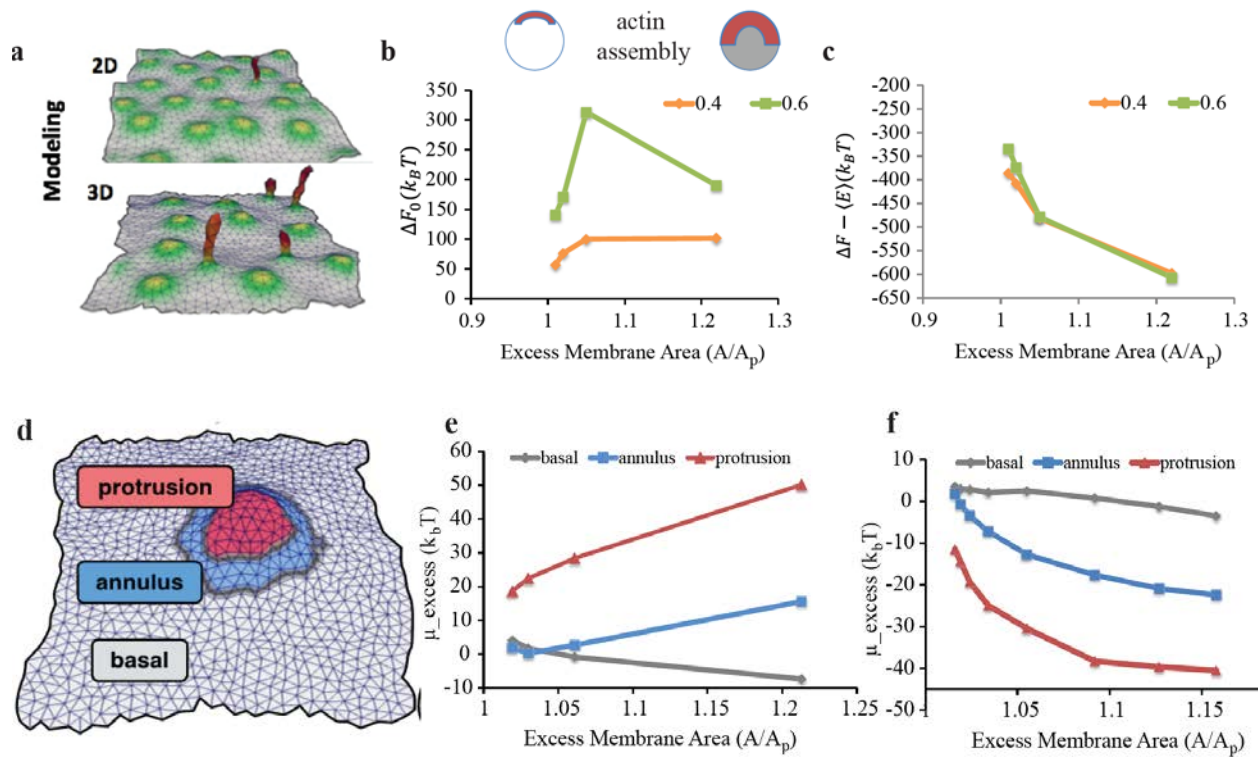
Figure 4.4. Mathematical modeling of protrusion dynamics and membrane curvature.

a) Visualization of model setup and results, where green and yellow regions indicate points of protrusion nucleation and red regions are protrusions. b) Model predictions of Helmholtz free energy associated with actin assembly as a function of excess membrane area, for two a_0 values, which maps to the peak spontaneous protrusion curvature. c) Free energy of membrane deformation as a function of excess membrane area values. d) Depiction of different areas of the membrane. e) and f) Excess chemical potential associated with recruitment of negative (e) and positive (f) to the three indicated spatial regions of the membrane.

EXPERIMENTAL VALIDATION OF MATHEMATICAL MODELING PREDICTIONS

To validate these computational predictions, we performed time-lapse confocal imaging of MECs expressing Lifeact-RFP or –GFP and quantified actin-mediated protrusion size, density, and residence time (Figure 4.5a). While protrusion length and width followed trends predicted by our computational models, high variability in cells in 3D led to inconclusive results (Figure 4.5c and d). Protrusion density, however, was nearly three times higher ($p<0.05$) in cells on 2D substrates; similarly, protrusion lifetime was approximately 110 seconds in 2D and 300s in 3D (Figure 4.5b and e). Both observations matched predictions from computational modeling.

To verify that these observations were due to differences in biophysical properties of the cell, similar measurements were made in cells treated with blebbistatin. As expected, mitigating myosin activity decreased protrusion density (Figure 4.5f), increased protrusion length (Figure 4.5g), and increased protrusion residence time (Figure 4.5h).

To validate predictions about curvature-sensing proteins, we used immunofluorescence and expression of GFP-tagged proteins to detect subcellular localization of Exo70, a previously demonstrated negative curvature-binding and stabilizing protein[182]. Again, as predicted by computational modeling, there was enhanced membrane-associated Exo70 in cells in 3D (Figure 4.6). Importantly, both the ratio of membrane to cytoplasmic Exo70 and proportion found within large aggregates was increased in cells in 3D (Figure 4.6). Further, this difference was verified to be dependent on acto-myosin contractility, as blebbistatin treatment in 2D induced membrane enrichment of Exo70 (Figure 4.6).
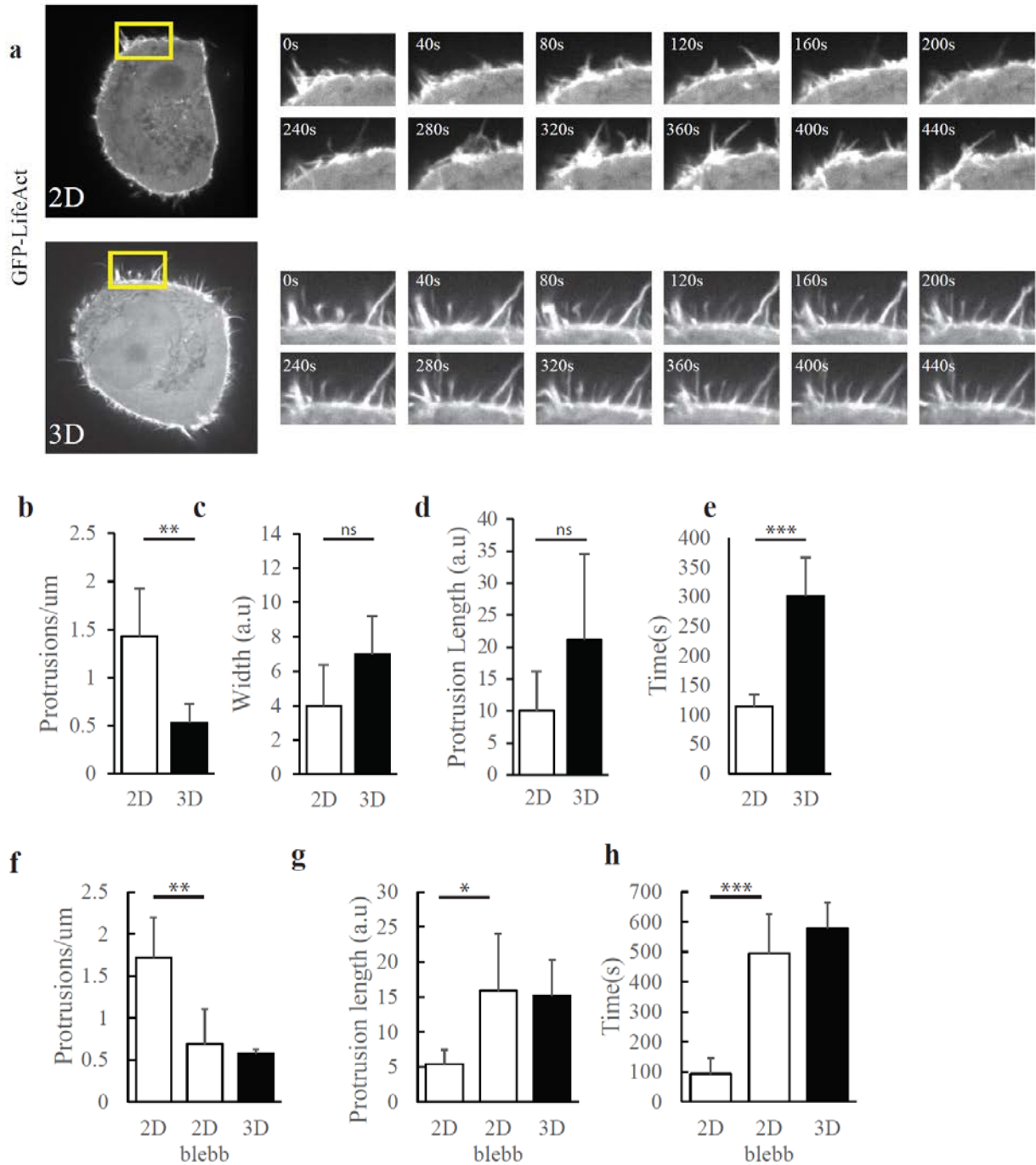
Figure 4.5. Experimental validation of actin protrusion dynamics.

a) Snapshots from timelapse imaging of GFP-Lifeact expressing MCF10As in 2D and 3D. Quantification of b) Protrusion density, c) Protrusion width, d) Protrusion length, and e) Protrusion residence time in 2D and 3D. Quantification of f) Protrusion density, g) Protrusion length, and h) Protrusion residence time in 2D, 2D treated with blebbistatin, and 3D.
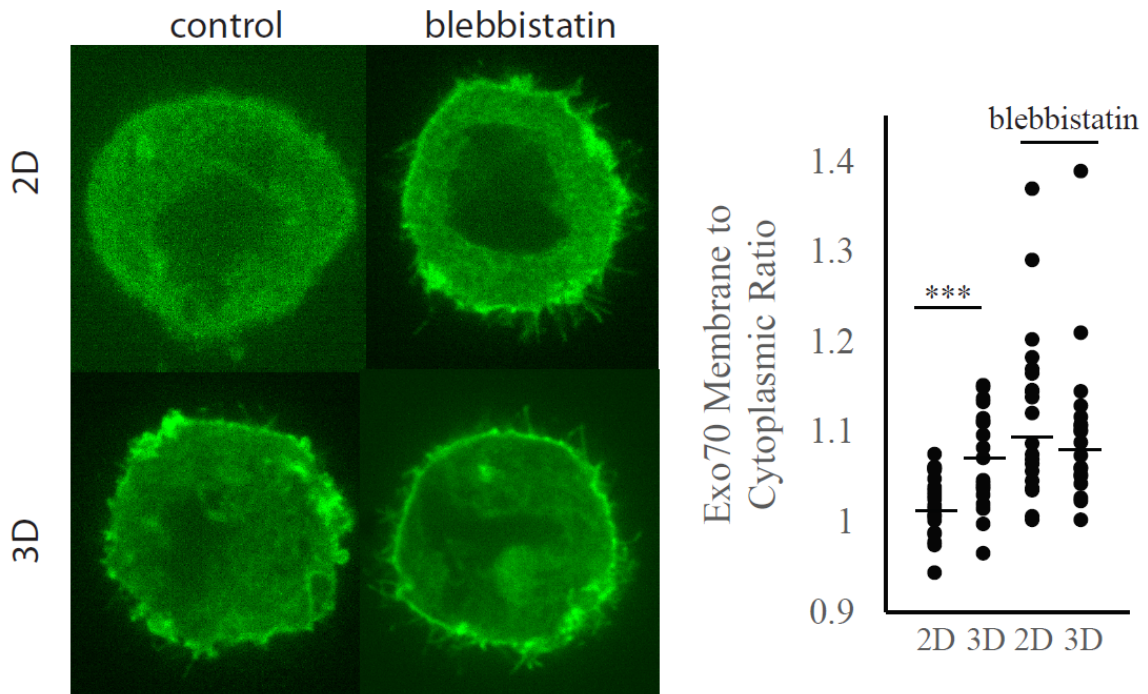
Figure 4.6. Exo70 localization in 2D and 3D.

Left: Example images of Exo70 (green) localization in 2D and 3D, with and without blebbistatin treatment. Right: Quantification of membrane to cytoplasmic ratio of Exo70 fluorescence intensity in 2D and 3D, with and without blebbistatin treatment.

In considering how these differences might translate to differences in signaling and cell fate, we took into account both existing knowledge about changes in cell behavior due to altered extracellular cues and how those changes may be connected membrane recruitment of curvature-binding proteins. One molecule of particular interest that arose is Arf6-GTPase. Arf6 is typically associated with regulation of cell migration and invasion via regulation of protein trafficking[99,183]. It has also been implicated in Erk and Rac1 activation and mediation of cell survival signaling. Cell migration[169,170], proliferation signaling[184], and Rac activity[185] have all been shown to be influenced by matrix dimensionality. Most intriguingly, several Arf6 effectors have membrane recruitment domains and a subset of them have curvature-sensing properties[186]. Specifically, several Arf6 GTPase activating proteins (GAPs) have positive membrane curvature binding domains, including BAR, ENTH, CALM, and CIN85[27], and Arf6 itself has been implicated as having curvature-sensing capacity[187]. Given results from computational modeling, we'd expect that exclusion of Arf6GAPs in 3D would lead to increased Arf6GTP levels. Indeed, we find via pulldown assays that culture in 3D is associated with increased Rac- and Arf6-GTP levels (Figure 4.7a).

Given the role of Rac- and Arf6-GTPase upstream of survival signaling, we first tested whether there are indeed survival differences due to matrix dimensionality. Culture of single cells in 2D and 3D contexts revealed that approximately 35% of cells in 2D undergo apoptosis, compared to less than 5% in 3D (Figure 4.7b). We show this difference in survival is dependent on acto-myosin contractility via ML-7 and blebbistatin treatment, both of which decreased cell death in 2D by more than 50% (Figure 4.7c). To test our mechanistic hypothesis, we used shRNA to knockdown Exo70, which has been previously shown to decrease negative curvature in cells[182]. If cortical tension-mediated changes in membrane curvature does indeed change Arf6 activation, and thereby downstream survival signaling, we would expect Exo70 knockdown to decrease cell survival in 3D. And indeed, we find that Exo70 knockdown increases apoptosis in 3D nearly seven fold, to levels similar to that found in 2D (Figure 4.8a).
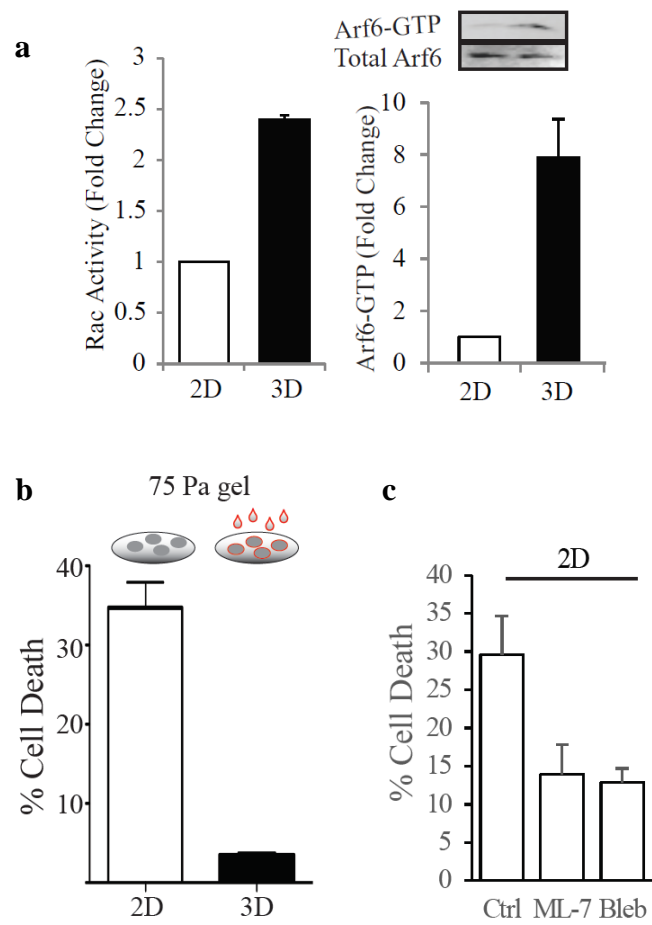
Figure 4.7. GTPase activity and cell survival in 2D and 3D.

a) Rac and Arf6GTP pulldowns in 2D and 3D. b) Cell survival in 2D and 3D. c) Cell survival in cells in 2D, with and without ML-7 or blebbistatin treatment.
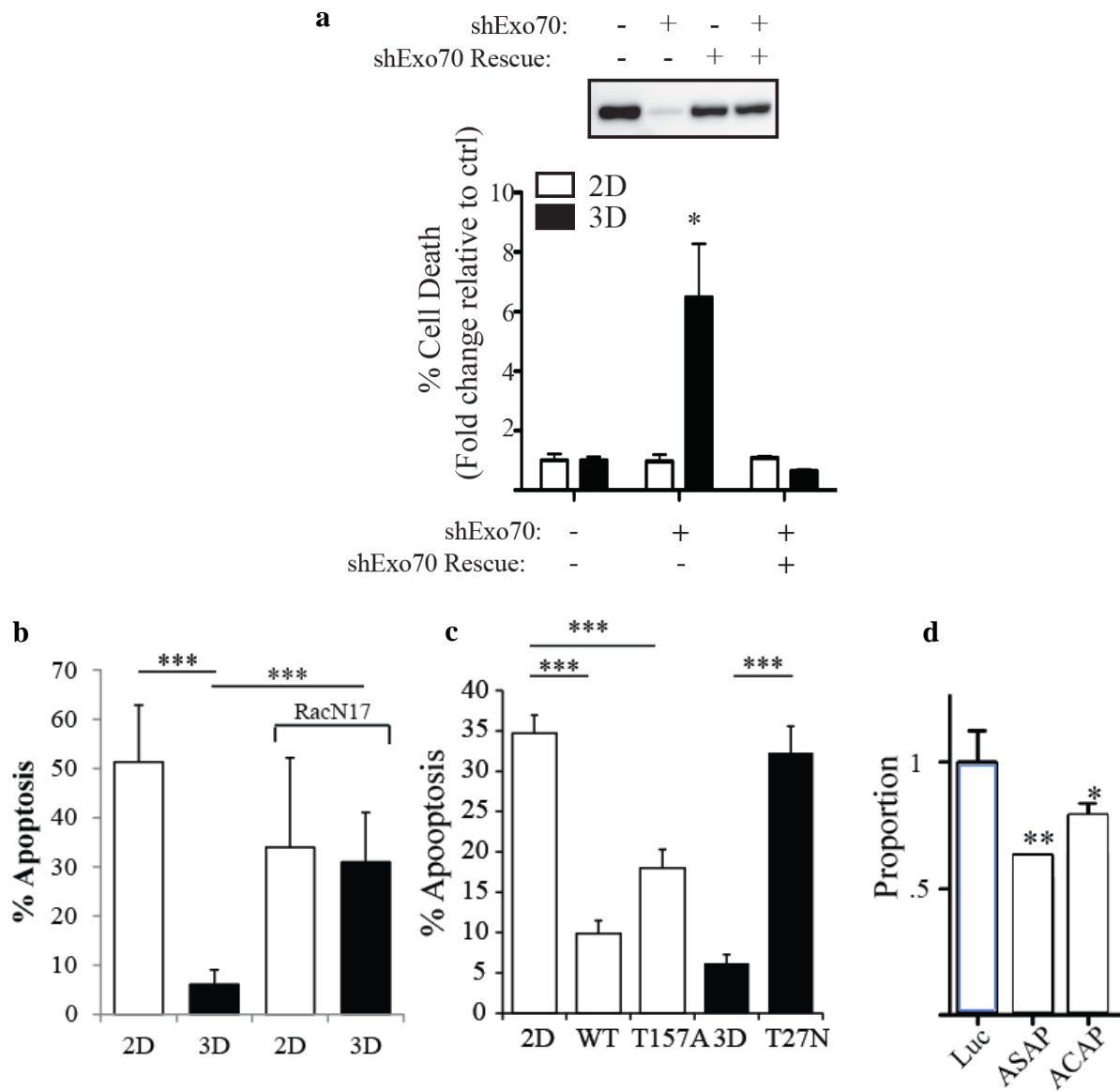
Figure 4.8. Manipulation of Rac and Arf6 activity and cell survival in 2D and 3D.

a) Cell survival in cells with and without Exo70 shRNA, with immunoblot validation of successful knockdown. b) Cell survival in control and RacN17 expressing MCF10As. c) Cell survival in control, Arf6WT, Arf6T157A, and Arf6T27N cells. d) Cell survival in control, ASAP shRNA, and ACAP shRNA cells.

To directly implicate Rac- and Arf6-GTPase activity in differences in cell survival, we used Rac and Arf6 functional mutants. Expression of a dominant negative RacN17 in cells led to an increase in cell death in 3D (Figure 4.8b). Consistently, expression of fast cycling Arf6T157A and overexpression of Arf6 in 2D both decreased cell survival (Figure 4.8c). Conversely, expression of a dominant negative Arf6T27N in 3D increased cell death (Figure 4.8c). Finally, we showed that knockdown of positive curvature binding Arf6GAPs, ASAP1 and ACAP2, and thereby increasing Arf6 activity, decreased cell death in 2D (Figure 4.8d).

DISCUSSION

Our data suggests a functional link between biophysical changes induced by matrix dimensionality and changes in cell fate. Specifically, culture in 3D depolarizes the cell and decreases both its traction force generation and cytoskeletal tension. This decrease in cytoskeletal and, by proxy, membrane tension, leads to a change in the energetics of protrusion formation and stability. These phenomena, in turn, govern the probability of GTPase activating protein recruitment to the membrane and thus GTPase activity within the cell. We've shown one particular GTPase pathway that appears to be affected by changes in matrix dimensionality and is linked to changes in cell survival. Attempts to directly connect GTPase activity with changing biophysical properties remain in progress. Overall, these results indicate a mechanism by which the context in which signaling occurs is altered via external biophysical cues. Undoubtedly, the global changes induced by matrix dimensionality shifts have more wide-ranging consequences, and further studies will need to be performed to catalogue and understand them all.

MATERIALS AND METHODS

Cell culture, antibodies, and reagents

MCF10A and HMT-3522 S1 human mammary epithelial cells (MECs) were grown and maintained as previously described[188]. Matrigel™ (BD Biosciences) was used to conjugate reconstituted basement

membrane to the polyacrylamide gels and for the three dimensional (3D) culture experiments. Laminin-1 (Sigma and Trevigen) was used to conjugate micropatterned surfaces and for 3D overlay manipulations. The following primary antibodies were used in these studies: cleaved caspase-3 (Cell Signaling); HA.11, clone 16B12 (Covance); Arf6, clone 3A-1 (Santa Cruz Biotechnology), GM-130 (BD), Exo70 (Sigma), filamin (EMD Millipore). The secondary antibodies used were as follows: HRP-conjugated anti-rabbit and mouse (Amersham Laboratories), AlexaFluor 488 and 561-conjugated goat anti-rabbit and anti-mouse (Molecular Probes, Thermo Fisher Scientific).

Vector constructs and gene manipulations

C-terminal HA tagged Arf6 constructs (WT, mutants Q67L, T27N; gift from M. Chou, University of Pennsylvania, Philadelphia, PA[4]), and the Arf6 T157A construct (gift from L.C. Santy, Pennsylvania State University, Pittsburg, PA[5]) were cloned into the pLV TetO$_7$mCMV tetracycline-inducible lentiviral vector[6] and expressed biscistronically with EGFP. GFP-tagged Exo70 was cloned into the the pLV vector with hPGK promoter.

All shRNA constructs were cloned into IPTG-inducible lentiviral vector. Stable MEC populations expressing the various transgenes and shRNAs were selected using either blasticidin, puromycin, or G418 and gene expression. Gene knockdown was confirmed through RT-qPCR and/or immunoblotting. When necessary, induced pools of infected MECs were FACS sorted for EGFP to enrich for transgene expression or loss.

shRNA sequences

ASAP1:

5' CCGGGCCAAGAATGTAGGAAACAATCTCGAGATTGTTTCCTACATTCTTGGCTTTTTTG-3'

ACAP2:

5'CCGGCCAGTATTGCTACTGCTTATACTCGAGTATAAGCAGTAGCAATACTGGTTTTTTG-3'

Exo70:

5'CCGGCGACCAGCTCACTAAGAACATCTCGAGATGTTCTTAGTGAGCTGGTCGTTTTTTG-3'

Micropatterned surface and polyacrylamide gel preparation

Micropatterned surfaces were prepared using the microcontact printing method as described[7]. In brief, photolithographic generated master templates were used to cast and bake PDMS stamps. ECM islands of defined geometry were coated (2 hr; 25 μg/ml) with fibronectin, type I collagen or laminin-1, washed with PBS (3-5X), and dried with compressed nitrogen. The ECM coated surfaces were then used to stamp UV-oxidized (UVO-cleaner 342, Jelight Co.) PDMS substrates and the coated surfaces were blocked with Pluronic F127 (3 hr) and washed with PBS (3X) prior to cell plating. Polyacrylamide hydrogels of defined elastic modulus were generated using a modified as previously described.[189]

Immunofluorescence

Cells were fixed in situ (20 min; room temperature) using 2-4% paraformaldehyde in PBS. After permeabilization in 0.5% Triton-X 100, samples were incubated with primary Abs, followed by Alexa-Fluor-488, 555 or 595-conjugated secondary antibody. Nuclei were counterstained with DAPI (Sigma).

Apoptosis Assay

Apoptosis was assayed by immunofluorescent staining of activated caspase-3, via TUNEL assay (Roche), or using the Molecular Probes LIVE/DEAD™ Cell Viability/Toxicity assay (Thermo Fisher Scientific). Percent apoptosis was quantified as the number of dying cells divided by the total number of cells. The minimum number of cells scored was 200 per experimental condition. Cells were visualized using a fluorescence microscope (Olympus model IX-81).

Immunoblotting

Cells were lysed in RIPA buffer (50mM Tris-HCl, pH 7.4, 150mM NaCl, 1% NP-40, 0.5% deoxycholate, 0.2% SDS, 20mM NaF, 1mM Na_3VO_4, 1 mM Pefabloc SC, 1 μg/ml leupeptin, 5 μg/ml aprotinin). After protein quantification, equal amounts were separated on reducing SDS-PAGE gels, immunoblotted and detected with an ECL-Plus system (GE Healthcare). Immunoblots were quantified with the Multi Gauge software (FujiFilm).

Arf6GTPase assay

Arf6 GTPase activity was assessed as previously described[10]. Cells plated on rBM-functionalized polyacrylamide gels in 2D or 3D (750,000 cells) were lysed on ice (4°C) in Arf6 lysis buffer (50 mM Tris pH 7.5, 100 mM NaCl, 2 mM $MgCl_2$, 0.5% deoxycholic acid, 0.1% SDS, 1% Triton X-100, 10% glycerol, 1mM DTT, 1 mM Pefabloc SC, 1 µg/ml leupeptin, 5 µg/ml aprotinin, 1 mM sodium orthovanadate and 1 mM sodium fluoride), clarified by centrifugation (20,817 RCF; 4°C; 10 min) and GST-GGA3 immobilized on glutathione-sepharose beads (20-30 µg; Amersham Biosciences) were added to the clarified lysate. Following incubation (1.5 hr; 4°C) the beads were washed (3X) in Arf6 wash buffer (50 mM Tris pH 7.5, 100 mM NaCl, 2 mM $MgCl_2$, 1% NP-40, 10% glycerol, 1mM DTT, 1 mM pefabloc SC, 1 µg/ml leupeptin, 5 µg/ml aproptinin, 1 mM sodium orthovanadate and 1 mM sodium fluoride) and bound protein was eluted in Laemmli buffer and separated on a 12% SDS-PAGE gel. Active Arf6 was detected by immunoblotting and specific activity was calculated by normalizing densitometric values of GGA3-associated Arf6 to total Arf6 (quantified in cleared cell supernatant lysate), as described.[10]

Traction Force Microscopy

MECs were plated sparsely on BM-coated 400Pa polyacrylamide gels containing fluorescent beads. The gel was mounted on a microscope chamber to maintain 37°C and 5% CO2 level. Phase contrast images were taken to record MEC position and fluorescent images of beads embedded in the gel just below the cells were taken to determine gel deformation. Images of MECs were collected before and after 0.5% triton X-100 treatment using a Nikon Inverted Eclipse TE300 microscope and a Photometric Cool Snap HQ camera (Roper Scientific). Images were exported to ImageJ and aligned using the StackReg plugin (NIH). The bead displacement field and the force field were reconstructed using Iterative Particle Image Velocimetry (PIV) and FTTC plugins from Image J, respectively.[190]

Atomic Force Microscopy

All AFM measurements were performed using a MFP3D-BIO inverted optical AFM mounted (Asylum Research, Santa Barbara, CA) mounted on a Nikon TE200-U inverted microscope (Melville, NY) placed on a vibration-isolation table (Herzan TS-150). A V-shaped gold-coated silicon nitride cantilever with a four-sided pyramidal tip (Asylum Research, Santa Barbara, CA) was used for indentation. The spring constant of the cantilever was 0.09 N/m. For each session, cantilevers were calibrated using the thermal fluctuation method.[191] AFM force maps were performed on 40 x 40 µm fields and obtained as a 12 x 12 raster series of indentation. Elastic moduli measurement of each cell was derived from the force curves obtained utilizing the FMAP function of the Igor Pro v. 6.22A (WaveMetrics, Lake Oswego, OR) supplied by Asylum Research. Cells were assumed to be incompressible and a Poisson's ratio of 0.5 was used in the calculation of the Young's elastic modulus. 2D measurements were conducted on MECs plated on a laminin-conjugated polyacrylamide gel of defined elastic modulus or micropatterned surface with media overlay. 3D measurements were obtained using MECs incubated with media containing laminin-1 (150μg/ml) for 24 hours.

Imaging and Laser Ablation

Immmufluorescence and live Lifeact imaging was performed on an inverted microscope (Eclipse Ti-E; Nikon) with spinning disk confocal (CSU-X1; Yokogawa Electric Corporation), 405 nm, 488 nm, 561, 635 nm lasers; an Apo TIRF 100XNA 1.49 objective; electronic shutters; a charged-coupled device camera (Clara; Andor) and controlled by Metamorph.

Live imaging for laser ablation was performed on an inverted microscope (Eclipse Ti-E; Nikon) with a spinning disk confocal (CSU-X1; Yokogawa Electric Corporation), head dichroic Semrock Di01-T405/488/561GFP, 488-nm (120 mW) and 561-nm (150 mW) diode lasers, emission filters ET525/36M (Chroma Technology Corp.) for GFP or ET630/75M for RFP, and an iXon3 camera (Andor Technology). Targeted laser ablation (20 3-ns pulses at 20 Hz at two target spots) using 551- (for GFP) or 514-nm (for RFP) light was performed using a galvo-controlled MicroPoint Laser System (Photonic Instruments)

operated through Metamorph. Laser strength was calibrated before each experimental session based on minimum power necessary to ablate a k-fiber.

Statistical analysis

All tests for statistical significance were done using an unpaired student's t-test, assuming unequal variances and a two-tailed distribution with a 95% confidence interval. Data was analyzed using Excel (Microsoft) software.

S1. Mathematical Modeling Validation

The description of modeling methods used for the free energy of tubule formation and free energy landscape

for protein recruitment on the cell membranes, as well as the subsequent analysis are detailed in this section.

S1.1 Membrane Simulations: Cell membrane simulations consist of a dynamically triangulated sheet

evolved with Monte Carlo according to the Helfrich Hamiltonian. This membrane simulation method is

adapted from techniques described in Ramakrishnan et al. [1]. Briefly, in this method the membrane patch

is discretized into N vertices, each of characteristic size a_0, interlinked by L links that form T triangles.

The membrane is initialized as a planar sheet with periodic boundary conditions, where both the height and

curvature of the membrane are maintained over the bounds. Monte Carlo techniques are then used to both

evolve membrane morphology and diffuse membrane proteins. The three Monte Carlo moves in the model

include the vertex move, which simulates thermal undulations, the link flip, which simulates membrane

fluidity and allows it to more dynamically remodel, and the protein move, which allows protein movement

along the membrane. All three MC moves are accepted with Metropolis acceptance criteria according to

the Helfrich Hamiltonian. The Helfrich Hamiltonian is an energy functional which governs the equilibrium

properties of membrane according to,

$$\mathcal{H} = \frac{\kappa}{2} \sum_{v=1}^{N} \left(2H_v - H_{0,v}\right)^2 A_v + \sum_{v=1}^{N} \sigma A_v. \tag{1}$$

Here κ and σ are the bending stiffness and the surface tension of the membrane, H_v and $H_{0,v}$ are the mean

curvature and spontaneous curvatures corresponding to vertex v, and A_v is the area associated with vertex

v. The summation in (1) is computed over all vertices in the discretized membrane. Proteins are included

in the model through their spontaneous curvature field H_0. This spontaneous curvature field can be patterned

on the membrane to model different biophysical processes. In the case of the generation of cell protrusions,

a spontaneous curvature field is assumed to be a circular collection of vertices of a prescribed spontaneous

curvature with a nearest-neighbor (Ising-model-like) potential keeping these vertices together. This circular

region of spontaneous curvature is meant to approximate the effects of a large complex protein-assembly involved in pushing out a protrusion. As a first approximation, for single membrane proteins, spontaneous curvature fields are assumed to be the form of a Gaussian function with a pre-factor C_0 (peak spontaneous curvature), and a variance ϵ^2 (field spatial extent).

$$H_0^P(r) = C_0 \, e^{(-r^2/\epsilon^2)}. \tag{2}$$

One measure of membrane morphology is the excess area present in the membrane; this quantity is defined simply as the sum of the curvilinear area of the mesh divided by the sum of its projected area on the xy-plane. High excess areas correspond to low tension, while excess areas close to 1 describe tense membranes. For all simulations the bending stiffness was initialized at 20 $k_B T$ and the tension at 0 $k_B T/a_0^2$, where T is the temperature and a_0 sets the link-length between adjacent vertices. Both these moduli are renormalized during equilibration for different initial conditions of link length. Renormalized tension is calculated by fitting the undulation spectrum of membrane undulations [2]. A table of the renormalized values of tension is shown in Table 5.1. A typical value of a_0 for the systems we model is a_0=10 nm; this value ensures that our choices of c_0=0.4-0.8 a_0^{-1} and ϵ^2=6.3a_0^2, are primed to model curvature sensing proteins such with BAR and ENTH domains, as justified in previous works [2, 3]. With this choice of the value for the scale parameter a_0, the characteristic size of the protrusion we model is of diameter 10a_0 (as set by the Ising potential), which amounts to 100 nm; this value is consistent with the diameter of membrane protrusions observed in cell studies [W. Guo, private communication, 2015]. We note that the choice of a_0 also sets the range of membrane tensions we model to the range 0-100 μN/m, which is consistent with the range to membrane tension values reported in cellular experiments [4, 5].

Table 4.1 Membrane excess area and renormalized surface tension

Initial link length	A/A_P	Renormalized σ ($k_B T/ a_0^2$)	Renormalized σ (μN/m) $a_0 = 10$ nm
1.27	1.0754	0.165312855	6.794358356
1.3	1.0295	0.51881372	21.32324391
1.33	1.0156	0.85017139	34.94204415
1.35	1.0132	1.066002153	43.81268848
1.38	1.0117	1.390551811	57.15167943
1.4	1.0112	1.619003582	66.54104724

S1.2 Free Energy Methods: The membrane model is coupled to several computational free energy methods including Widom insertion, inhomogeneous Widom insertion, and thermodynamic integration [1-3].

We employ Widom insertion as a computational method used to probe the excess chemical potential of a curvature inducing protein on a membrane with a given tension/excess area. The Widom insertion involves randomly inserting a virtual/test membrane protein into the system and recording the change in energy. This difference in energy between a system with n and n+1 proteins can be related to the excess chemical potential as,

$$\mu_P^{ex} = -k_B T \ \ln\langle e^{-\beta\Delta\mathcal{H}}\rangle_n, \tag{3}$$

where μ_P^{ex} is the excess chemical potential for the n+1'th protein and $\Delta\mathcal{H}$ is the change in energy calculated from the Helfrich Hamiltonian upon insertion of that protein. The Boltzmann weighted ensemble average of this change in energy is then related to the chemical potential. Extensive sampling of each equilibrated system can then converge this ensemble average. In all Widom results shown, simulations were equilibrated for 5 million Monte Carlo steps and sampled with Widom method every 100 steps. Only the

last 2.5 million Monte Carlo steps are used when computing the ensemble average to ensure an equilibrated system for sampling.

Widom insertion can also be derived in a spatially dependent manner where subsections of the system can be isolated by an axis of inhomogeneity. In inhomogeneous Widom insertion, each subsection has its excess chemical potential defined as

$$\mu_P^{ex}(\mathbb{R}) = -k_B T \ln\langle e^{-\beta \Delta \mathcal{H}(\mathbb{R})}\rangle_n, \tag{4}$$

where $\mathbb{R}$ is a collection of vertexes within a specified region. In the case of protrusion simulations, where a circular region induces spontaneous curvature, three regions are defined: a protrusion region, defined as all vertices within the Ising-potential, an annulus region, defined as a radial extension of the protrusion region, and a basal region consisting of the rest of the vertices in the membrane, see Figure 4.9

Thermodynamic Integration (TI) is a computational free energy perturbation method that computes the change in free energy between two states of the system (states A and B). TI works by defining a scalar parameter λ, which traces a path between these two states (state A: $\lambda = 1$; state B: $\lambda = 0$). The derivative of the Helmholtz free energy $F = -k_B T \ln Q$ (Q is the partition function) with respect to the parameter λ is given by:

$$\frac{\partial F}{\partial \lambda} = \langle \frac{\partial \mathcal{H}_{el}}{\partial \lambda}\rangle, \tag{5}$$

and the free energy difference between the states characterized by $\lambda = 0$ and $\lambda = 1$ is calculated as,

$$F_{\lambda=1} - F_{\lambda=0} = \int_0^1 \langle \frac{\partial \mathcal{H}_{el}}{\partial \lambda}\rangle \, d\lambda. \tag{6}$$

The change in free energy is calculated in the TI method by running a set of simulations with a range of lambda values from 0 to 1, where the integrand in equation (6) is calculated and stored. The discretized data are then integrated with the trapezoid rule to obtain the free energy difference between $\lambda = 0$ and $\lambda = 1$. All results shown were obtained with a window resolution of 0.1 (or $\lambda = 0, 0.1, 0.2, \dots, 1$). In order to

determine the accuracy of this window resolution, a sensitivity analysis was performed, where window sizes of 0.05 and 0.02 showed no appreciable difference in free energy.

Error was estimated in all free energy methods by running each simulation in quadruplicate and calculating the standard deviation.

S1.3 Reference State of Free Energy of Membrane Protrusions: To generate membrane protrusions, a spontaneous curvature field is applied at the center of the membrane that consists of 50 vertices; this gives the protrusion region an average radius of 4.55 a_0. The spontaneous curvature of the protrusion was chosen to be either 0.4 a_0^{-1} or 0.6 a_0^{-1} these values of spontaneous curvature gave the largest variety of protrusion structures when altering the membrane tension. Simulations with the spontaneous curvature 0.6 a_0^{-1} and low tension showed the generation of budding vesicles, while all other simulations generated protrusion-like morphologies without a constricted vesicle neck.

The free energy of formation of a protrusion was analyzed with TI. As described above, this method computes the change in free energy to deform the membrane with an applied spontaneous curvature field. In order to analyze the free energy of generating a protrusion on the membrane, the reference state of the free energy is changed according to,

$$\Delta F_0 = \Delta F + \langle \frac{\kappa}{2} \sum_{v=1}^{N} (2H_v)^2 \rangle_{\lambda=1} - \langle \frac{\kappa}{2} \sum_{v=1}^{N} (2H_v - H_{0,v})^2 \rangle_{\lambda=1}, \tag{7}$$

where ΔF is the change in free energy required to deform the membrane once the protrusion is assembly is already bound, and ΔF_0 is the change in free energy to generate a protrusion from an unstressed membrane.

S2. Studies of Protein Recruitment on Protrusions

Membrane protein recruitment on protrusions was analyzed by using inhomogeneous Widom insertion techniques coupled with simulation conditions detailed in the previous section (S1.3). In this study membrane protrusion morphologies are generated by applying a spontaneous curvature field of 0.4 a_0^{-1} in a circular pattern with an average radius of 4.55 a_0, as in the previous section. This study is conducted with no membrane proteins present (i.e. n = 0, n+1 = 1). Inhomogeneous Widom insertion is then done in

three spatially distinct regions: protrusion, annulus, and basal regions, see Figure 4.9. A snapshot of the simulations with panels depicting the three membrane regions, and a height map of the protrusion is shown in Figure 4.9.
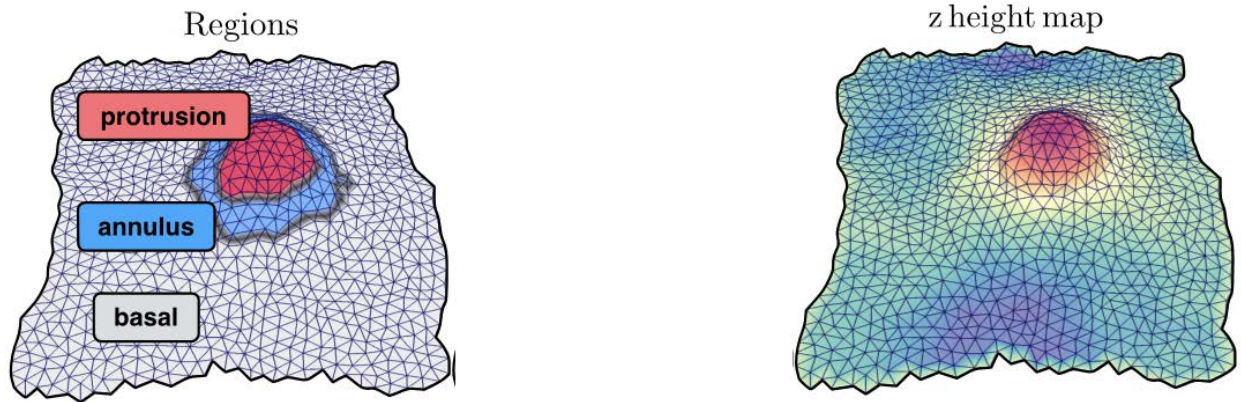
Figure 4.9. Membrane simulations.

Snapshot of membrane simulation detailing (left) the three inhomogeneous Widom regions, and (right) a height map of the z-axis of a membrane protrusion.

When conducting inhomogeneous Widom calculations, the background spontaneous curvature field of the protrusion-field was disregarded in the Widom formula. Membrane proteins with spontaneous curvature fields with the functional form in equation (2) were then randomly inserted and categorized into the appropriate region. The protrusion region was defined as all 50 vertices with the spontaneous curvature field. The annulus region was defined by creating a neighbor list at the point of insertion: if a protrusion region vertex existed within the first 30 closest neighbors of this vertex and the vertex was not a protrusion vertex itself, this was described as the annulus region vertex. Vertices that don't meet either of these criterions were categorized as the basal region. The proteins inserted in this study had peak spontaneous curvature of $C_0 = 0.4\ a_0^{-1}$ or $-0.4\ a_0^{-1}$ and a variance of $\epsilon^2 = 6.3\ a_0^2$.

S3. Protrusion Elongation Studies

Protrusion simulations are performed with several curvature-inducing membrane proteins present and with no other background spontaneous curvature field. In this study, membrane proteins diffuse around and are able to co-locate to produce tubule like structures. Once above a threshold density required for tubulation,

the protrusion elongates. The threshold density of proteins required for tubulation and consequently the protrusion length and density are strongly dependent on membrane interfacial tension.

S4. shRNA Validation

shRNA efficiency was validated via qPCR with the following sequences:

Exo70 F: 5'-AAG ATT CAG AAG GCA GTG GAG-3'

Exo70 R: 5'-AAT GAC ATC CTG GAG CAC G-3'

ASAP1 F: 5'-CAGCCAAGTTGAACCTTCTCACC-3'

ASAP1 R: 5'-CCTGCTCATCTTCTGCCTGAAAG-3'

ACAP2 F: 5'-CTGTGGTAGTTGAAGACCTCAGG-3'

ACAP2 R: 5'-CAGCTTTTCGGAATCTGCCTGG-3'
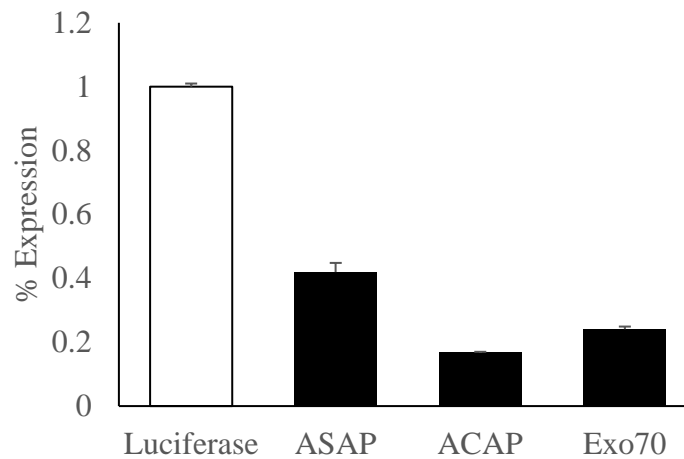
Figure 4.10 Q-PCR validation of protein knockdown, normalized against an anti-Luciferase control plasmid.

References:

1. Ramakrishnan, N., P.B. Sunil Kumar, and R. Radhakrishnan, *Mesoscale computational studies of membrane bilayer remodeling by curvature-inducing proteins.* Physics Reports, 2014. **543**(1): p. 1-60.
2. Tourdot, R.W., N. Ramakrishnan, and R. Radhakrishnan, *Defining the free-energy landscape of curvature-inducing proteins on membrane bilayers.* Phys Rev E Stat Nonlin Soft Matter Phys, 2014. **90**(2-1): p. 022717.
3. Tourdot, R.W., et al., *Multiscale computational models in physical systems biology of intracellular trafficking.* IET Syst Biol, 2014. **8**(5): p. 198-213.

4.   Diz-Muñoz, A., D.A. Fletcher, and O.D. Weiner, *Use the force: membrane tension as an organizer of cell shape and motility.* Trends in Cell Biology, 2013. **23**(2): p. 47-53.
5.   Vogel, V. and M. Sheetz, *Local force and geometry sensing regulate cell functions.* Nat Rev Mol Cell Biol, 2006. **7**(4): p. 265-75.

5 MATRIX STIFFNESS AND CELL BEHAVIOR IN CANCER

EXTRACELLULAR MATRIX STIFFNESS AND CANCER

Extracellular mechanical cues play a major role in regulating key cellular processes and signaling pathways. A large body of literature now supports the hypothesis that changing ECM stiffness, solid stress, or interstitial fluid pressure has a direct impact on cell morphology, subcellular protein localization, and gene expression[192–194]. Cells sense and process information about the mechanical properties of its microenvironment in a process called mechanotransduction, which in turn influences such disparate cellular functions as growth and proliferation, apoptosis, and migration[85,118,195]. One might note that these are all functions that become deregulated in cancer. Indeed, researchers have not only characterized the many ways in which the tumor ECM is dramatically altered when compared to its healthy counterpart but have also implicated these changes in promoting tumor-sustaining behaviors[118,195–198].

While early investigations into the link between mechanical cues and cancer progression were phenotypic and correlative, recent work has revealed the mechanistic underpinnings of this interplay. This has coincided with increased appreciation for and application of the concept of precision medicine, where knowledge of the mechanistic drivers of a particular cancer subtype is used to design directed therapeutics. While certainly a step forward from the carpet bombing strategy of chemotherapeutics, the guided missile of precision medicine has nonetheless fallen short. Targeting strategies that work in simpler models fail in human patients, and while no doubt a myriad of factors is behind this gap in efficacy, one of them is surely the increased complexity of the tumor microenvironment *in vivo*. For instance, if indeed mechanotransduction effects signaling events that crosstalk with the target of such therapies, like p53, then not factoring in the mechanical environment of a cell being treated with an anti-p53 drug will necessarily introduce variability in its measured effectiveness. In addition to potentially offering clinical insights, it is similarly important to consider cellular context when conducting cell biology research. Awareness of how mechanical cues regulate a particular pathway of interest is necessary in order to properly control for and take into account their impact on any measurements or observations that are made in an experiment. Deeper understanding of how the context in which cell signaling occurs affects that signaling then facilitates more

nuanced interpretation of any results. As such, we find it timely to reflect on our current state of understanding of how the mechanics influence cell signaling events to regulate cancer cell behavior.

In this chapter, we seek to synthesize existing literature to examine how the mechanical properties of the extracellular matrix, solid stress, and interstitial fluid pressure regulate the initiation and formation of a cancer, or tumorigenesis. In order to do so, it is important to define the bounds of what we will discuss. Hanahan and Weinberg, in two seminal publications[199,200], established a widely accepted set of "Hallmarks of Cancer" that we use as a basis for our discussion. Their hallmarks are all encompassing and meant to describe the disease of cancer as a whole, from initiation to metastasis. As we are focused solely on tumorigenesis, we divide their hallmarks into "tumor-initiating processes", "tumor-sustaining processes", and "tumor-disseminating processes", as illustrated in Figure 5.1. While there is debate over where tumorigenesis ends and tumor progression and dissemination picks up, it was necessary for the purposes of this discussion to draw a line. We take tumorigenesis to end at the establishment of a tumor mass and the beginning of invasion. This delineation means that the following sections will focus on mechanical regulation of the growth and proliferation, cell death, and genomic instability. While many reviews detailing the various cellular pathways impacted by changing extracellular mechanics exist, we seek to synthesize existing literature from a new perspective. That is, we focus here not on particular canonical pathways and not even on one specific cellular function. Instead, the information presented here is thematically linked by consideration of the mechanical environment in which tumorigenesis takes place, and how that environment might help or hinder the processes involved in the establishment of cancer.
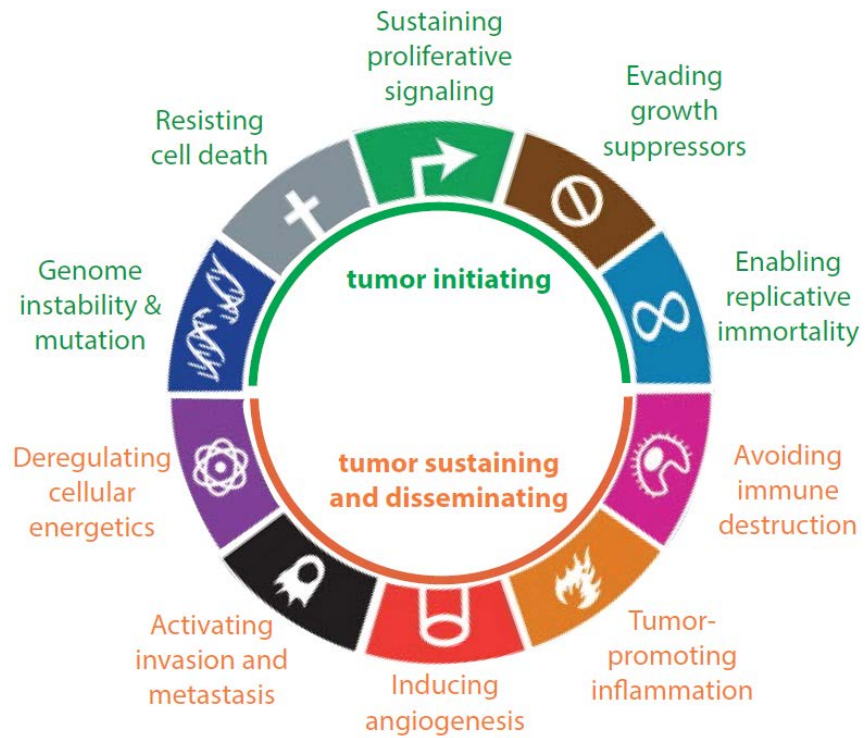
Figure 5.1. Mechanical regulation of the hallmarks of cancer.

The hallmarks of cancer, delineated by "tumor initiating" and tumor sustaining and disseminating" characteristics. Here, we will focus on how mechanical cues regulate tumor initiating hallmarks. Adapted from work by Hanahan and Weinberg[199,200].

MECHANOTRANSDUCTION: A BRIEF PRIMER

To make sense of the evidence that will be presented regarding how mechanical cues regulate various aspects of tumorigenesis, is it helpful to be acquainted with common cell signaling responses to such cues. Cells connect with extracellular matrix components through cell surface receptors, which are specific to macromolecules found within the matrix, like collagen or fibronectin[201]. These receptors nucleate complexes called focal adhesions, which are large plaques of proteins that connect receptors to the cytoskeleton and serve as a point of initiation for propagation of mechanical cues[202]. When cells are exposed to a stiffened ECM, integrin receptors form large clusters that correspond with large, mature focal adhesions populated with activated kinases, including focal adhesion kinase (FAK) and Src[195]. Formation of these strong connections to the extracellular matrix leads to an increase in acto-myosin mediated cell contractility, reorganization of the cytoskeleton into thickly bundled stress fibers, and activation of both Rho/Rho-associated protein kinase (ROCK)[203]. Mechanical cues can also increase GTP-loading of Rac, PI3K/Akt activation, and ERK activation[118,195,204].

MECHANICAL REGULATION OF CELL GROWTH AND PROLIFERATION

One of the defining characteristics of cancer is tumor cells' increased ability to grow and proliferate. A cell's growth, that is, increase in mass due to protein production and fluid influx, can be independent of cell cycle progression and replication[205]. However, replication is a far more important part of *tumor* growth and "growth and proliferation" are often referred to together in cancer literature and meant to indicate cell cycle progression. Hence, in this document, we consider growth and proliferation at the cellular level to go hand-in-hand and to be defined by cell cycle progression and cellular replication.

There is ample phenotypic evidence that mechanical cues regulate cell proliferation. Increasing ECM stiffness is associated with proliferation in normal and tumor cells, in a variety of contexts[206,207]. Exposure to solid stress can actually inhibit cell growth, while the effect of fluid shear stress on cells depends on cell type and context[208–211]. Our interest here is linking known mechanisms by which mechanical cues influence

proliferation to the ways tumor cells are known to upregulate growth and proliferation. A tumor cell's aberrant capacity for growth and proliferation can be derived in several ways: deregulation of cell cycle machinery, evasion of senescence and altered sensitivity to/need for proliferative signals. We discuss how mechanical cues regulate each of these in turn.
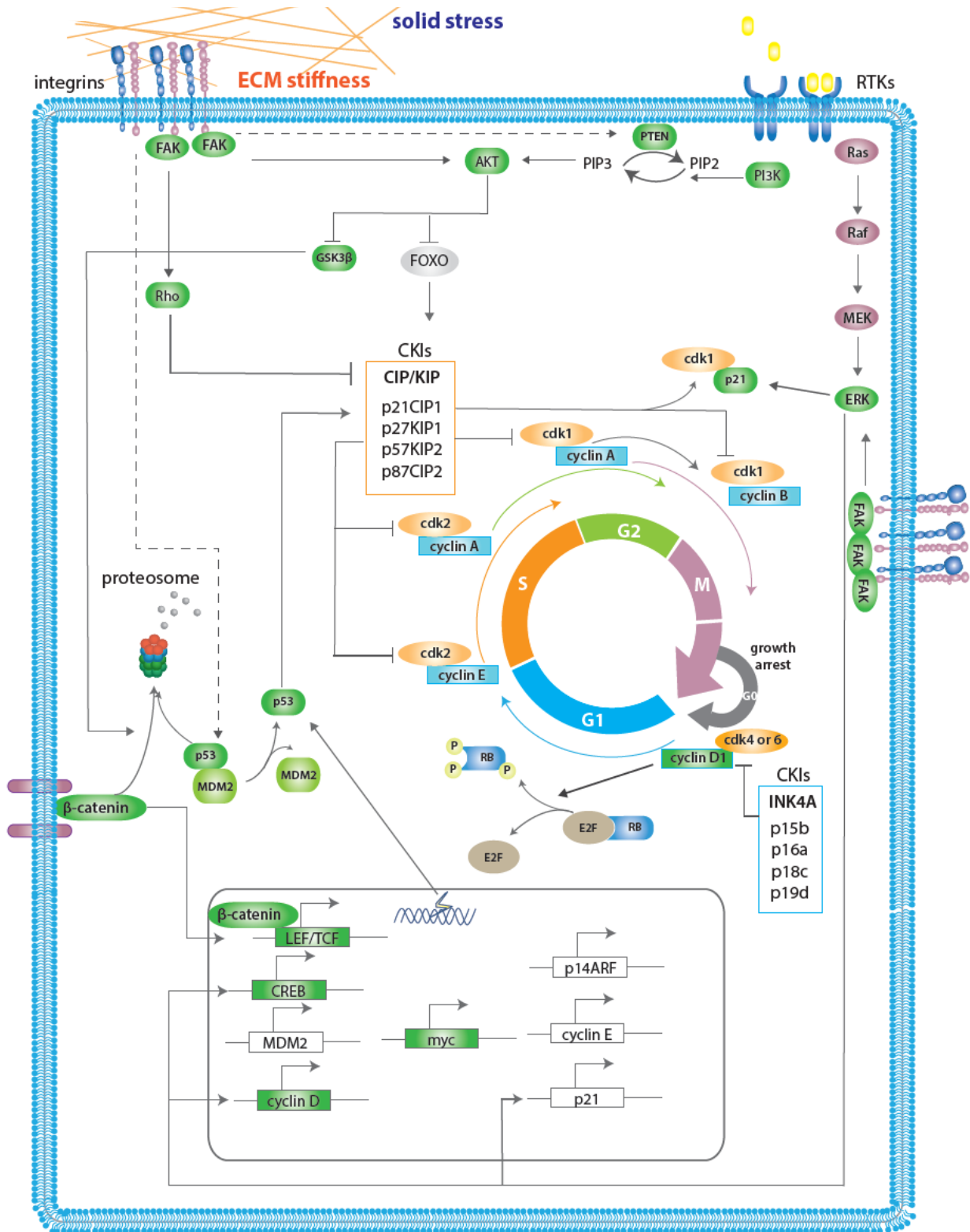
Figure 5.2. Mechanical regulation of cell growth and proliferation.

Overview of the interplay between mechanotransduction and growth and proliferation signaling. Proteins and genes in green have direct evidence linking their regulation to mechanical cues.

Deregulation of Cell Cycle Machinery

In order to achieve replicative advantage, tumor cells must overcome multiple layers of cell cycle regulation. The cell cycle is tightly monitored by a set of cyclin-cyclin dependent kinase (CDK) complexes at each juncture[212] (Figure 5.2). Transition from one phase to another depends on the presence of the correct CDK-cyclin complexes, in the correct activated/deactivated state[213]. CDK activity depends on interaction with cyclins, which are transiently expressed at necessary times during cell cycle[212]. These cyclin-CDK complexes are further regulated by CDK inhibitors (CKIs), which report on the state of events key to cell cycle progression, like DNA replication, and hence have their own inputs and controls. These regulators act through degradation of the cyclin subunit and activating or deactivation phosphorylation of the CDK unit. CKIs like p21, in turn, have a layer of transcriptional regulation by activators like p53[214]. Mutation, deletion, and overexpression of proteins in each layer of cell cycle control is found across many cancer types. Most of the components affected in cancer regulate either the late G1 or S phase checkpoint; a smaller subset regulate the G2/M checkpoint and even exit from mitosis[214].

One of the clearest links between ECM stiffness and regulation of cell cycle progression is through cyclin D1. There are many avenues through which matrix rigidity may be connected to cyclin D1 expression. In general, cyclin D1 expression is dependent on cell-matrix adhesion[215]. Integrin signaling is necessary not only for cyclin D1 expression but also regulates expression of CKIs p21[Cip1/Waf1] and p27[Kip1].[216] FAK- and Cas-dependent Rac activation due to substrate stiffness regulates cyclin D1 expression through lamellipodin, a component in actin cytoskeleton remodeling[217]. FAK and Src phosphorylation of p130Cas enables G1 progression via regulation of cyclin D1 expression[218,219]. Sustained ERK activity upregulates cyclin D1 expression[215] and increased ECM stiffness is linked to enhanced ERK activation through FAK, Src, Rho/Rho-associated protein kinase (ROCK), and Rac[188,207].

The Wnt/β-catenin pathway is another mechanism by which mechanical cues regulate growth and proliferation in cancer cells, particularly in colorectal cancer and leukemia[220,221]. Mutation in the *APC* gene is found in 80% of sporadic colorectal tumors; loss of its downregulation of β-catenin is considered the initiating event in colorectal tumorigenesis[222]. β-catenin activation and associated TCF/LEF gene

expression promote cyclin D1 and c-Myc expression to drive cell proliferation. Increasing matrix stiffness leads to breakup of E-cadherin containing cell-cell contacts, which frees previously sequestered β-catenin for nuclear translocation and transcription of target genes[223,224]. Independent of E-cadherin, both growth-induced solid stress and extracellular matrix stiffness have been shown to directly influence β-catenin activation and resultant malignant transformation and cell growth[196,197]. Mechanistically, myosin-mediated, ROCK-activated cell contractility as a result of matrix rigidity is found to induce β-catenin activation[225]. FAK-mediated Akt phosphorylation and resultant deactivation of GSKβ, itself an inhibitor of β-catenin, appears to underlie the connection between increased matrix stiffness and β-catenin signaling[197,225].

As alluded to above, myc transcription is also an important contributor to cell growth and proliferation. In fact, *MYC* is a widely expressed oncogene found in lung and breast carcinomas, leukemia, and neuroblastomas[226]. While implicated in transcriptional control of many genes, it is connected with activation of the phosphatase Cdc25, which removes inhibitory phosphates from Cdk2 to promote cell cycle progression. It also directly promotes cyclin-E/Cdk2 complex formation via removal of inhibitory p27^{Kip1} from the complex[227]. ECM stiffness has been found to increase MYC transcript and protein level in non-malignant epithelial cells[197]. In contrast, increasing ECM stiffness in neuroblastomas corresponded with downregulation of N-Myc expression and cellular proliferation[228].

Evasion of Senescence

Cellular senescence is a state of irreversible cell cycle arrest that can be induced when cells undergo oxidative stress, are exposed to oncogenic signals, or suffer DNA damage[229]. When senescent, cells can continue to grow in size (sometimes more than two-fold) as they produce proteins to fuel its heightened secretory state[229]. While ostensibly another way in which tumor cells subvert cell cycle control, activation of the senescence pathway has proven to be conserved across many cancer types[230,231]. It is one of the cell's first lines of defense against aberrant signaling through oncogenes. Indeed, senescence markers are observed in pre-malignant tumor cells but not in malignant ones[232]. Hence, tumor cells need to bypass senescence signaling in order to succeed.

Senescence is regulated by two major tumor suppressors, p53 and RB. p53 is a transcription factor that is lost or mutated in most human cancers and serves as a locus of senescence control, along with many other cellular functions, the list of which seems to grow longer every year[233,234]. It is typically short-lived in the cell, until its ubiquitin ligase, Mdm2, is sequestered as a result of cellular stresses[235]. At this time, p53 is stabilized and activates transcription of targets like CDKN1A/p21 and E2F7[236]. Both these targets then actively participate in the inhibition of cell cycle progression. p21 is a cyclin dependent kinase (CDK) inhibitor involved in G1 cell cycle arrest and E2F7 is a transcription factor responsible for turning on S-phase associated genes and driving cell proliferation[236–238].

RB, a part of the p16(INK4a)-Rb-E2F pathway, was originally discovered in the context of retinoblastoma and regulates G1 to S phase transition[235]. p16 inhibits CDK-4 and -6, which, when bound to cyclin D, phosphorylate RB[239]. Phosphorylated RB releases E2F family proteins to drive transcription of proteins necessary to S phase progression[239]. Hence, both p16 and Rb act as tumor suppressors by controlling cell cycle progression. In retinoblastoma, non-small cell lung cancer, breast cancer, and more, both p16 and RB function are inactivated through methylation, mutation, or deletion[230,231].

In addition to mutation and genetic silencing, mechanical cues can also interfere with these tumor suppressor pathways. Nuclear FAK can inactivate p53 by directly binding to both p53 and Mdm2, targeting p53 for proteasomal degradation[240]. Klein *et al.* showed G1 and S phase progression to be dependent on matrix stiffness[207]. At low stiffnesses, cyclin D1-dependent Rb phosphorylation is inhibited[207]. Shear stress, on the other hand, appears to drive cell cycle arrest. Osteosarcoma cells exposed to flow-induced shear stress exhibited altered expression in p21, cyclins A, D1, and E, and CDKs 1, 2, 4, and 6[241].

MECHANICAL REGULATION OF APOPTOSIS AND CELL SURVIVAL

Concomitant with an increase in growth and proliferation, tumor cells must be able to combat apoptotic signals that arise in response to their aberrant signaling state. In fact, carcinomas often exhibit mutations in both cell cycle and apoptotic regulators. Tumor achieve this through inactivation of apoptotic signaling or by upregulating pro-survival signaling. We discuss how mechanical cues regulate each of these mechanisms in turn.
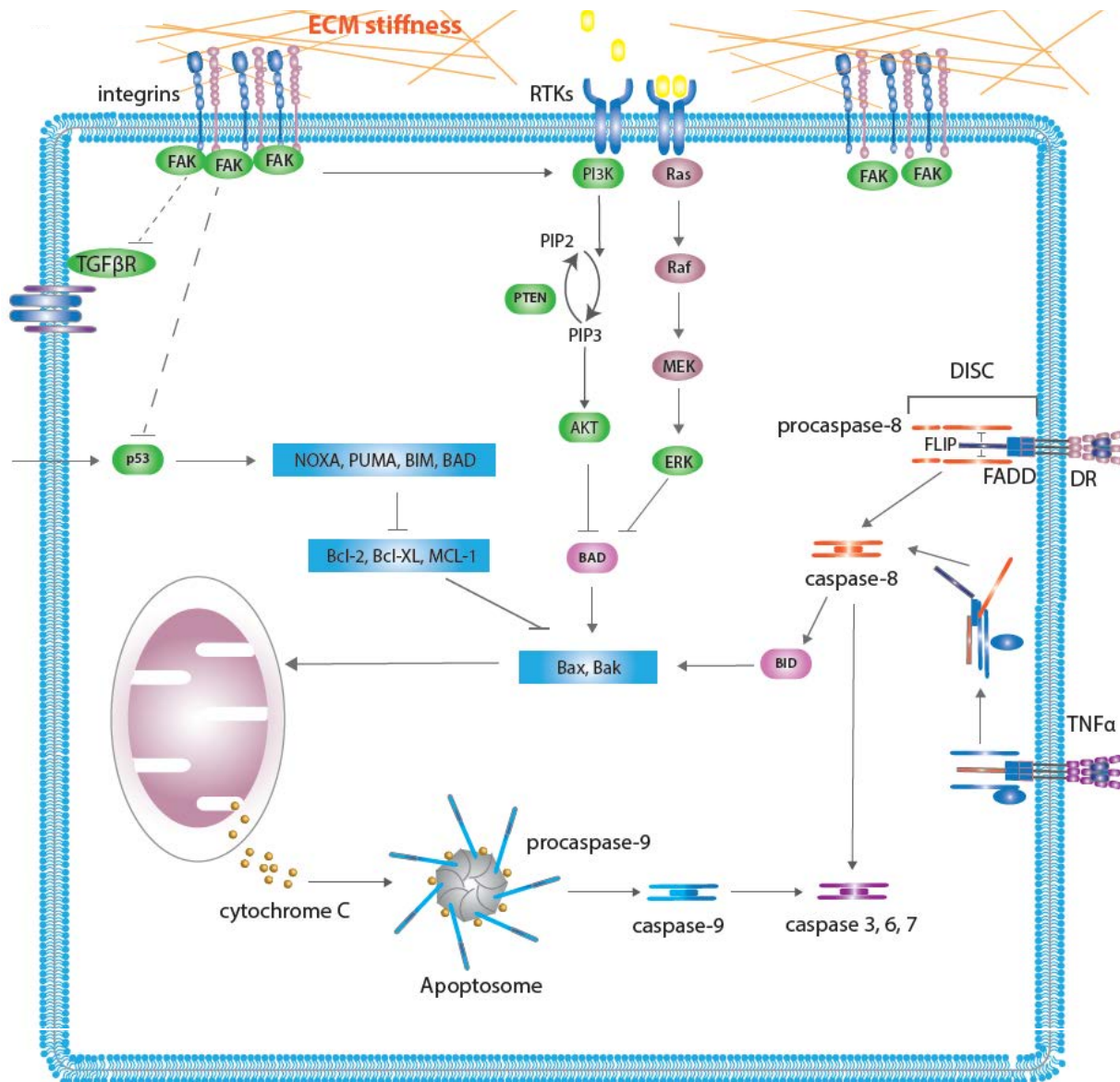
Figure 5.3. Mechanical regulation of apoptosis.

Overview of mechanical regulation of apoptosis signaling. Proteins and genes in green have been shown to be directly regulated by mechanical cues.

Inactivation of Apoptotic Signaling

Programmed cell death, or apoptosis, can be initiated through extrinsic (extracellular) or intrinsic (intracellular) signals (Figure 5.3). Death receptors at the cell surface bind to death ligands like TRAIL (tumour-necrosis-factor-related apoptosis-inducing ligand), recruit adaptor proteins to form a protein complex called the death inducing signaling complex (DISC). Cell cycle arrest due to DNA damage, cytokines, or oxidative stress can all activate the mitochondrial pathway, leading to release of cytochrome

c and formation of a protein complex called the apoptosome. In both cases, these protein complexes recruit and activate members of the caspase protease family. These initiator caspases then go on to cleave executioner caspases, starting a cleavage cascade that eventually reaches key cellular components like nuclear lamins and the actin cytoskeleton[242]. Apoptosis pathways are regulated mainly through the various caspases. FLIPs (FLICE(FAS-associated death domain (FADD)-like IL-1β-converting enzyme)/caspase-8-inhibitory proteins) bind to certain initiator caspases and block their catalytic sites to prevent death signal propagation[242]. Members of the BCL-2 family control the permeability of the mitochondrial membrane and thereby interactions between components of the apoptosome and other cellular components[242]. IAPs (inhibitor of apoptosis proteins) also bind caspases and specifically signal them for ubiquitin-mediated degradation. These regulators are in turn controlled through transcription and sequestration through protein-protein interactions[243,244].

In cancer, many components of apoptotic signaling are lost or mutated. Bax, a pro-apoptotic member of the BCL-2 family that increases mitochondrial membrane permeability to allow release of cytochrome c, is lost in many cancers[245–247]. Apaf-1 and Casp-9, both key components of the apoptosome, have been found to be mutated in tumor cells[248,249]. The death receptors TRAIL-R1 and -R2 are downregulated in head and neck and lung cancer. Interestingly, p53 is also involved in tumor cell's ability to avoid apoptosis. As previously mentioned, p53 is implicated in regulation of many cellular functions. It promotes cell death by regulating transcription of BCL-2 family members, Apaf-1, caspase-6, and death receptors[234,247–251]. Its mutation in tumor cells, in addition to preventing proper cell cycle control, also facilitates evasion of apoptosis. Hence, as with cell-cycle progression, FAK –mediated regulation of p53 degradation is also a means by which ECM rigidity can influence apoptosis.

While mechanotransduction pathways do not seem to directly regulate expression of caspases and apoptosome, mechanical cues mediate apoptosis through upstream activators of apoptotic signaling. Transforming growth factor-beta (TGF-β) acts as a tumor suppressor via activation of apoptosis, but is found to lose this suppressive capacity and drive epithelial-to-mesenchymal transition (EMT) in later stage tumor cells[252]. The transcription factor NF-κB is mutated in cancer and implicated in both apoptosis

repression and promotion, depending on context[253–257]. Its upstream regulators are also frequently lost or mutated in cancer[258]. Both TGF-β and NF-κB signaling are responsive to mechanical cues. Mechanical stretching induces conformational changes in and activates latent TGF-β1 bound to the extracellular matrix[259].The switch between TGF-β's tumor suppressive and EMT-promoting functions was shown to be stiffness regulated[252]. Specifically, increasing substrate rigidity resulted in nuclear translocation of the transcription factor TWIST-1, an initiator of the EMT program[260]. Not only is there significant crosstalk between mechanotransduction pathways and TGF-β effectors, TGF-β1 expression itself is regulated by substrate stiffness[261]. Additionally, ECM stiffness increases both expression and nuclear localization of Smad3, an effector of TGF-β signaling[261]. Similarly, nuclear translocation of NF-κB and hence its ability to turn on target genes is dependent on both cell shape and extracellular matrix rigidity[262,263]. Pharmacological studies indicated that this NF-κB activity in response to tumor necrosis factor alpha (TNFα) is increased with acto-myosin mediated cytoskeletal tension and signaling by RhoA and ROCK pathway[262,263].

Upregulation of Pro-Survival Signaling

In cancer, upregulation of pro-survival signaling is a major mechanism by which tumor cells subvert programmed cell death. Anti-apoptotic members of the Bcl-2 family (Bcl-2, Bcl-X_L, Bcl-W) are key pro-survival factors. The *bcl-2* oncogene facilitates cancer progression by promoting cell survival[66,242]. The PI3K/Akt/PKB cascade is another frequently dysregulated survival signaling pathway. This pathway can be perturbed via mutations in upstream receptor tyrosine kinases (EGFR, HER2, PDGFR), oncogenic mutation or upregulation of Ras, amplification of its effector, Akt, or loss of its suppressor, phosphatase and tensin homolog (PTEN)[264,265]. The PI3K pathway regulates apoptosis through multiple mechanisms. It can directly interact with and inactivate pro-apoptotic proteins, such as Bad, a Bcl-2 family member, or caspase-9. It also regulates NF-κB nuclear translocation and expression of caspase inhibitors via IKKα phosphorylation and represses p53-mediated apoptosis via phosphorylation of the ubiquitin ligase, Mdm2[266,267]. Activated Akt can activate mammalian target of rapamycin (mTOR) signaling, which drives

transcription of survival genes and is linked to repression of p53-mediated apoptosis[268]. The Ras/Raf/MEK/ERK pathway is another pathway involved in pro-survival signaling that is frequently dysregulated in tumor cells. A variety of inputs can activate Ras activation, including cellular stress and growth factor receptor signaling, and can be a point of deregulation of Ras signaling. Receptor tyrosine kinases like epidermal growth factor receptor (EGFR), for instance, experience high rates of mutation in tumor cells. Ras mutations are found in 20-25% of all tumors and is responsible for 90% of certain cancers, like pancreatic cancer[269]. Mutation in Raf, MEK, and ERK are also found in cancer cells. Activated Raf-1 increases expression of c-FLIP, a caspase-8 inhibitor. Phosphorylated ERK increases expression of Bcl-X_L, directly phosphorylates NFκB, and inhibits caspase-8 and -9 activation[270]. ERK phosphorylation of p90 ribosomal S6 kinase (RSK) inactivates Bad and regulates the transcription of cAMP response element-binding protein (CREB), which promotes cell survival via activation of c-Fos transcription[271].

Mechanical regulation of apoptosis is achieved through multiple points in the apoptosis pathway. $\alpha5\beta1$ integrin binding to fibronectin promotes cell survival by upregulating BCL-2 expression in CHO cells[272]. Signal transducer and activator of transcription 3 (STAT3) upregulates antiapoptotic members of the BCL-2 family and is constitutively active in many solid cancers[273,274]. Hepatocellular carcinoma cells cultured on stiff substrates demonstrated higher levels of STAT3 activation in the presence and absence of growth factor[206]. Stretching mammary epithelial cells produced similar increases in phosphorylated STAT3[275]. Precise mechanisms underlying this have yet to be clarified. Both PI3K and Ras-MAPK signaling are strongly affected by mechanical cues. Cells cultured on stiff matrices exhibit upregulation of PI3K and pAkt[118,204]. This appears to be dependent on both integrin clustering and crosstalk between the cytoplasmic tail of integrins and receptor tyrosine kinases[204]. ECM stiffness also enhances PI3K signaling by downregulating PTEN. Mouw *et al.* elucidated the molecular mechanisms underlying this regulation, demonstrating that FAK-dependent induction of miR-18a via β-catenin signaling by extracellular matrix stiffness reduced PTEN mRNA[197]. Crosstalk between activated integrins and receptor tyrosine kinases also results in increased Ras, Raf, and ERK activity[204,276]. Functionally, these signaling events correlate with

decreased cell death on stiff substrates and protection of cells from chemotherapeutics when exhibiting higher PI3K/Akt or ERK activation[277].

On a broader scale, interstitial fluid pressure plays a large role in controlling the flow of nutrients and mitogens in the extracellular space, and hence the availability of pro-survival signals to cells[194]. Direct cellular signaling in response to exposure to IFP and its effects on programmed cell death have yet to be reported.

CONCLUSION

There has long been discussion of the seed vs. soil question—what is the true driver of transformation—the cell's intrinsic genetic properties or the microenvironment's influence? In the context of our discussion, what causes there to be tumor-promoting mechanical cues? We know tumor tissue is stiffer, due to a combination of increased cell mass, matrix deposition, and matrix crosslinking. But which came first? The stiffened matrix or the tumor? These are all questions that remain unanswered, at least not completely. Transgenic mouse models of cancer and novel technologies have afforded researchers the ability to begin teasing apart these questions, but much work remains to be done. One intriguing hypothesis, put forth by Brock *et al.*, offers a tantalizing perspective on these questions. They suggest that tumor cells exhibit frequent state-switch due to genetic noise and that external factors, including the extracellular matrix, can exert pressures that push cells irretrievably in one direction. This idea is consistent with the fact that oncogenic mutations are often accumulated until a certain threshold is passed; it is also consistent with the observation that synergy between oncogenes and altered ECM properties is a stronger driver of tumorigenesis than either alone. In order to evaluate the validity of this hypothesis, researchers will need to generate models of cancer in which both genetic makeup and mechanical cues can be controlled. Fortunately, as this Review reflects, many mechanistic links between mechanical signaling and tumorigenesis have been elucidated. Once proper models exist, researchers will not lack for pathways to probe in their exploration of the interplay of oncogenes and mechanical cues in tumorigenesis.

Researchers' understanding of mechanical regulation of tumorigenesis is transitioning from correlative to causational. For decades, there have been parallels between how cells respond to stiffened environments and the types of signaling necessary to form a tumor. Recently, direct links between mechanical perturbations and tumorigenic cell behavior have been made. The emerging picture is one where mechanical cues from the environment work in tandem with an existing, vulnerable cellular state to push cells over the edge. Just as oncogenes need a permissive environment or other, cooperating mutations to achieve full transformation, mechanical cues alone also prove to be insufficient to effect malignancy. Instead, it appears that both environmental and genetic conditions must be in place for tumorigenesis to take place. With this in mind, it is clear that clinical interventions must take this paradigm into account when designing interventions. A succession of failed molecular therapies supports the notion that single points of entry into the morass of oncogenic signaling is often insufficient to revert the disease. Perhaps a combinatorial approach, where environmental and genetic contributions to tumorigenicity are addressed, will produce better results.

6 The Effect of Matrix Stiffness on Epidermal Growth Factor Receptor Signaling and Trafficking

MATRIX STIFFNESS AND GFR SIGNALING

For many years since the advent of molecular biology, soluble factor signaling was studied in isolation and widely regarded as the key to understanding cell function. The general consensus was that the cleaving, binding, and shuttling of small bits of information was the end-all be-all of cell biology. With the recent rise of the field of mechanotransduction, the study of the manner in which cells perceive and respond to the mechanical properties of its environment, our conception of the context in which this signaling takes place has changed. Studies of the cytoskeleton and the jungle of proteins that compose the ECM have revealed that there is a complex architecture around and within cells that defines the environment in which soluble factors interact. Cells, far from amorphous containers for proteins, sugars, and nucleic acids floating in a soup of the same substances, are structural units in an organized mesh of support. This landscape governs the transport and interaction kinetics of soluble factors and contributes its unique set of inputs for the cell to process. Given this, efforts have been made to examine the effect of these biophysical cues on established signaling pathways. One manifestation of this with particular relevance to cancer has been the investigation of the effect of ECM compliance on tumor growth and metastasis. Researchers have developed tools to characterize and manipulate ECM compliance and shown that not only do tumor ECMs have increased stiffness, but that this can be causally linked to tumor malignancy and progression.[188,278,279]

Studies into the mechanism by which ECM compliance controls cell behavior have highlighted the importance of putative mechanotransduction pathways. These signaling pathways were identified as being sensitive to and responsible for transducing information about the mechanical properties of the ECM into the cell. In reality, they more generally transduce information (mechanical and otherwise) about the ECM. Typically, these pathways consist of mechanosensors, proteins that undergo some change in response to mechanical forces. The most extensively studied group of mechanosensors is the integrins, cell surface receptors for ECM components like collagen, fibronectin, and laminin.[280] The integrin family consists of more than 20 distinct members with specificity for different ECM components.[280] When an integrin binds an ECM protein, it recruits intracellular components to nucleate focal adhesions, collections of scaffolding

and signaling proteins that connect the ECM to the cytoskeleton.[280] One mechanism by which the cell is thought to sense ECM stiffness is via the feedback between cytoskeletal tension and extracellular tension through focal adhesions.[77,281] Essentially, a tug-o'-war between the ECM and cytoskeleton occurs, where increased ECM stiffness drives Rho GTPase-dependent actin stress bundle formation and increased cell contractility to balance the extracellular tension.[282] In addition to effecting mechanical changes within the cell, integrin activation can also initiate signaling through canonical growth pathways. Focal adhesion kinase (FAK), which binds to integrins in focal adhesions, contains multiple Src homology 2 (SH2) binding sites commonly utilized by scaffolding proteins involved in tyrosine kinase signaling, such as in the Src and Ras pathways.[283–286] Alternatively, integrin signaling may interact with canonical growth and proliferation pathways downstream of Rho GTPase signaling. Rho-associated protein kinase (ROCK), for example, can increase Erk activation.[188] As researchers investigate further into the intricacies of mechanotransduction signaling, there is no doubt that further nodes of crosstalk will arise.

An orthogonal, and less frequently discussed, mechanism by which matrix rigidity can influence signaling in more "conventional" pathways is to change the context in which that signaling takes place. While increased matrix rigidity can drive many signaling events, it also induces physical changes in the cell, including those to cell shape, transport dynamics, and cytoskeletal organization. These changes may directly influence the process of signal transduction independent of signaling components like ROCK or FAK. The most well-known example of this is stretch-activated ion channels in sensory neurons, where mechanical deformation of ion channels leads directly to depolarization and signal propagation.[287] Understanding how matrix rigidity can affect intracellular signaling independent of mechanotransduction pathways can alter researchers' conception of how cells integrate physical and biochemical cues from their environment. This is of particular relevance to cancer biologists both attempting to understand cancer progression and to develop novel cancer therapeutic approaches. If matrix rigidity can modulate the activity of oncogenic or tumor-suppressing pathways, then researchers can use it both as a prognostic indicator and as a therapeutic target.

ErbB1 Activation

In order to evaluate whether matrix stiffness causes physical changes that alter the context of canonical intracellular signaling, it was important to identify a high-potential pathway relevant to cancer and conducive to detailed signaling analyses. The ErbB family of receptor tyrosine kinases (RTK), and ErbB1 in particular, is one of the best characterized RTK families in biology. ErbB1 and ErbB2 have been found to be overexpressed, amplified, or mutated in breast, gastric, lung, and brain cancer[288–293]. ErbB family members dimerize and autophosphorylate upon ligand binding and initiate proliferation and survival signaling through the Ras, Src, and PI3K pathways (Figure 6.1)[294–296]. Multiple tyrosine kinase inhibitors and function-blocking antibodies against ErbB1 have been developed and tested in clinical trials, with marginal success.[297–303] An alternative approach to modulating ErbB1 signaling in cancer may be to change the environment in which that signaling is taking place. Matrix stiffness has been shown to sensitize epithelial cells to EGF stimulation of ErbB1[188,278,304]. In comparisons of cells cultured on substrates of a range of stiffnesses, increased matrix rigidity correlated with increases in the magnitude and duration of signaling downstream of ErbB1 (Figure 6.2)[188,278,304].
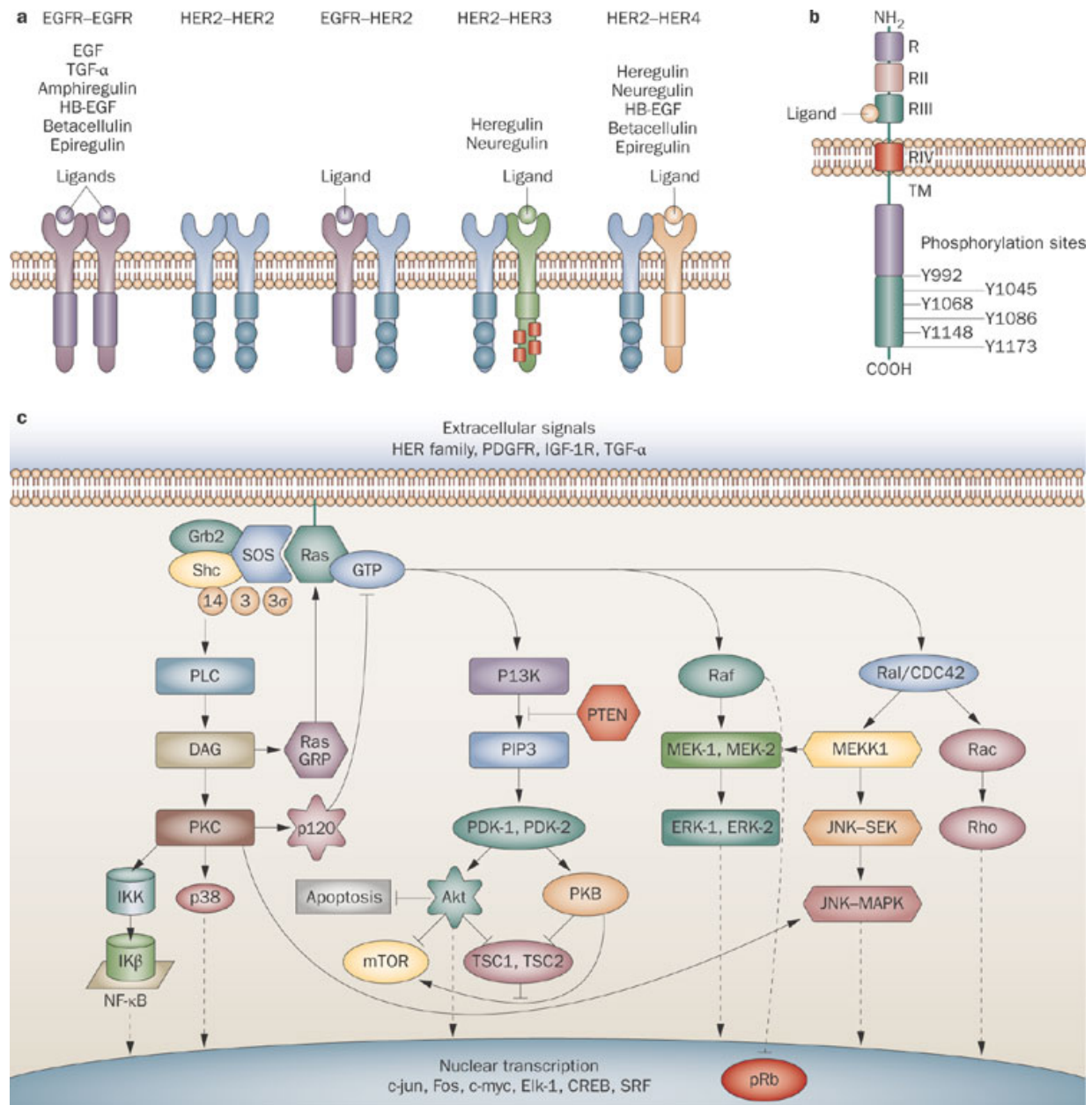
Figure 6.1. Overview of the ErbB family receptors.

a) Illustration of possible receptor interactions and ligand binding. b) Activation sites. c) Downstream signaling, including Ras, Raf, PI3K, and p38 pathways. From Linardou et al. [305]
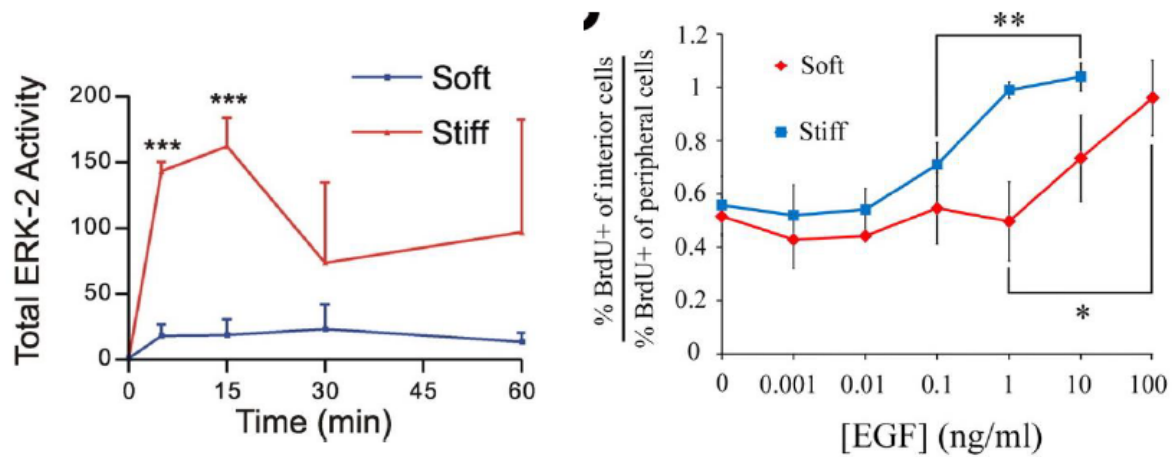
Figure 6.2. Matrix stiffness increases cell sensitivity to EGF treatment.

Evidence from literature that increasing matrix stiffness alters cell response to EGF stimulation. *Left: from Paszek et al.*[188] *Right: from Kim et al.*[304]

To confirm the effect of increasing substrate stiffness on signaling downstream of ErbB1, I collected lysates from cells cultured on soft (10–50Pa) and stiff (>60kPa) substrates at multiple time points after EGF stimulation, following overnight serum starvation. These lysates were then processed and run on SDS-PAGE gels to evaluate levels of ERK activation (Figure 6.3).
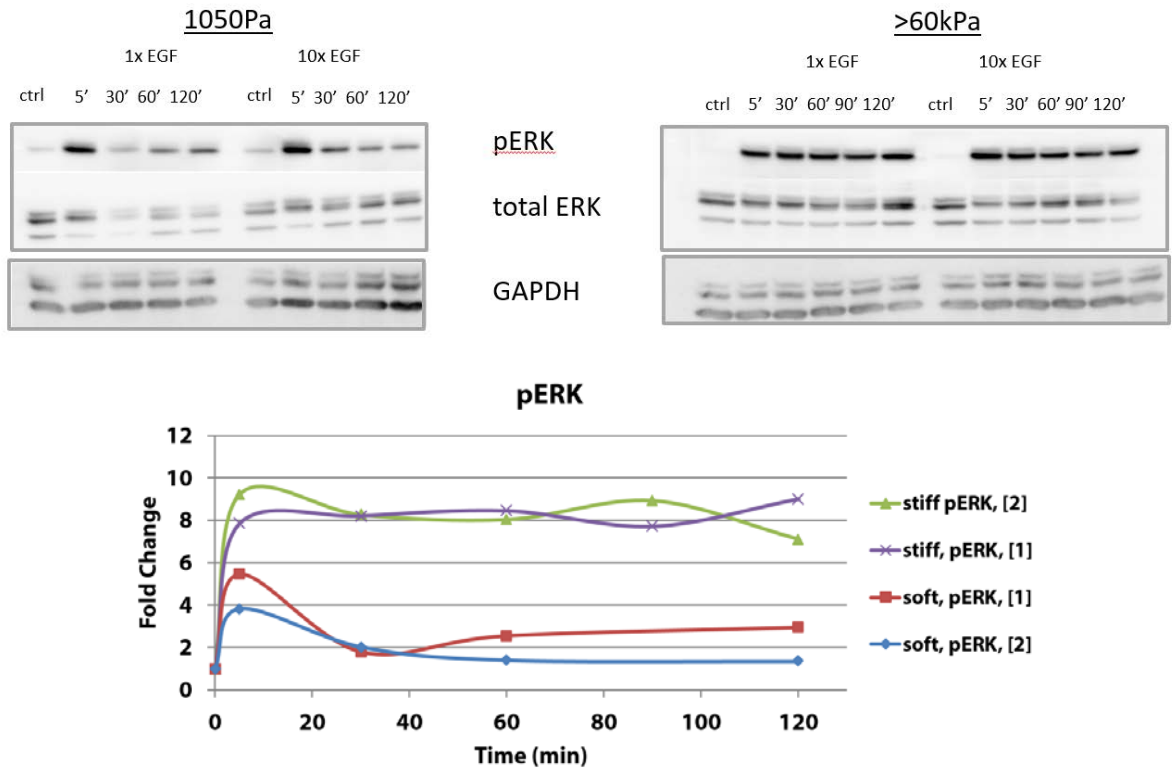
Figure 6.3. Validation of the effect of ECM stiffness on ERK activation in response to EGF treatment.
Immunoblots of cells on 1kPa and 60kPa polyacrylamide gels, serum-starved and stimulated with two concentrations of EGF.

As established in literature, cells cultured on stiff substrates demonstrate higher levels of pERK when compared to cells on soft substrates, as well as increased duration of this activation (Figure 6.3). Specifically, pERK levels remained at least 7 times baseline for 2 hours after EGF addition on stiff substrates, compared to soft substrates, where the signal returned to baseline levels after approximately 30 minutes. This pattern was consistent for two concentrations of EGF ($10\mu g/mL$ and $100\mu g/mL$).

Part of this increased sensitivity has been attributed to increased integrin activation on stiff substrates.[188] Integrin-mediated activation of ROCK has been linked to activation of ERK1/2, a downstream target of ErbB1 through the Ras/Raf/MAPK pathway (Figure 6.4).[188] However, employment of an integrin cluster mutant in cells on soft substrates recapitulated only the increase in the magnitude of ErbB1 signaling, not the prolonged duration observed on stiffer substrates (Figure 6.4).[188] This suggests that matrix rigidity acts on ErbB1 signaling via other mediators.
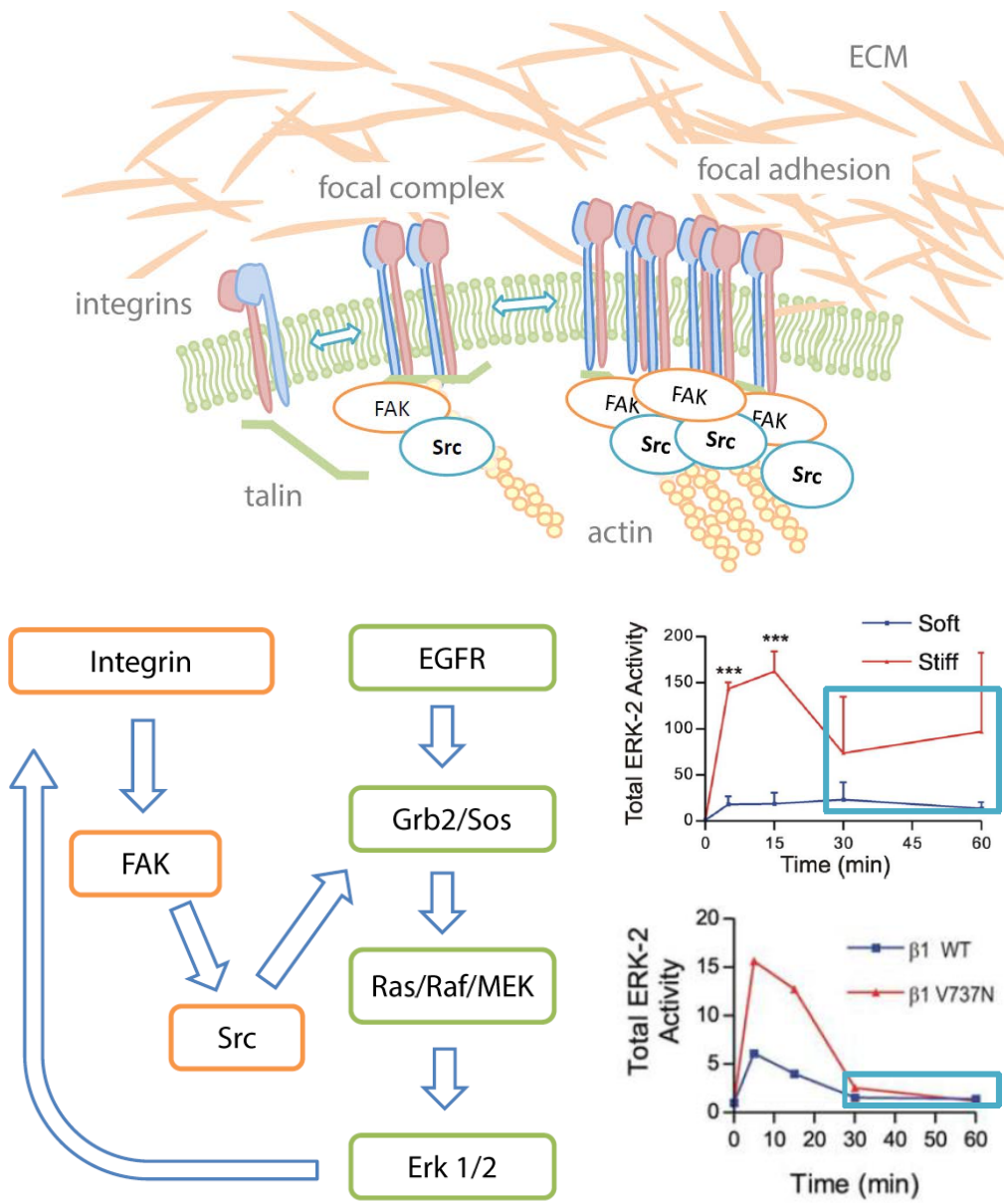
Figure 6.4. Integrin clustering and activation and activation downstream of ErbB1 signaling.

ERBB1 ENDOCYTOSIS

Ligand-induced receptor internalization is a regulatory mechanism used in ErbB1 signaling. While some studies have shown ErbB1 to maintain signaling capacity after internalization, its availability and propensity to bind downstream effectors changes as a result of uptake back into the cell.[306] Residence time of the activated receptor at the membrane plays a key role in determining the duration of a signal after initial ligand binding.[306,307] Previous work has shown that signal duration in the PI3K and MAPK pathways were altered in cells expressing internalization deficient ErbB1.[308] ErbB1 has been shown to be internalized with activated integrins and decreased rates of ErbB1 endocytosis can increase tumorigenic potential.[309] Changes in membrane tension, integrin internalization, and cytoskeletal organization can all affect the rate of receptor internalization. As such, a mechanism by which matrix rigidity can prolong signal duration downstream of ErbB1 may be by modulating ErbB1 internalization rates.
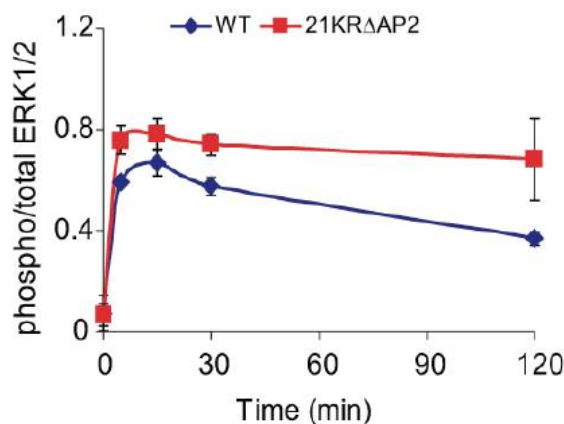
Figure 6.5. Mitigation of ErbB1 endocytosis influences duration of ERK1/2 activation. From Goh et al.[308].

In order to investigate whether substrate stiffness regulates receptor endocytosis, we used both biochemical and imaging assays. In our biochemical assays, we use a combination of biotin labeling and immunoprecipitation to quantify the amount of internalized receptor at specific time points after EGF stimulation (Figure 6.6).
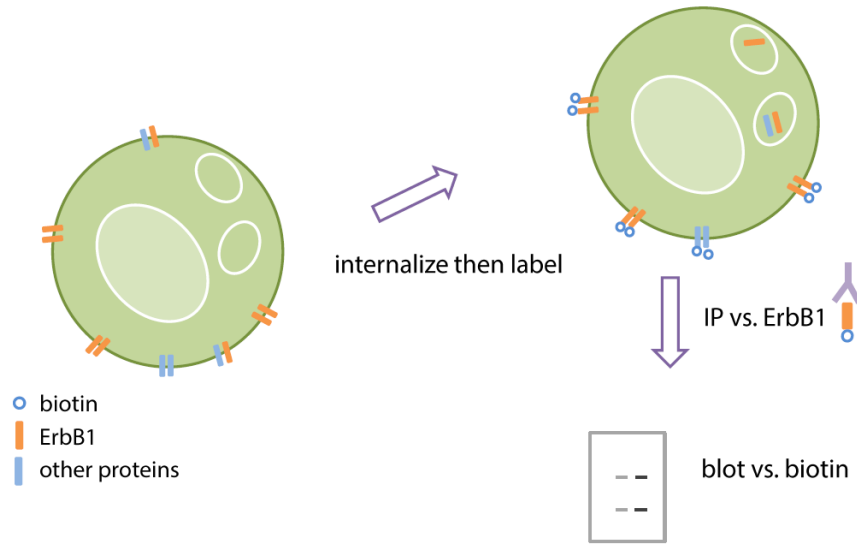
Figure 6.6. Schematic of biochemical assay.

These experiments suggest that increase ECM stiffness enhances the rate of ErbB1/EGFR endocytosis in

MCF10A cells (Figure 6.7).
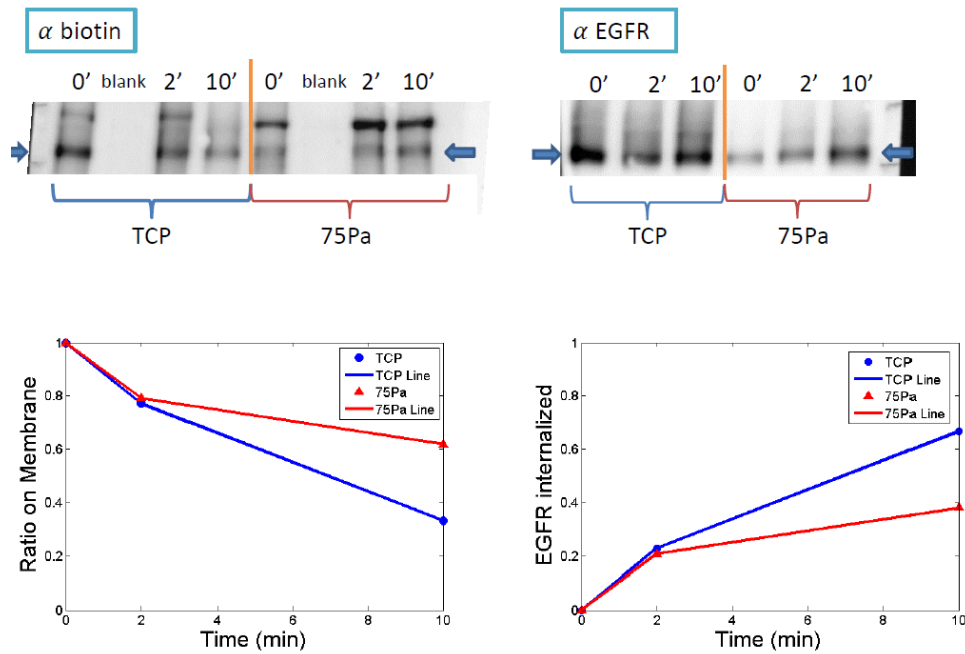
Figure 6.7. Increased substrate stiffness increases rate of ErbB1/EGFR endocytosis.

Top: Immunoblots of biotin and IP experiment. Bottom: quantification of immunoblot results.

Evidence from existing literature suggests that there is a dynamic interaction between ErbB1/EGFR and $\alpha5\beta1$ integrin. This includes data showing these two proteins are trafficked together and the fact that increased $\beta1$ integrin activation increases levels of pERK in cells.[195,309] To further explore this relationship, we treated cells on stiff substrates with the $\beta1$-integrin function-blocking antibody, AIIB2 and evaluated how this treatment changed the profile of proteins associate with ErbB1/EGFR after EGF treatment and the rate of ErbB1/EGFR endocytosis. First, using biotin-labeling and an anti-EGFR immunoprecipitation procedure, we find that AIIB2 treatment changes the membrane-associated proteins found in association with ErbB1/EGFR after EGF treatment (Figure 6.8). Mass spectrometry investigation of what these proteins are is currently underway.
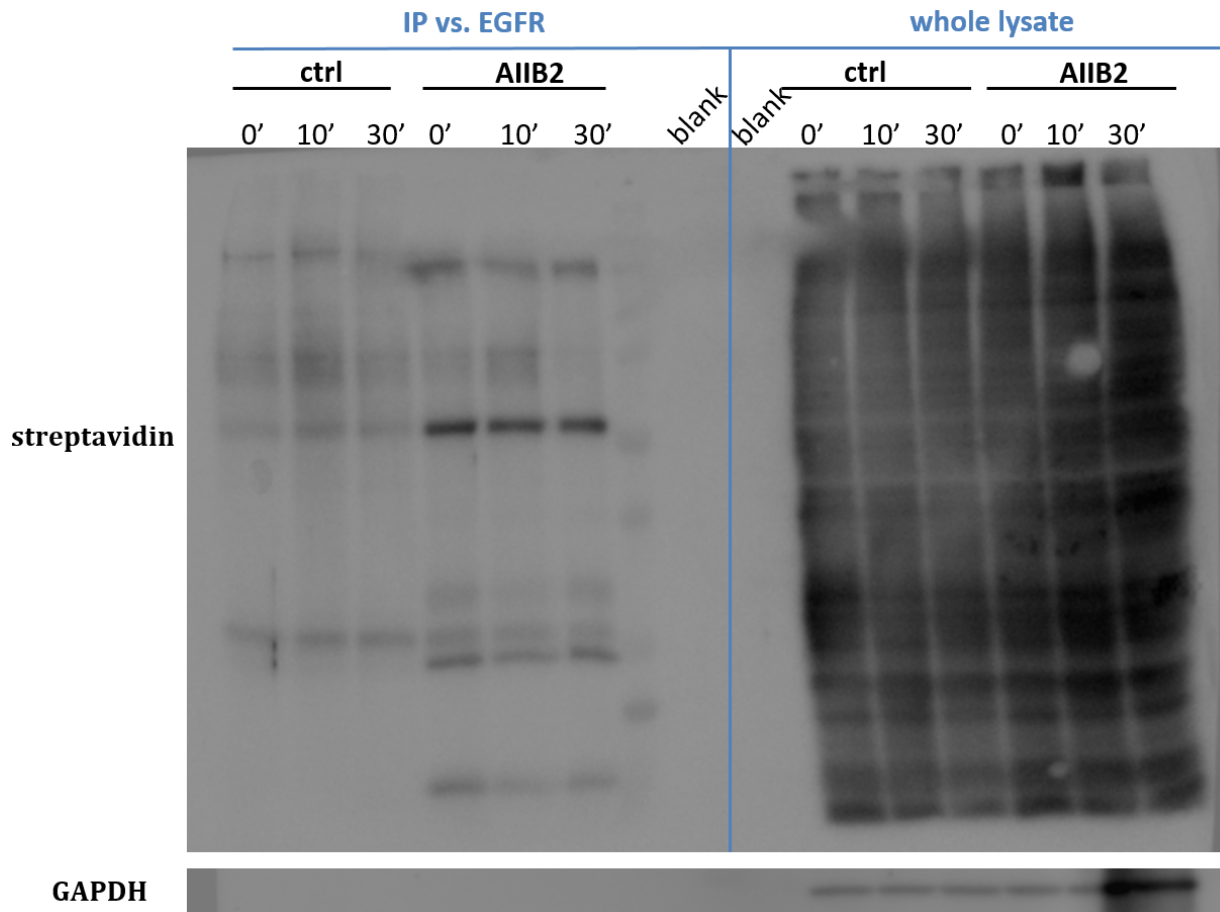
Figure 6.8. Proteins associated with ErbB1/EGFR changes with AIIB2 treatment.

Further, we were specifically able to identify that AIIB2 treatment appears to enhance association between ErbB1 and $\alpha5$ integrin, as well as caveolin-1 (Figure 6.9). Understanding the impact of these changes in association will require more detailed mechanistic studies that are currently being planned and executed.
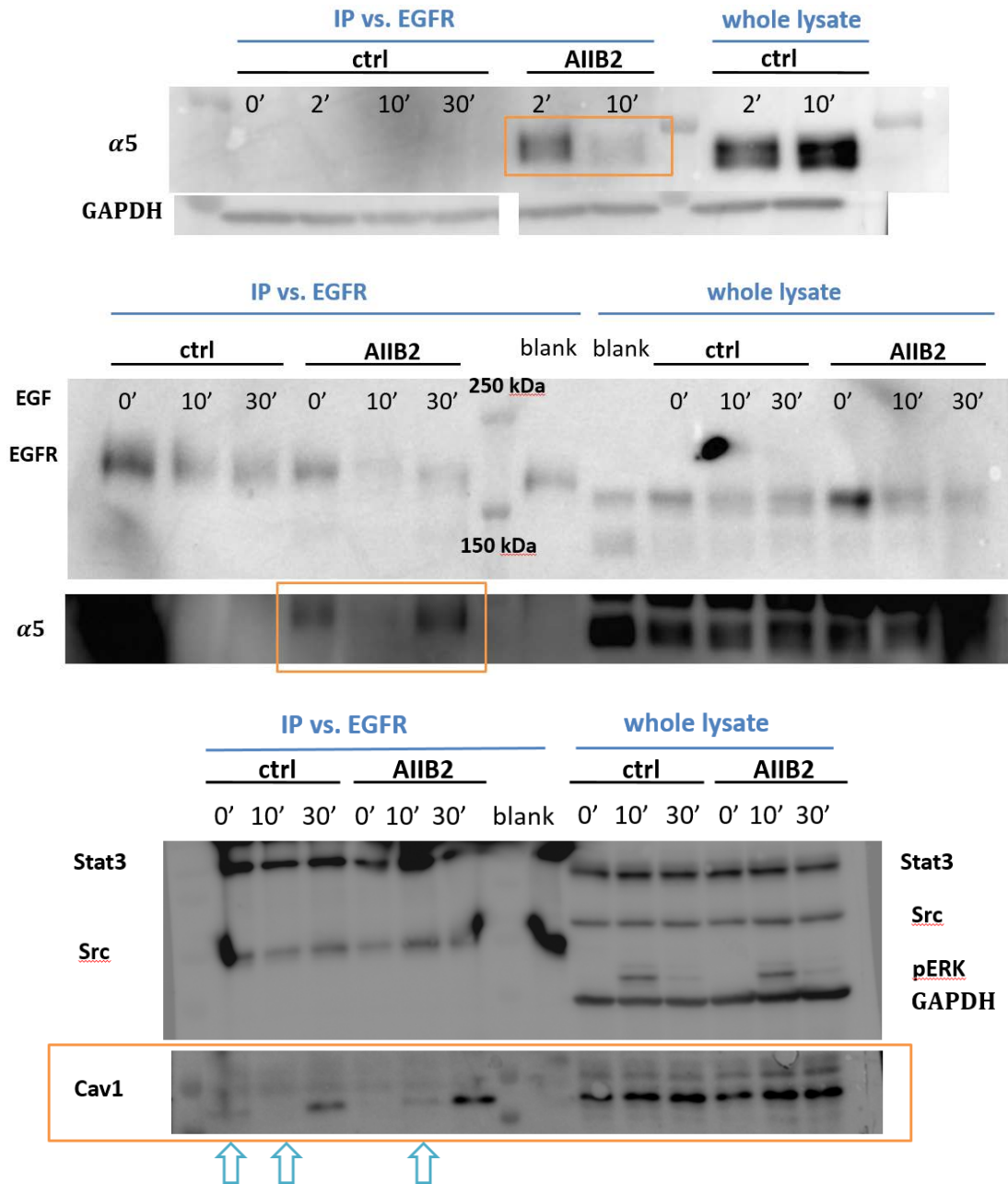
Figure 6.9. Immunoprecipitation of $\alpha5$ integrin and Cav1 with EGFR with and without AIIB2 treatment.

Top: Two independent immunoprecipitation experiments demonstrating different patterns of $\alpha5$ integrin association with EGFR when cells are treated with AIIB2. Bottom: Different time points for first association between Cav1 and EGFR with AIIB2 treatment.

We also employed EGFP-tagged ErbB1 and live confocal imaging as an orthogonal approach to studying the effect of ECM stiffness on ErbB1/EGFR endocytosis and protein association. Figure 6.10 provides an example of how we can observe appearance of endosomes after EGF stimulation of serum-starved cells.
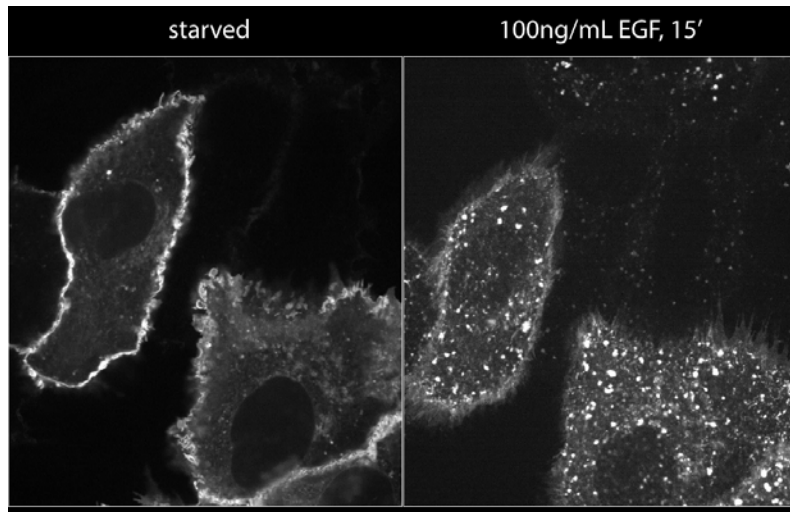
Figure 6.10. Imaging of EGFR endocytosis.

Example image of serum-starved (left) and EGF stimulated (right) MCF10A cells with EGFP-tagged ErbB1/EGFR.

These experiments confirmed our biochemical observations and showed that increase ECM stiffness increased the rate of endocytosis in MCF10As (Figure 6.11).
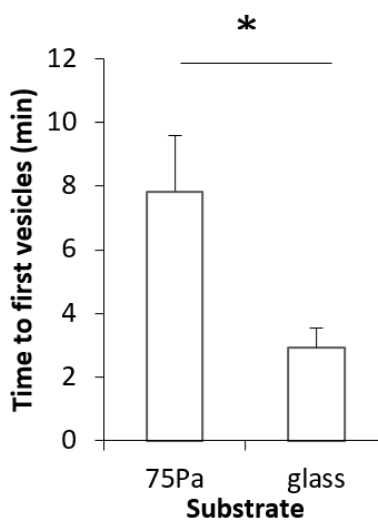
Figure 6.11. Analysis of live-imaging of ErbB1/EGFR endocytosis on soft and stiff substrates.

One obvious explanation for the difference in rate of endocytosis between cells on different stiffness substrates is the dramatic difference in morphology in these two contexts. Indeed, evaluation of the average size and number of trafficking vesicles under these two conditions suggests that while endosome size appears to remain constant across conditions, there is an increased number of vesicles in cells on stiff compared to soft substrates (Figure 6.12). This may be due to increases in cell size and spreading associated with substrate rigidity.
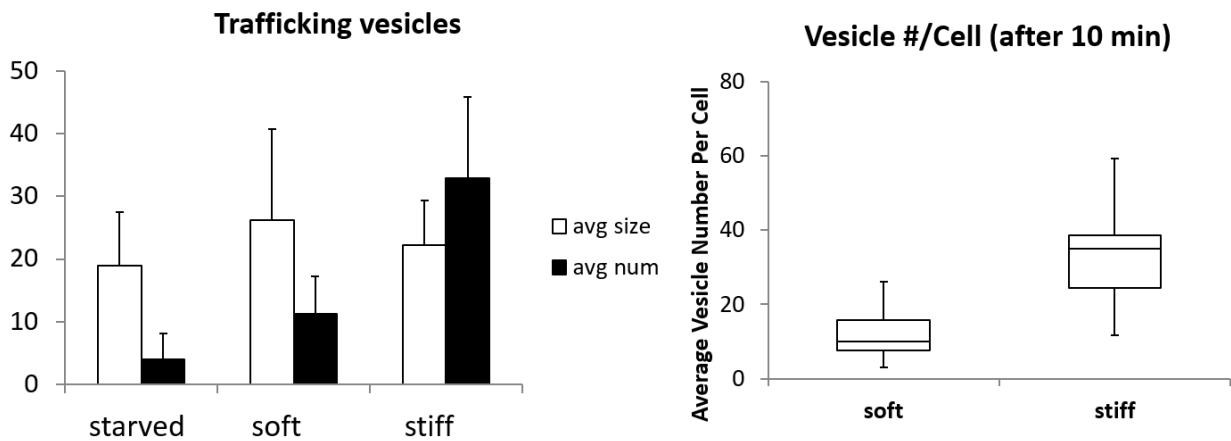
Figure 6.12. Vesicle size and density on soft and stiff substrates.
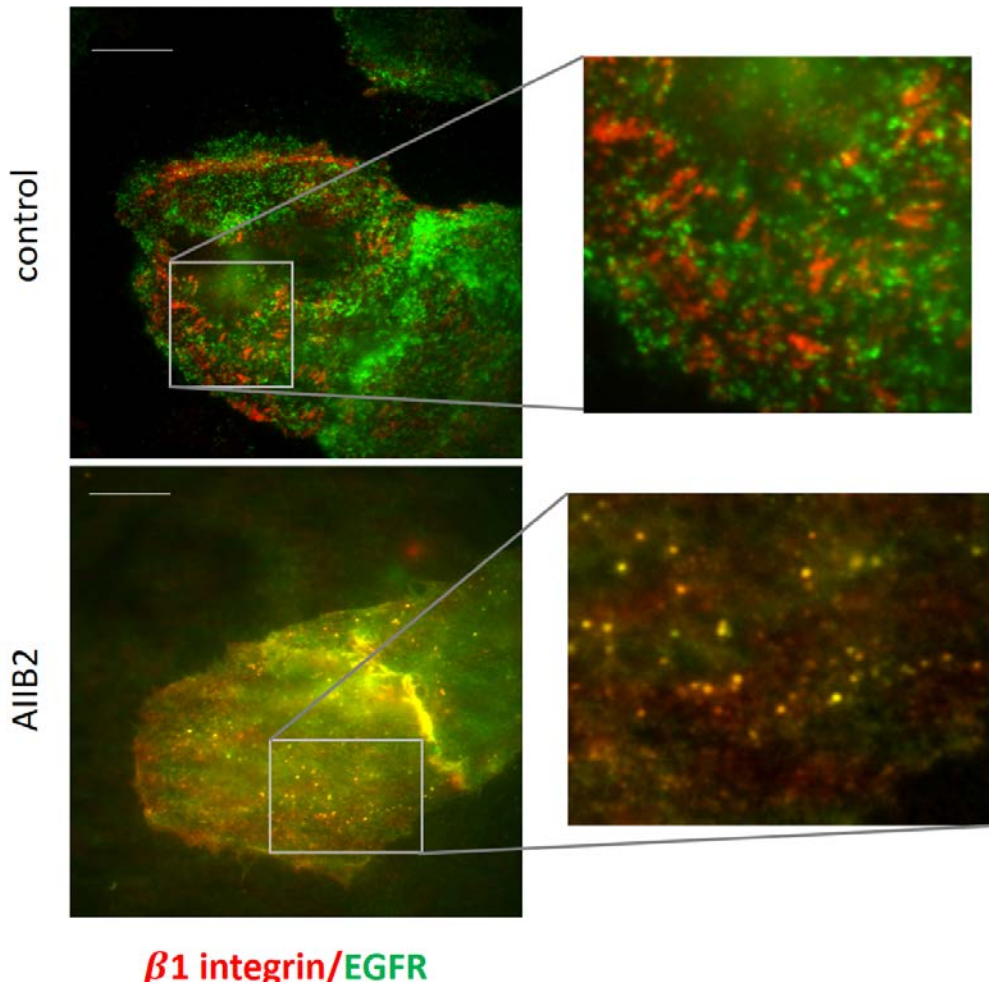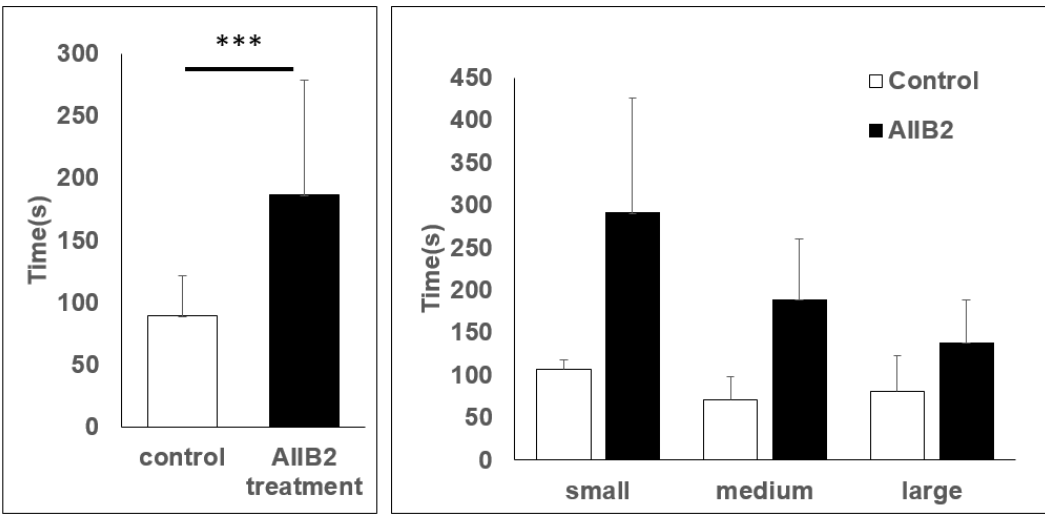
Figure 6.13. AIIB2 treatment.

Top: Colocalization of β1 integrin and ErbB1/EGFR with and without AIIB2 treatment. Bottom: Rate of endocytosis with and without AIIB2 treatment.

As in our biochemical studies, we exposed cells to AIIB2 treatment and observed resultant effects on $\alpha5\beta1$ integrin interaction with ErbB1 and ErbB1 endocytosis. These studies confirmed that AIIB2 treatment enhanced interaction between integrins and ErbB1/EGFR (Figure 6.13). Further, inhibition of integrin activity appeared to slow receptor endocytosis, suggesting a key role for integrin activity in enhancing ErbB1/EGFR internalization on stiff substrates. Interestingly, the rate of receptor endocytosis in AIIB2 treated cells correlated with cell size, such that larger cells were more immune to the effects of AIIB2 (Figure 6.13). This leads us to the same question as in untreated cells—does altered cell spreading due to changing substrate stiffness contribute to the changes in cell signaling we observe? To directly answer this question, we adapted micropatterned surfaces that allow mediation of cell spreading without changing substrate stiffness (Figure 6.14). We have been able to successfully seed single cells on these patterned islands of varying size and to perform real-time imaging of receptor endocytosis on these substrates. However, in order to control both substrate stiffness and cell spreading, we needed to develop a substrate that is both mechanically tunable and compatible with existing imaging techniques. This work is described in the next chapter. Our work in this area is thus on-going.
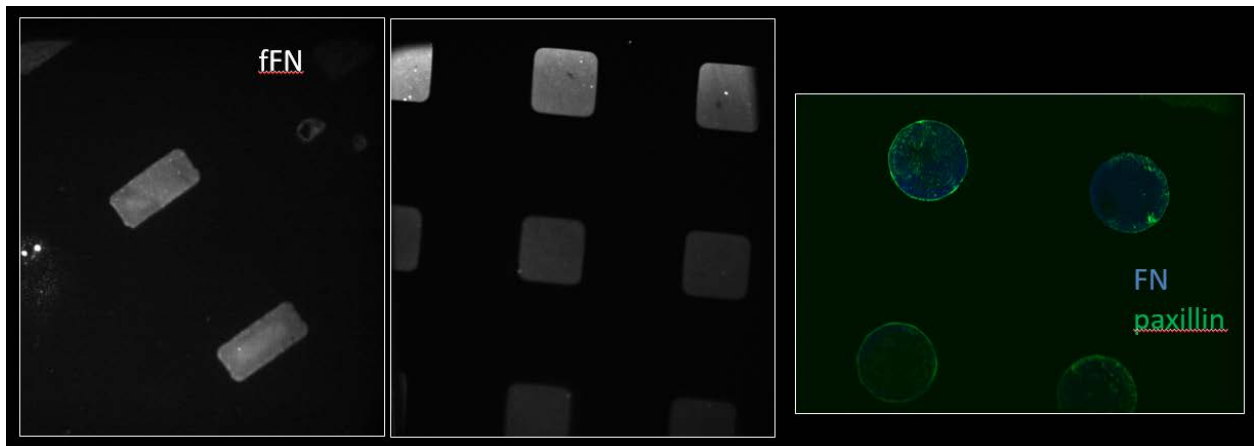
Figure 6.14. Micropatterned surfaces and cell attachment on these surfaces.
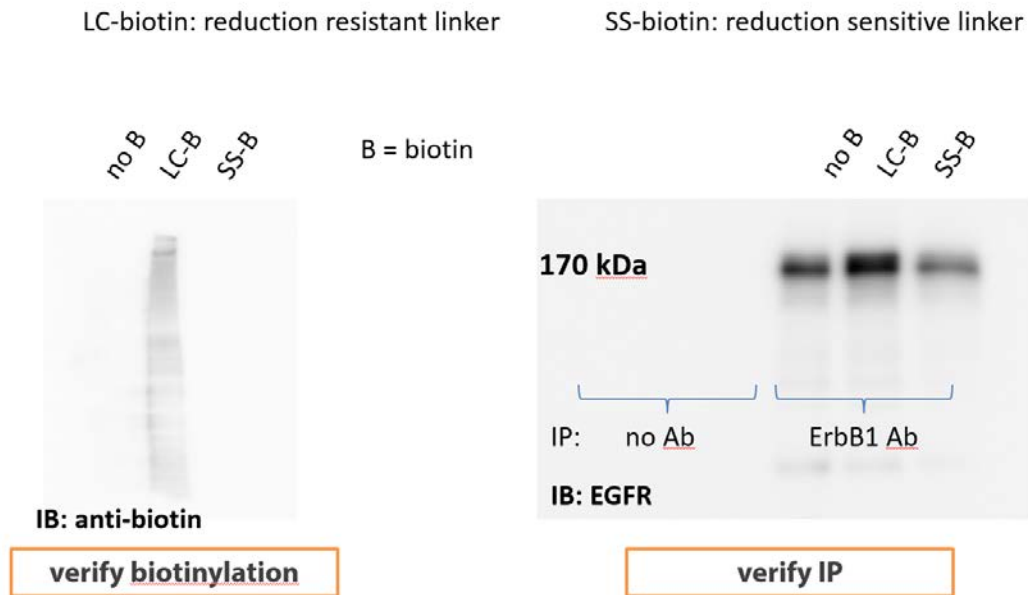
Figure 6.15. Validation of biotinylation and immunoprecipitation steps in biochemical endocytosis assay.

Left: validation of biotinylation of sample using LC (long chain) and SS (NHS-ester disulfide bonded to) biotin. Cells were treated with the indicated biotin (or no biotin) and then exposed to DTT, to cleave disulfide bonds. Lysates were subsequently collected and blotted with an anti-biotin antibody. We demonstrate that we are able to successfully label cells with biotin and to cleave off the susceptible form of biotin. Right: validation of immunoprecipitation with an anti-ErbB1/EGFR antibody. Cell lysates were treated with a control IgG or anti-EGFR antibody and then blotted with a second anti-EGFR antibody. Biotin treatment did not appear to hinder successful IP and only the anti-EGFR IP samples were positive for EGFR in the immunoblot.
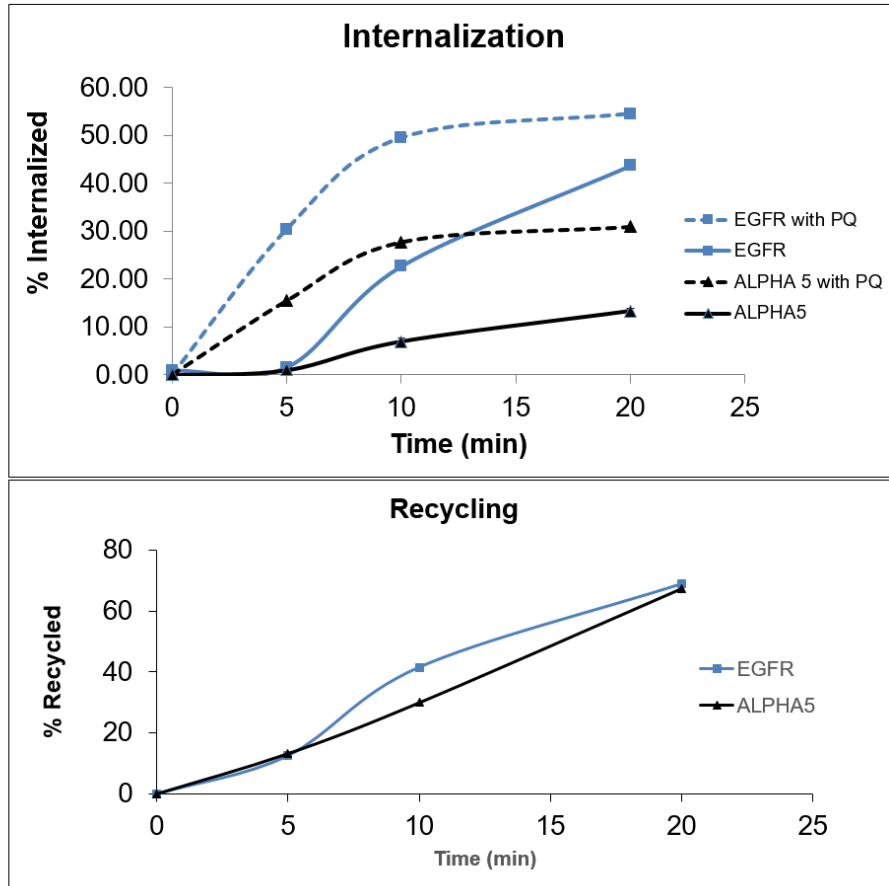
Figure 6.16. Validation of biochemical assay of protein endocytosis and recycling.

Validation of biochemical assay for quantification of receptor endocytosis. Cells were treated with primaquine (PQ), an inhibitor of cell recycling, to demonstrate the assay's ability to capture differences in levels of internalized protein. Two proteins were assayed to demonstrate adaptability of this method to multiple cell-surface proteins.
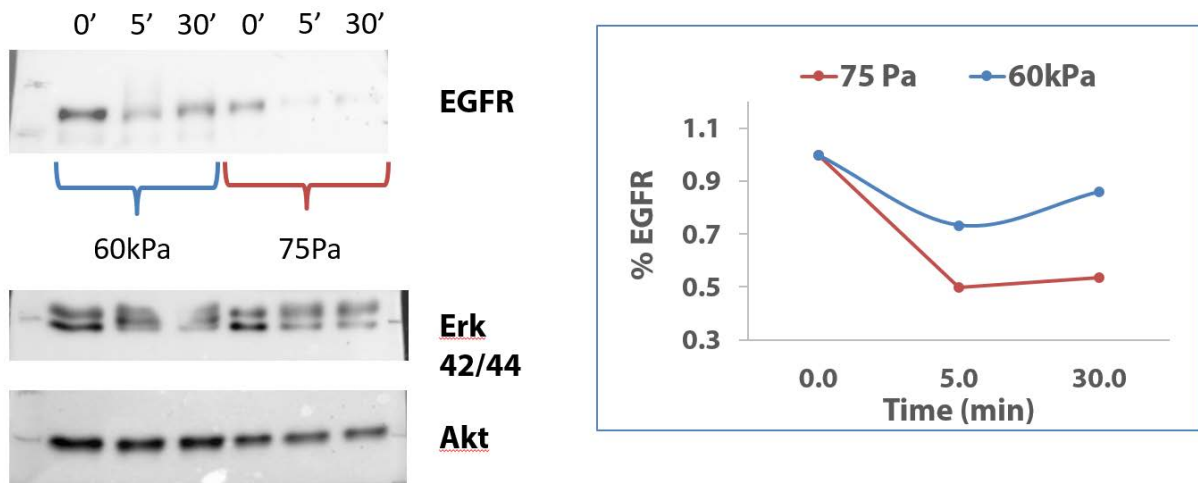
Figure 6.17. EGFR degradation on soft and stiff substrates.

Preliminary data indicating there is enhanced levels of ErbB1/EGFR degradation on soft substrates.

7 TOOL DEVELOPMENT: A MECHANICALLY TUNABLE SUBSTRATE FOR SUPER-RESOLUTION IMAGING OF ADHESIONS PROTEINS

The following work was done in collaboration with:

Dhruv Thakar, [b] Jason C. Tung, [b] Yekaterina A. Miroshnikova, [a,b] Christopher C. Dufort,[b] Edgar Gutierrez,[c] Alex Groisman,[c] and Valerie M. Weaver[a,b,d,e,f]

[a.] *University of California, Berkeley and University of California, San Francisco Joint Graduate Group in Bioengineering, San Francisco, CA, USA.*
[b.] *Center for Bioengineering and Tissue Regeneration, Department of Surgery, UCSF, San Francisco, CA, USA.*
[c.] *Department of Physics, UC San Diego, San Diego, CA, USA.*
[d.] *Department of Anatomy, and Department of Bioengineering and Therapeutic Sciences, UCSF, San Francisco, CA, USA*
[e.] *Eli and Edythe Broad Center of Regeneration Medicine and Stem Cell Research, UCSF, San Francisco, CA, USA*
[f.] *UCSF Helen Diller Comprehensive Cancer Center, UCSF, San Francisco, CA, USA*

Mechanical cues influence cell and tissue phenotype through a process termed mechanotransduction, in which receptors that bind extracellular matrix (ECM) molecules connect the cytoskeleton to the ECM and transduce information about the properties of the ECM via downstream signalling. This signalling can then induce changes in cell behaviour and fate. Engler *et al.* and Paszek *et al.* separately demonstrated the key role played by mechanical properties of the ECM in directing stem cell differentiation and malignant transformation, respectively.[310,311] Altering ECM stiffness can change cell proliferation, apoptosis, protein biogenesis, transcription, and more.[207,312,313] Researchers have made great strides in mechanistic understanding of this process with conventional cell and molecular biology approaches, which depend upon genetic mutants to elucidate the role played by various proteins in mechanotransduction[314,315]. Similarly, the employment of hydrogels and light microscopy has provided insight into how changing ECM properties influences subcellular organization of proteins.[316,317] More detailed mechanistic revelations, however, are contingent on our ability to visualize protein localization and interactions at a nanoscale level.

Super-resolution imaging has filled this need and permitted researchers to pinpoint the location of a labelled protein within the cell with nanometer precision. These methods have yielded studies that lend otherwise unattainable insight into the behaviour and organization of proteins within the cell. For example, Shroff et al. used photo-activated localization microscopy (PALM) to illustrate how paxillin is recruited to and disassociates from focal adhesion complexes.[318] Scanning angle interference microscopy (SAIM) led to characterization of how a bulky glycocalyx drives integrin clustering independent of acto-myosin contractility.[319,320] As interest in employing these methods to answer various biological questions grows, however, the need to adapt these techniques for biologically relevant experimental conditions arises. Cell and tissue elastic modulus can vary across multiple orders of magnitude, depending on type and location within the body.[310] The ability to mechanically tune the cell substrate *in vitro* can thus significantly enhance the physiological relevance of a study in question. As such, the ability to perform super-resolution imaging on mechanically tunable substrates would open up a new

avenue of investigation and facilitate greater understanding of the molecular mechanisms underlying mechanical regulation of cell signalling and behaviour.

Here, we report a novel approach to perform scanning angle interference microscopy (SAIM) for nanoscale imaging of subcellular components on mechanically tunable substrates. This system offers nanoscale precision in pinpointing fluorophore localization while affording control over the mechanical properties of the cell substrate. We provide detailed description of this novel imaging approach, key changes to optical theory and associated image analysis software, validation of the gel properties and cellular responses, and example applications for the platform in imaging cell-matrix adhesions. This method has great potential for adaptation in any study where ECM rigidity may play a role and allows researchers to benefit from advances in technology without sacrificing physiological relevance.

EXPERIMENTAL SETUP

In this section, we describe the experimental setup involved in utilizing this imaging platform, from silicone gel coating onto the imaging surface to image acquisition and analysis.

SAIM Background

Scanning angle interference microscopy is described in detail by Paszek *et al.*[321] To provide context for the steps detailed below, we briefly describe its origins and underlying theory here.

SAIM is an improvement of fluorescence interference contrast microscopy (FLIC), which uses surface-generated structured illumination to achieve z-super resolution.[322] In traditional FLIC, silicon wafers with different thickness silicon oxide layers are used. The interference pattern generated when light is reflected from these surfaces interacts with fluorophores situated on oxide layers of different thicknesses in predictable patterns.[322] For example, a fluorophore at a height corresponding with constructive interference will register higher fluorescence intensity than a fluorophore at a height corresponding with destructive interference. By assembling data about these fluorophores' relative positioning to the interference pattern, it is possible to calculate their absolute

height above an imaging surface.[323] In SAIM, on the other hand, vertically varied patterns of illumination are generated by changing the incidence angle of excitation (Figure 7.1c).[321] As with FLIC, a silicon wafer with a defined thickness of silicon oxide is used. However, in SAIM, only one thickness is needed, thereby simplifying substrate preparation.

Preparation of imaging samples

Substrate Preparation Silicone (or polysiloxane) gels have previously been spin-coated in thin layers (5-10μm) for use in TIRF.[324,325] Polymer to crosslinker ratio can be varied to obtain silicone gels of different stiffnesses.[324] The ability to deposit thin layers of these gels facilitates their adoption for use in sensitive imaging techniques. We adapt these mechanically tunable gels for mechanobiological studies using scanning angle interference microscopy. In order to coat silicon wafers with a silicone gel, we spin coated unpolymerized gel solution at 8000 rpm for 90 seconds. *N*-type (100)-orientation silicon wafers with 300nm or 1.9μm silicon oxide (Addison Engineering) were cut into 1cmx1cm squares and cleaned in acetone, potassium chloride, and water in sequence, while sonicating, for 20 minutes each. Silicon wafer and silicon oxide deposition methods were unchanged from Paszek and colleagues' original description.[321] Mixed and degassed gel solution (Corning 52-276 Parts A and B at ratios corresponding with desired stiffness) was deposited on wafer squares using a small pipet tip or dropper before commencing the spin coating program (VTC-100, MTI Corporation). The resulting substrates were then baked at 60°C for 3 hours. To conjugate ECM proteins to the substrate surface, gels were incubated with 95% ethanol, 0.5% (3-aminopropyl)trimethoxysilane (Sigma-Aldrich) solution for 5 minutes, then 100μg/mL 1-Ethyl-3-(3-dimethylamino-propyl)carbodiimide (EDC, TCI America) + 10 μ g/mL human plasma fibronectin (Millipore) for 30 minutes while shaking at room temperature. At this point, samples could be stored for 1 week at 4°C or immediately used for cell seeding (Figure 7.1a and 7.1b).
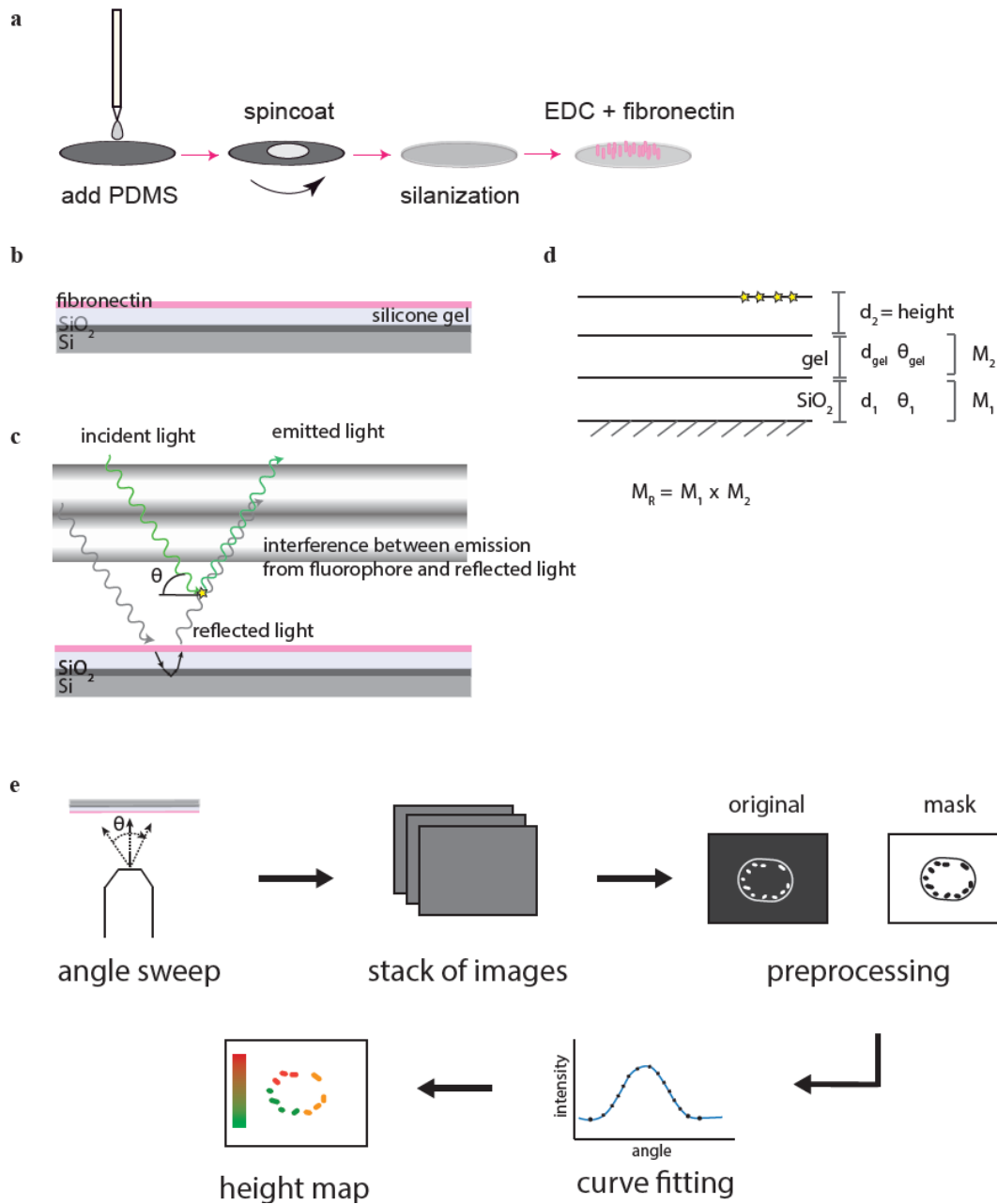
Figure 7.1. Experimental setup

a) Spin coating and activation procedure. b) Gel and silicon wafer layout. c) Optical theory behind scanning angle interference microscopy (SAIM). Reflected excitation light interferes with emission from fluorophore in a manner that is dependent on the angle (θ) of incidence of excitation light. This interference pattern can be used to calculate the height of a fluorophore situated above the substrate surface, as illustrated in d). Here, we consider the silicon oxide as one layer and the gel as another layer. Knowing the thickness (d_1 or d_{gel}) of the materials and angle of light passage (θ) through these materials allows us to construct transfer matrices (M_1 and M_2) and solve for d_2, the fluorophore height. Adding multiple layers together means multiplying their respective transfer matrices to obtain a system transfer matrix, M_R See text for full derivation. e) An overview of the acquisition and analysis process. A sample is imaged at multiple angles of incidence, producing a stack of images in which each image corresponds with one angle of incidence. This stack is used to generate a mask of regions and feature of interest, which is then used by the analysis software to determine which pixels to analyze. The software compares experimental intensity vs. incidence angle curves to those predicted by optical theory and finds the best fit for each pixel. The output of this analysis is a height map that reflects the best fit angle for each pixel indicated in the mask.

Calibration Samples To conjugate fluorescent microspheres onto the gel surface for use in calibration, gels were plasma treated (PDC-32G Plasma Cleaner, Harrick Plasma for 30 seconds after polymerization and incubated with 20μL of a 1 in 10^6 dilution of 0.1μm red fluorescent carboxylate-modified microsphere solution (Molecular Probes, Invitrogen) in the dark until dry.

Cell Samples MCF10A human mammary epithelial cells were cultured as previously described.[321] To generate cell lines stably expressing paxillin-mCherry, paxillin-eGFP, or vinculin-eGFP, HEK-293T cells were transfected with lentiviral vectors. Recombinant lentivirus was then collected and used to transduce MCF10A cells. Resulting cells were selected in media containing 200ng/mL G418 for 48 hours. Infection efficiency was verified via epifluorescence and brightfield microscopy 24 hours after doxycycline treatment. Only cell samples with >75% positive fluorescently expressing cells were used in experiments.

Cells were seeded on fibronectin-conjugated substrates on the day prior to fixation or live imaging and allowed to adapt to the gel substrate for a minimum of 18 hours. Cells used for focal adhesion or cytoskeletal component imaging were fixed in 4% paraformaldehyde in 1X Cytoskeletal Buffer (10mM MES pH6.1, 140mM KCl, 3mM $MgCl_2$, 2mM EGTA) supplemented with cold 11% sucrose on the day of fixation. Non-cytoskeletal component imaging samples were fixed in 4% para-formaldehyde in PBS. In both cases, cells were fixed for 15 minutes at room temperature, washed 3 times in cold PBS, and permeabilized in 0.1% Triton-X 100 in PBS for 10 minutes. Cells were then washed three times for 15 minutes each and blocked in 1% BSA in PBS-Tween (0.3%) for one hour. Primary antibody was incubated in blocking solution overnight at **4**°C. Secondary antibody was incubated in blocking solution for 1 hour, preceded and followed by three 15-minute PBS washes. Live cell imaging was achieved in an environmental chamber, at 37°C and 5% CO_2. Culture media was exchanged for imaging media (with no phenol red), to reduce background signal.

Rheology and Image Acquisition and Analysis

Shear Rheology, Shear rheology was performed on an Anton Paar Rheoplus 32 with an 8mm probe (PP08/S-SN22031). A curing test was performed at 60°C, where a 5% strain test was performed every 60 seconds until storage and loss modulus values changed by less than 1% for three consecutive time points (Figure 7.2). A frequency sweep between 0.5-10Hz under controlled shear deformation was then performed on the cured samples to obtain steady state storage and loss moduli. Complex modulus was then calculated using the following formula: $G^* = \sqrt{G'^2 + G''^2}$.

TIRF and SAIM Our imaging setup consisted of a Nikon inverted TIRF microscope system (Ti-E Perfect Focus System), with 488-nm and 561-nm lasers and an electron-multiplying charged-coupled device camera (EMCCD, QuantEM 512, Photometrics). Linear light polarization was achieved as previously described.[321] To accurately correlate motor position of the TIRF illuminator with effective incidence angle of excitation, manual calibration was performed prior to each imaging session. The TIRF motor was moved to twenty-five evenly spaced out angles between -50° and +50°, and the corresponding motor position was recorded. As these angles were measured in ambient air, their corresponding angles in aqueous solutions was calculated using Snell's Law. The relationship between motor position and incident angle was fitted using a power law and the resulting equation used to calculate appropriate motor positions for acquisition angles, which ranged from -45° to +45° at 0.5° intervals. These motor units were entered into a journal in the microscope controller software (Metamorph).

Atomic Force Microscopy and Scanning Electron Microscopy Images were acquired using a MFP3D-BIO inverted optical AFM (Asylum Research, Santa Barbara, CA) mounted on a Nikon TE200-U inverted fluorescence microscope (Melville, NY) in non-contact imaging mode. Silicon nitride cantilevers (k=0.09N/m, Olympus TR400PB) were calibrated for each session using the thermal oscillation method. Images shown are height maps of 30μm×30μm areas. All images were acquired on fresh non-fixed cells in cell culture media. For SEM, silicone gels were fixed in 1.5%

glutaraldehyde/1% paraformaldehyde and impregnated with a conductive layer of osmium-thio-carbohydrazide-osmium (OTOTO). The gels were then dehydrated in a graded series of ethanol, followed by critical point drying procedure with an AutoSamdri 815 critical point dryer (Tousimis, Rockville, MD). Subsequently, the gels were imaged on JEOL JCM-6000 Neoscope Scanning Electron Microscope (JEOL USA Inc., Peabody, MA).

Image Analysis TIFF stacks with one image corresponding to each incidence angle were processed in FIJI (NIH).[326] Stacks were z-projected with standard deviation to create a composite image, which was then binarized to generate a mask (Figure 7.1e). Individual TIFFs were saved for each image in the stack and input into the analysis software, along with the mask and a parameter file (Figure 7.1e). Raw fluorescence intensity profiles were generated in FIJI for 5 pixel x 5 pixel regions of interest and points of inflection were counted and compared with theoretically generated fluorescence intensity curves (Figure 7.3a and 3b). A best guess for silicone gel thickness (d_{gel}) was determined based on this comparison and input into the analysis software (Figure 7.1d). Both uncompiled analysis code and an example parameter file are provided as supplementary material. Analysis software was written in C++ and compiled in a Linux operating system. It makes use of the Intel Math Kernel Library for curve fitting. Visualization software was written in Python using libraries distributed by Enthought, Inc. Statistical analysis was performed in Microsoft Office Excel 2013.

To evaluate the success and utility of our novel imaging platform, we identified four major design requirements:

1) the silicone gel should be mechanically tunable within a physiologically relevant range,

2) the substrate should be compatible with cell culture,

3) the silicon wafer and gel substrate should be compatible with the optical requirements of TIRF and SAIM, and

4) the new imaging system can be used to make observations about biological systems.

We address each of these design requirements in turn, in the following sections.

Substrate Rigidity and Cell Responses to Silicone Substrate

Substrate Characterization To characterize the range of elastic moduli attainable using these silicone gels, we mixed Parts A and B of the silicone gel at varying ratios and performed shear rheology on the resulting bulk gels (Figure 7.3a). It is possible to generate gels from 250Pa to 100kPa, a broad range that spans the physiological range (which ranges from <1kPa in the brain to 25k-100kPa for in muscle and bone.[310,327] To further ensure the gel's compatibility with imaging requirements, we performed atomic force microscopy (AFM) and scanning electron microscopy (SEM). AFM allowed us to characterize the gel surface. Both TIRF and SAIM require relatively flat surfaces that do not induce distortions in light path. AFM imaging revealed that the gel surface had <10nm variation in height (Figure 7.3b). SEM suggested similar levels of roughness on the gel surface further permitted us to measure gel thickness (approximately 8μm, Figure 7.3c).
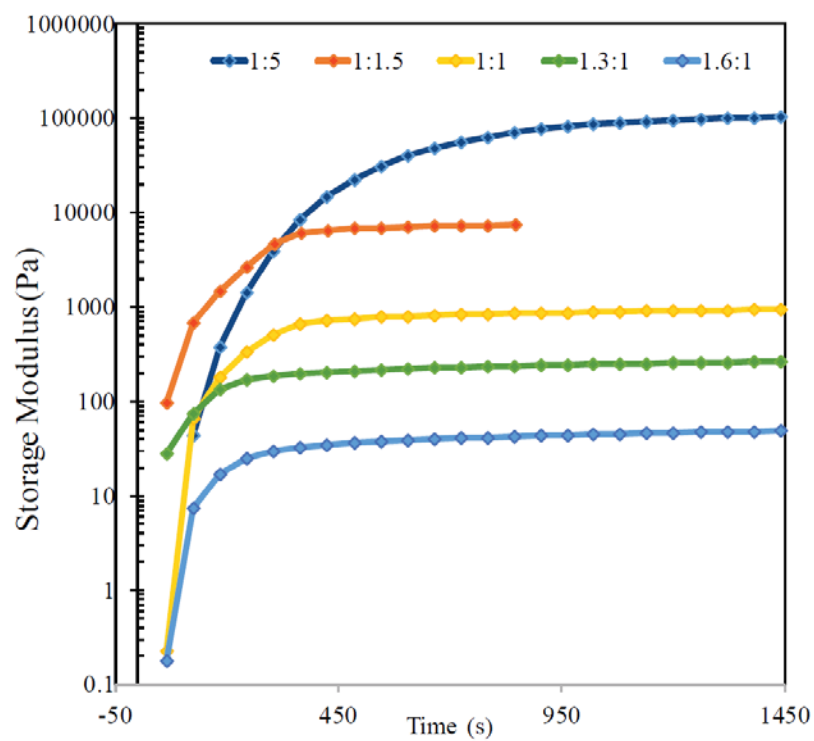
Figure 7.2. Shear rheology curing test curves.

Curing test of different monomer to crosslinker ratios at 60°C, with constant shear deformation at frequency of 1Hz. Measurements were taken every 60 seconds.

Biological Characterization To investigate how cells respond on different stiffness substrates, we seeded MCF10A mammary epithelial cells (MECs) and observed cell spreading and cell-matrix adhesion morphology. As previously reported, cell spreading was positively correlated with substrate stiffness (Figure 7.3d). Similarly, cells on stiff substrates (100kPa) formed large, elongated adhesions, while cells on soft substrates (250Pa) formed smaller adhesions in the middle of the cell (paxillin and actin staining, Figure 7.3e). These findings confirm that cells behave similarly on silicone gels as on the polyacrylamide hydrogels typically used to vary the mechanical properties of cell substrates. Further, we observed no cytotoxicity as a result of culture on silicone gels.

High-Refractive Index Silicone Gels for TIRF

To validate the refractive index of the gels and their compatibility with SAIM's optical requirements, we tested whether it is possible to perform TIRF microscopy on our silicone gel system. Specifically, we compared epifluorescent illumination with TIRF illumination of MCF10A cells expressing paxillin-mCherry and noted that, consistent with the concept of TIRF, at high incidence angles of excitation, we obtain a relative decrease in background signal and an enhancement of membrane-adjacent signal. In particular, we could much better distinguish paxillin-containing focal adhesions (Figure 7.3f).

Technical Validation of SAIM on Silicone Gels

Once we established that silicone gels are amenable to TIRF microscopy, we tested their compatibility with scanning angle interference microscopy. In order to do this, we needed to make theoretical adjustments to the image analysis software used to calculate fluorophore heights from acquired images. As described above, each image acquisition consists of a stack of images, each obtained at a different angle of incidence. Based on the optical theory behind SAIM, the fluorescence intensity of molecules should vary with the incident angle, in a manner that corresponds with the fluorophore's position above the reflective silicon surface.

A:B Ratio	1.6:1	1.3:1	1:1	1:1.5	1:5
Complex Mod. (Pa)	252	731	1478	8421	114727
St. deviation	46	65	49	796	4303
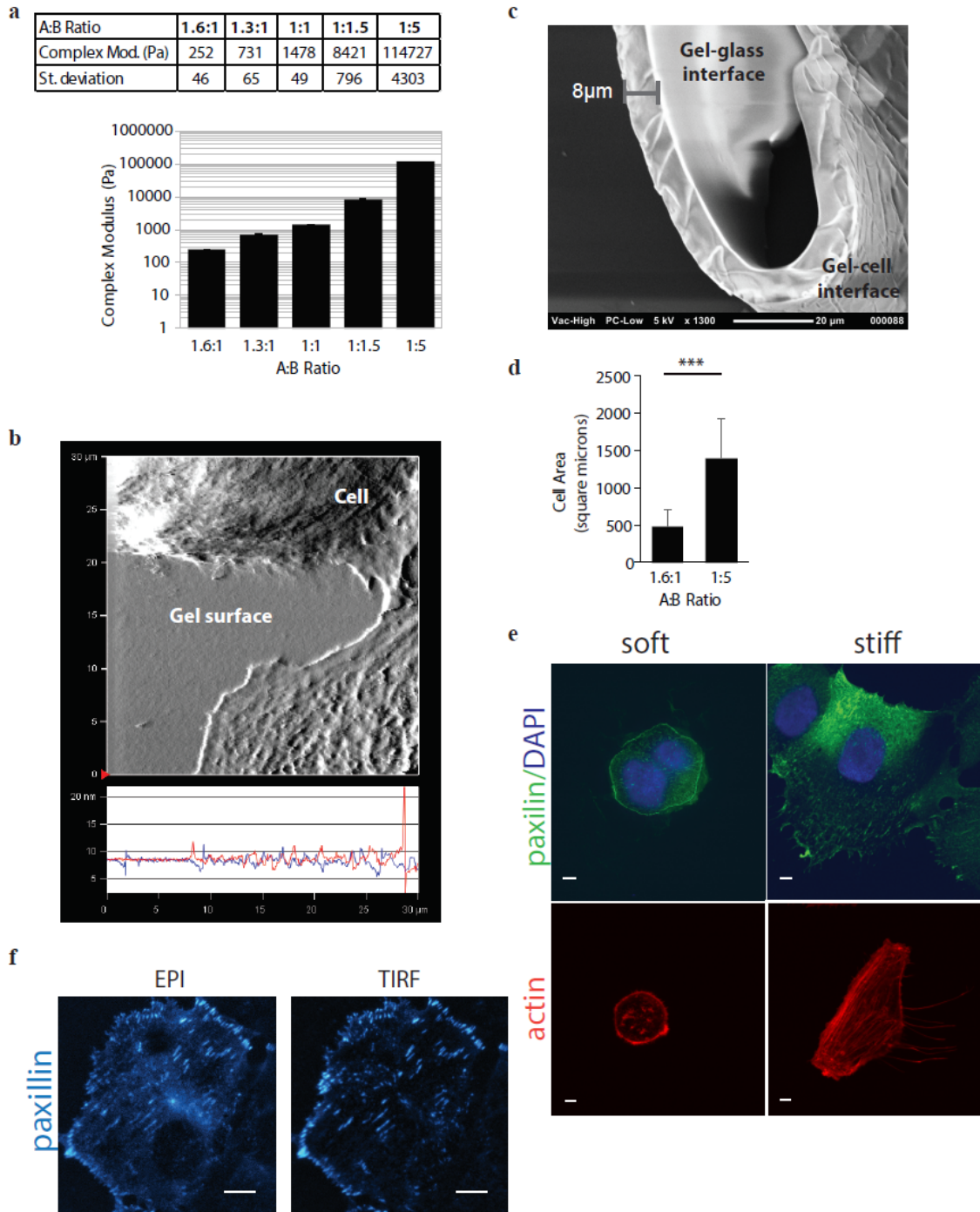
Figure 7.3. Silicone gel characterization.

a) Shear rheology of different gel base (A) to crosslinker (B) ratios and corresponding complex modulus. b) Atomic force microscopy image of epithelial cell seeded on matrix-protein functionalized silicone gel. c) Scanning electron microscopy of detached gel that allows characterization of gel surface roughness and thickness. d) Biological characterization of cellular response on gels with A:B ratios as indicated. Cells are more spread, as expected, on stiffer gels. Asterisks indicates p< 0.005. e) Confocal fluorescence microscopy of paxillin-GFP expressing MCF10A cells immunostained with DAPI and AlexaFluor594-Phalloidin on soft (252Pa) and stiff (114kPa) gels. Scale bar = 4.5µm. f) Paxillin-mCherry MCF10A cells seeded on stiff gels imaged under epifluorescence (left) and TIRF (right). Scale bar = 4.5µm.

113

Optical Theory An in-depth derivation of the generalized case of this phenomenon is described by Lambacher and Fromherz in their 1996 *Applied Physics A* article.[322] Here, we describe the specific case when incident light is polarized perpendicular to the plane of incidence, as in our application of SAIM. The fluorescence intensity of a fluorophore situated at position H above a silicon surface is governed by the strength of the electric field at H. To determine the strength of this electric field, we employ the transfer matrix method, an approach to account for electromagnetic waves of a given frequency propagating through a stack of layers of different materials.[328] It is based on the idea that, according to Maxwell's equations, there exist continuity conditions for an electric field as it crosses boundaries from one medium to another. Essentially, this means that if the field is known at the beginning of a layer, it is possible to calculate the field at the end of the layer through a matrix operation. Each layer has its corresponding transfer matrix, which can be multiplied together to produce the system matrix.

Each layer's transfer matrix is calculated using Fresnel coefficients. The standard form for a transfer matrix is as follows:

$$\begin{pmatrix} \cos(kL) & \frac{1}{k}\sin(kL) \\ -k\sin(kL) & \cos(kL) \end{pmatrix}$$

where k is the wave number in the material, and L is distance traversed through the material. Hence, for the silicon + silicon oxide case, the characteristic transfer matrix is

$$M_{TE} = \begin{pmatrix} m_{11}^{TE} & m_{12}^{TE} \\ m_{21}^{TE} & m_{22}^{TE} \end{pmatrix}$$

$$= \begin{pmatrix} \cos(k_{ox}d_{ox}\cos\theta_{ox}) & -\frac{i}{p_{ox}}\sin(k_{ox}d_{ox}\cos\theta_{ox}) \\ -ip_{ox}\sin(k_{ox}d_{ox}\cos\theta_{ox}) & \cos(k_{ox}d_{ox}\cos\theta_{ox}) \end{pmatrix}$$

where $p_{ox} = n_{ox} cos\theta_{ox}$, $k_{ox} = \frac{2\pi n_{ox}}{\lambda}$, for light wave with wavelength λ. $d_{ox} cos\theta_{ox}$ stands in for

L, by taking into account the true thickness of the layer, d_{ox}, as well as the angle at which the light

travels through the layer, θ_{ox}.

When we add in the silicone gel layer, we must include its corresponding transfer matrix:

$$= \begin{pmatrix} \cos(k_{gel}d_{gel}cos\theta_{gel}) & -\frac{i}{p_{gel}}\sin(k_{gel}d_{gel}cos\theta_{gel}) \\ -ip_{gel}\sin(k_{gel}d_{gel}cos\theta_{gel}) & \cos(k_{gel}d_{gel}cos\theta_{gel}) \end{pmatrix}$$

with $p_{gel} = n_{gel}\cos(\theta_{gel})$ and $k_{gel} = \frac{2\pi n_{gel}}{\lambda}$.

If we substitute $l_{gel} = k_{gel}d_{gel}\cos(\theta_{gel})$ and $l_{ox} = k_{ox}d_{ox}cos\theta_{ox}$ and multiply the silicon oxide

transfer matrix by the silicone gel matrix, we obtain the system matrix with the following

components:

$$m_{11}^{TE} = \cos(l_{gel})\cos(l_{ox}) - \frac{p_{ox}}{p_{gel}}\sin(l_{gel})\sin(l_{ox})$$

$$m_{12}^{TE} = -\frac{i}{p_{ox}}\cos(l_{gel})\sin(l_{ox}) - \frac{i}{p_{gel}}\sin(l_{gel})\cos(l_{ox})$$

$$m_{21}^{TE} = -ip_{gel}\sin(l_{gel})\cos(l_{ox}) - ip_{ox}\cos(l_{gel})\sin(l_{ox})$$

$$m_{22}^{TE} = -\frac{p_{gel}}{p_{ox}}\sin(l_{gel})\sin(l_1) + \cos(l_{gel})\cos(l_{ox})$$

This can then be used to construct the transverse electric component (perpendicular to the plane of

incidence) of the Fresnel coefficient of reflection between the imaging substrate and the sample:

$$r^{TE} = \frac{(m_{11}^{TE} + m_{12}^{TE}p_0)p_2 + (m_{21}^{TE} - m_{22}^{TE}p_0)}{(m_{11}^{TE} + m_{12}^{TE}p_0)p_2 + (m_{21}^{TE} + m_{22}^{TE}p_0)}$$

where $p_0 = n_{Si}cos\theta_{Si}, p_2 = n_s cos\theta_s$, corresponding to the silicon and sample layers, respectively.

This, in turn, allows us to know what happens to the electric field strength as it passes through each

material in our experimental system. Generally, it can be calculated as follows:

$$F \approx 1 + r^{TE} e^{i\phi(H)}$$

where ϕ is the phase difference between the direct and reflected light at position H:

$$\phi(H) = \frac{4\pi}{\lambda}(n_s H cos\theta_s)$$

for a light wave with wavelength λ at angle θ_s through a sample with refractive index n_s.

The analysis software uses constrained nonlinear least-squares optimization to fit experimental fluorescence intensity profiles to theoretically predicted profiles on a pixel by pixel basis. Fluorescence emission is proportional to the excitation radiation intensity, which is proportional to the squared projection of the local electric field onto the normal plane:

$$I = A\left|1 + r^{TE} e^{i\phi(H)}\right|^2 + B$$

where A adjusts for variation in intensity due to contributions from mean excitation laser intensity, fluorophore properties, and the efficiency of emitted photon detection and B accounts for background signal in the sample. The fitting algorithm fits for the parameters *A, B,* and *H.*

Fluorescent Microsphere Validation To test whether this new optical model can correctly calculate the position of a fluorophore above the silicon, silicon oxide, and silicone gel substrate, we conjugated fluorescent microspheres of known size onto the gel surface. Multiple quality control processes were employed both before and after quantitative image analysis. To account for variations in spin coated gel thickness, experimental fluorescence intensity curves were compared with a range of computationally generated curves to find the approximate range of gel thickness. Figure 7.4a illustrates how experimentally obtained pixel intensity can be plotted against excitation angle. The resulting curve can be used to evaluate instrument calibration. If TIRF angle calibration has been performed correctly, the curve should be mirrored around zero degrees and exhibit a periodic pattern as incidence angle changes. This experimental profile can be compared to the regular patterns of oscillation predicted by the optical model (Figure 7.4b). This process is performed with each set of experiments. A second quality control step is specifically implemented for microspheres. Due to the possibility of microsphere aggregates, masks are generated in FIJI

using z-projection with standard deviation. This allows isolation and exclusion of brighter than average bead clusters. Only values below 75% of maximum brightness are kept for mask generation. Finally, after image analysis, all pixels with an A-value less than 1.5 times the average A value for the experimental set are excluded. This necessarily leads to low yield but decreases neighboring pixel variability and whole cell variability. Figure 7.4c compares summarized height distributions from 6 microsphere samples imaged on either a 1900nm thick silicon oxide surface (left) or a spin-coated silicone gel surface (right). While there is less variation in the silicon oxide case, imaging on silicone gel substrates still produced reproducibly accurate height calculations, with an average near 50nm. This validates our ability to perform SAIM on silicone gels and to accurately measure the height of objects of known size above the imaging surface.
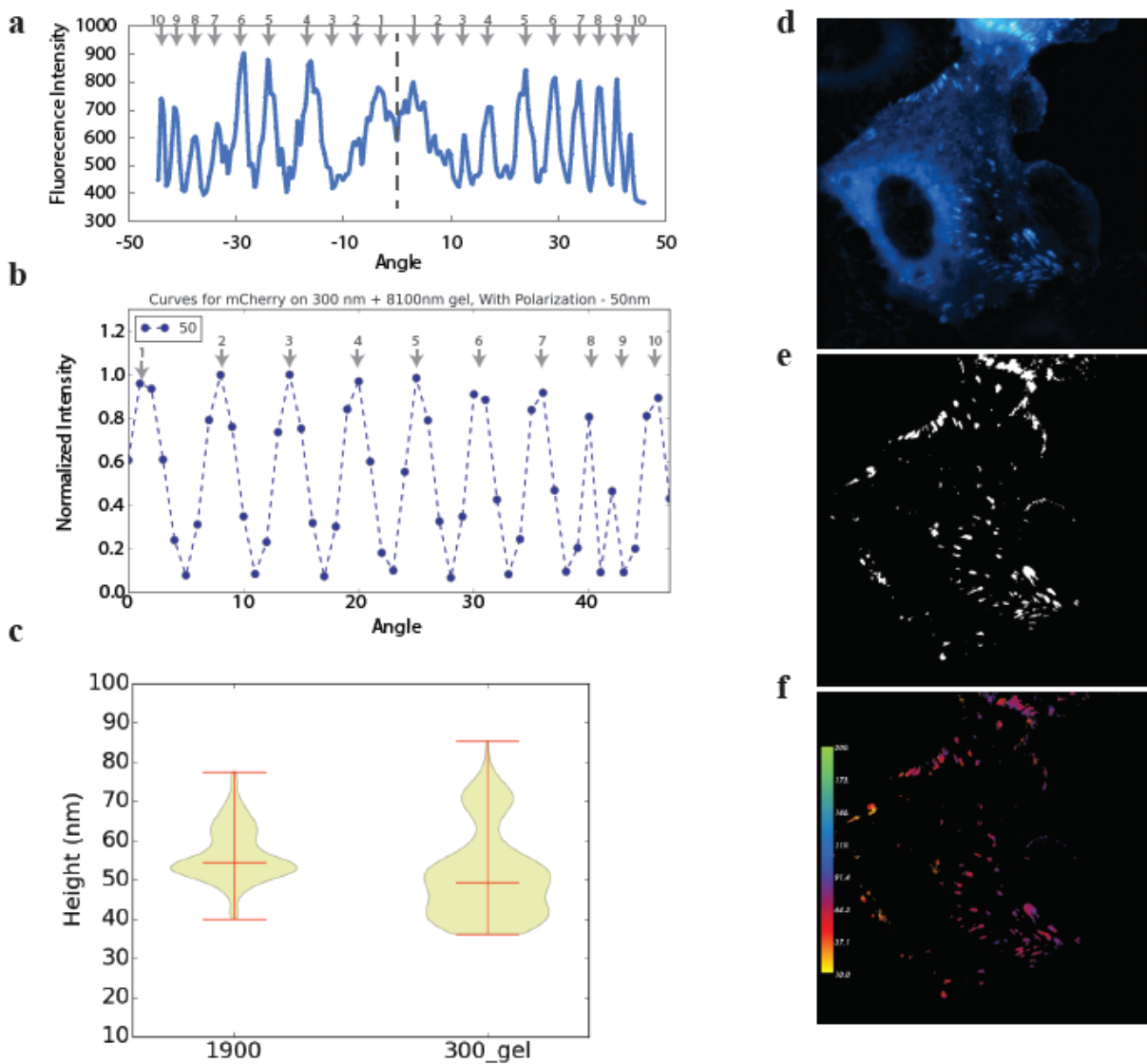
Figure 7.4. Technical and biological validation of SAIM on silicone gels.

a) An example of an experimentally obtained fluorescence intensity profile. Dotted line indicates incidence angle = 0°. Note that the profile is mirrored around this angle. Arrows indicate each inflection point and allows comparison with b) computationally generated curves. c) Comparison of fluorescence microsphere height on substrates without silicone gel (left) and with gel (right). d-f) Example of image processing process, with raw image (d), mask (e), and height map (f) of a vinculin-eGFP expressing MCF10A cell.

Biological Validation of SAIM on Silicone Gels To evaluate and demonstrate compatibility of this method to use in biological study, we used this silicone-gel SAIM to image focal adhesion and cytoskeletal protein positioning within MECs. Figure **7**.4d-f provides examples of representative images in the analysis process: the raw z-projected fluorescence image (7.4d), a masked image with areas of interest (adhesion) shown in white (**7**.4e), and a color map of adhesion heights produced after image analysis and fitting (**7**.4f). One indicator of high quality SAIM imaging and proper fitting is low variation in height in a local area, such as within an adhesion. The analysis software calculates height for each pixel independently. Hence, there is no memory or expectation of local agreement in height written into the program. As such, if we find that our results suggest an adhesion, made up of many pixels, is at approximately the same height above the substrate, this suggest that the method has been implemented correctly. Essentially, we use our biological intuition to evaluate technical execution of the method. For this first test, we imaged GFP-tagged vinculin and found it to be positioned approximately 60-90 nm above the cell substrate. This compares favourably with previously published studies, wherein vinculin z-position was imaged with PALM[329] and SAIM[321]. These studies reported finding vinculin between 45-60nm using PALM and 80-100nm using SAIM.

To demonstrate the potential for this novel platform to provide biological insight, we compared positions of two focal adhesion proteins in cells cultured on stiff and soft substrates. To facilitate direct comparison and to illustrate how this method could be used to study the relative positions of proteins within focal adhesions, we imaged both vinculin and paxillin in the same cells. We find that vinculin position does not change significantly. Its range on soft substrates is tightly distributed around 100nm, with 95% of observations falling between 60nm and135nm (Figure **7**.5a, individual example, and **7**.5c, aggregated data). Vinculin height in cells on stiff substrates centered around 86nm and 95% of observations fell between 68nm and 112nm (Figure **7**.5b, individual example, and **7**.5d, aggregated data). In contrast, while paxillin position averages 66nm on stiff substrates, (Figure **7**.5b and **7**.5d), its heights exhibit a clear, bimodal distribution on soft substrates (Figure **7**.5a and **7**.5c). This shift could be the result of changing binding
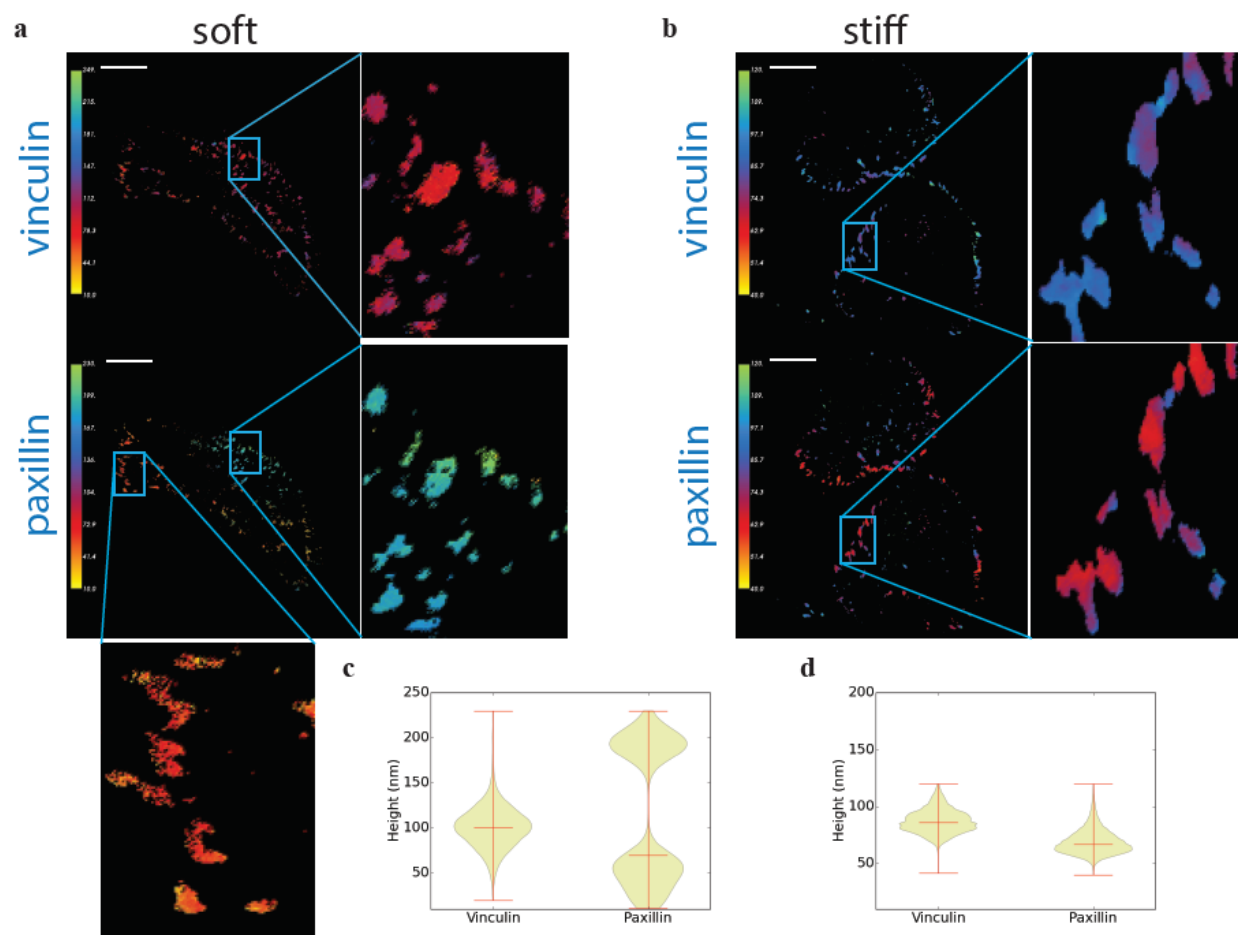
Figure 7.5. Further biological validation of SAIM on silicone gels.

a) Height maps of paxillin and vinculin in the same MCF10A cell on soft gel substrate, with insets. b) Height maps of paxillin and vinculin in the same MCF10A cell on stiff, silicon oxide substrate, with insets. c) Violin plot of adhesion protein heights for cells on soft substrates. d) Violin plot of adhesion protein heights for cells on stiff, silicon oxide substrates. Scale bar = 3μm.

partners for paxillin or a larger reorganization of the adhesion. Elucidating the precise mechanisms underlying this shift will certainly require further manipulation and study, but this intriguing example points to the types of phenomena this method could help to unveil and investigate.

To further explore ways in which this method may be used for biological investigation, we performed time-lapse SAIM imaging on MCF10A cells expressing paxillin-GFP (Figure **7**.6a). With 100ms exposure time, a full set of 182 frames required less than 50s for acquisition. This short acquisition time permits capturing dynamic cell processes, such as adhesion disassociation and maturation, which happen on a length scale of minutes. For instance, focal adhesion disassembly occurs over the course of 10-20 minutes.[55] In this example, we can see one population of paxillin disappear as a part of the membrane retracts and new adhesions form (Figure **7**.6b and **7**.6c).

Benchmarking Implementation of SAIM on mechanically tunable gels affords the ability to achieve 30-40nm precision in determining protein localization in z. This compares favourably to conventional confocal laser scanning microscopy, which has z-resolution in the range of 500-700nm.[330] Currently commercially available microscopy setups include stimulated emission depletion (STED), structured illumination microscopy (SIM), and PALM/STORM, as previously described.[330] These methods achieve anywhere from 50nm z-resolution in 3D-STORM[331] to 100nm in STED[332] and 250nm in SIM[330],. Of these methods, methods that allow penetrance into thick samples, like confocal or structured illumination microscopy, sacrifice vertical resolution. In contrast, methods that afford higher vertical resolution, like PALM/STORM, sacrifice compatibility with physiologically relevant samples. Uniquely, implementation of SAIM on mechanically tunable gels offers the ability to perform experiments on physiologically relevant samples while maintaining state of the art vertical resolution.
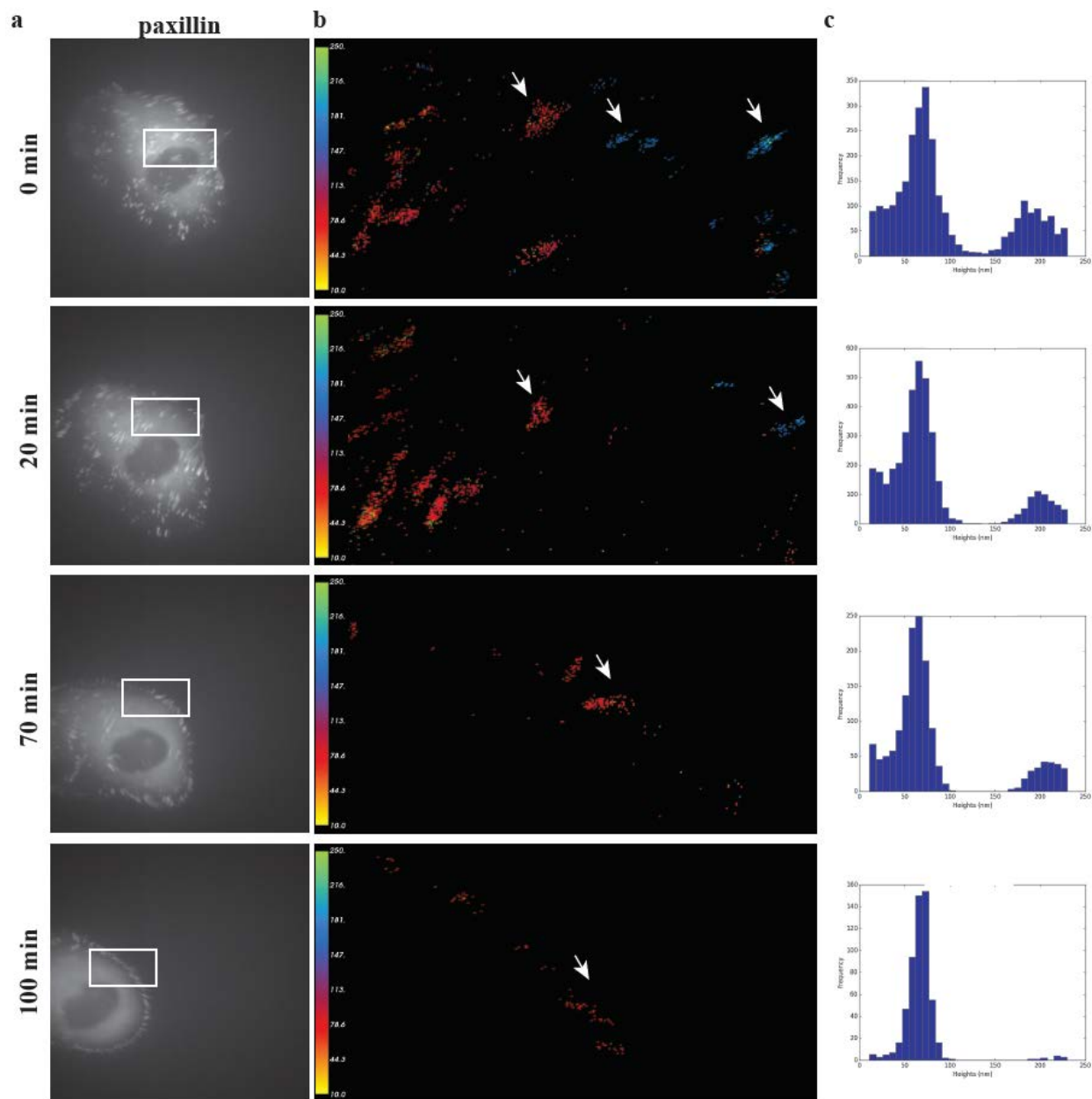
Figure 7.6. Time-lapse imaging with SAIM.

a) Z-projected images from time-lapse SAIM imaging of a migrating paxillin-eGFP expressing MCF10A cell on a 1.5kPa silicone gel substrate at 0, 20, 70, and 100minutes, with b) height maps for the areas boxed in white and c) histograms of height distributions in these cells.

SUMMARY

There remain many unanswered questions regarding how the mechanical properties of the extracellular matrix influence and regulate cellular processes. Use of novel nanoscale imaging techniques has already allowed researchers to elaborate many intricate signalling phenomena. This new method will facilitate application of one such tool to mechanobiological investigation. In addition to studying the nanoscale organization of focal adhesion proteins and the cytoskeleton, this method could be applied to study membrane curvature and topology under different substrate contexts, the interaction of membrane lipids and proteins, and more. The application of SAIM on mechanically tunable substrates combines physiologically relevant substrates with state of the art superresolution imaging, while affording the ability to perform live cell tracking. We present a method that can be implemented on commercially available microscopy equipment, with open-source analysis software, and with little investment in special materials. We look forward to its adoption and implementation to broaden our understanding of the effect of ECM rigidity on a wide array of cellular processes.

8 CONCLUSIONS AND FUTURE DIRECTIONS

My work provides specific examples of how changing extracellular matrix properties changes signaling context to affect cell signaling and fate. My investigation into matrix dimensionality revealed that this property can alter cytoskeletal tension and membrane dynamics to regulate GTPase activity, and, as a result, cell survival. Preliminary work into the effect of ECM stiffness on cell signaling indicates that altering substrate stiffness can change both the rate of protein endocytosis and its binding partners through this process. Both of these mechanisms are means by which the manner in which a cell processes signaling molecules changes in response to extracellular cues. This represents a departure from conventional mechanotransduction signaling, whereby ECM cues are processed by specific pathways (like integrin signaling) that then crosstalk with proliferation or survival signaling pathways. In addition to these biological studies, my efforts in tool development for both superresolution imaging and quantitative image analysis have enhanced researchers' abilities to study the effect of ECM properties on cell signaling and subcellular protein localization.

These are, of course, by now means the end of the story. Results from my work on matrix dimensionality point to further questions about how changes in membrane dynamics affect subcellular localization of other signaling factors. In addition, both Arf6 and Rac1 influence cell migration and trafficking. Understanding how matrix dimensionality affects these processes would be a logical continuation of my preliminary work. Further, while we now have a glimpse into how changing cytoskeletal tension can influence protein recruitment to the membrane and cell signaling, this idea needs to be explored in other signaling networks and in more cell types and tissue contexts. Similarly, demonstrating that extracellular stiffness can change the rate of receptor endocytosis, degradation, and recycling opens the door for many questions about what other proteins may be affected. Studies showing that altered trafficking is a conserved effect of increasing ECM stiffness would suggest that stiffness globally regulates protein processing within the cell. Conversely, future studies may find that this phenomenon to be specific to a subset of proteins—perhaps those that associate with integrins or caveolin. In addition to broadening our understanding of the effect of ECM

stiffness on protein trafficking across proteins and cell types, there is also much work remaining in terms of elucidating the molecular processes underlying this effect. One possibility raised by preliminary data is differential segregation of receptors on the cell surface. Increased ECM stiffness may induce integrin clustering and prevent EGFR-integrin binding, thereby freeing the receptor for more rapid internalization. Biochemically, the Rab effectors are main candidates of interest, as they have a clearly defined role in regulating integrin trafficking.

Broadly, what is powerful about these new insights into the interplay between ECM properties and cell signaling is the clear indication that signaling context has changed. This likely means that many pathways besides the ones we investigated are affected. As such, understanding the overall effect of changing ECM dimensionality or stiffness on cell signaling requires a holistic approach, such as high-throughput screening. There has been intriguing work already demonstrating the power of SILAC (stable isotope labeling by amino acids in cell culture) to illuminate how different parts of a signaling network (in this case TGF-β) is affected by external perturbation[333]. I would propose application of this approach to characterizing how changing ECM properties alters subcellular compartmentalization of activated components in the ErbB1/EGFR signaling network, as pictured in Figure 8.1.
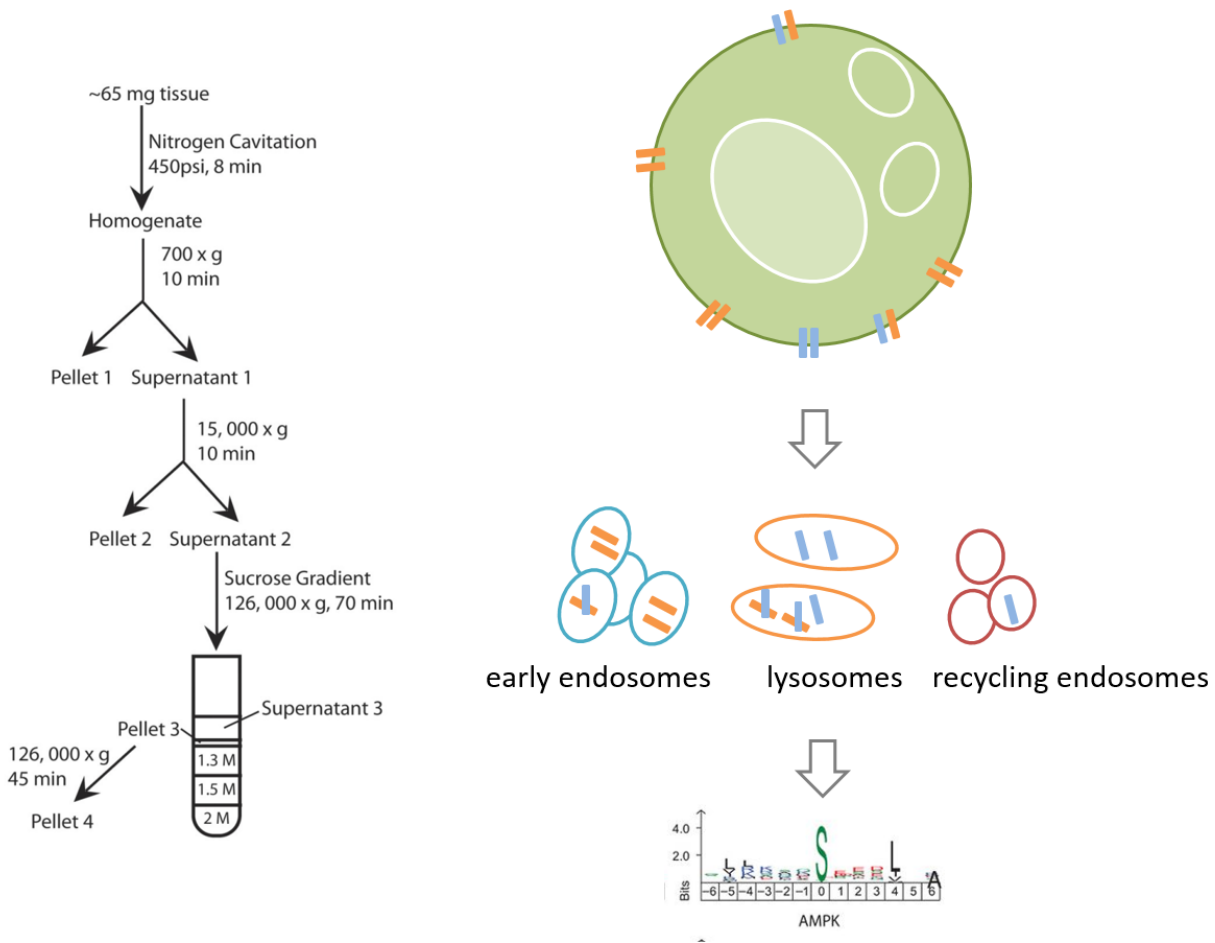
Figure 8.1. Suggested experimental flow for SILAC screening.

Subcellular compartments can be collected via centrifugation. These samples can then be sent for SILAC screening. Collectively, the data can reveal how trafficking and segregation of proteins is altered by matrix properties.

In addition, the development of a mechanically tunable substrate compatible with TIRF and SAIM allows us to better answer the question of how substrate stiffness regulates adhesion organization and receptor endocytosis. This gel system, combined with micropatterning technology, affords the ability to independently control cell shape, spreading, and substrate stiffness and thus better dissect the contribution of each of these factors to changes observed due to culture on different stiffness substrates.

I consider my thesis work to have been small steps in our growing understanding of the mechanistic underpinnings of mechanically regulated cell and tissue behavior. These results have lent intriguing insight into how a cell senses and synthesizes soluble and biophysical cues from its surroundings and I look forward to future work further elucidating this process.

WORKS CITED

1.   Mecham, R. P. Overview of extracellular matrix. *Curr. Protoc. Cell Biol.* **Chapter 10,** Unit 10.1 (2012).

2.   Lu, P., Takai, K., Weaver, V. M. & Werb, Z. Extracellular matrix degradation and remodeling in development and disease. *Cold Spring Harb. Perspect. Biol.* **3,** (2011).

3.   Rozario, T. & DeSimone, D. W. The extracellular matrix in development and morphogenesis: a dynamic view. *Dev. Biol.* **341,** 126–40 (2010).

4.   Naba, A. *et al.* The matrisome: in silico definition and in vivo characterization by proteomics of normal and tumor extracellular matrices. *Mol. Cell. Proteomics* **11,** M111.014647 (2012).

5.   Myllyharju, J. & Kivirikko, K. I. Collagens, modifying enzymes and their mutations in humans, flies and worms. *Trends Genet.* **20,** 33–43 (2004).

6.   Ricard-Blum, S. & Ruggiero, F. The collagen superfamily: from the extracellular matrix to the cell membrane. *Pathol. Biol. (Paris).* **53,** 430–42 (2005).

7.   Brodsky, B. & Persikov, A. V. Molecular structure of the collagen triple helix. *Adv. Protein Chem.* **70,** 301–39 (2005).

8.   Bandtlow, C. E. & Zimmermann, D. R. Proteoglycans in the developing brain: new conceptual insights for old proteins. *Physiol Rev* **80,** 1267–1290 (2000).

9.   Knudson, C. B. & Knudson, W. Cartilage proteoglycans. *Semin. Cell Dev. Biol.* **12,** 69–78 (2001).

10.   Cui, H., Freeman, C., Jacobson, G. A. & Small, D. H. Proteoglycans in the central nervous system: role in development, neural repair, and Alzheimer's disease. *IUBMB Life* **65,** 108–20 (2013).

11.   Schwartz, N. B. & Domowicz, M. Proteoglycans in brain development. *Glycoconj. J.* **21,** 329–41 (2004).

12.   *Glycosaminoglycans in Development, Health and Disease (Google eBook).* (Academic Press, 2010).

13.   Deepa, S. S. *et al.* Composition of perineuronal net extracellular matrix in rat brain: a different

disaccharide composition for the net-associated proteoglycans. *J. Biol. Chem.* **281,** 17789–800 (2006).

14.   Simon Davis, D. A. & Parish, C. R. Heparan sulfate: a ubiquitous glycosaminoglycan with multiple roles in immunity. *Front. Immunol.* **4,** 470 (2013).

15.   Bishop, J. R., Schuksz, M. & Esko, J. D. Heparan sulphate proteoglycans fine-tune mammalian physiology. *Nature* **446,** 1030–7 (2007).

16.   Proteoglycans and Sulfated Glycosaminoglycans. (2009).

17.   Wade, A., McKinney, A. & Phillips, J. J. Matrix regulators in neural stem cell functions. *Biochim. Biophys. Acta* (2014). doi:10.1016/j.bbagen.2014.01.017

18.   Johnson, K. G. *et al.* Axonal heparan sulfate proteoglycans regulate the distribution and efficiency of the repellent slit during midline axon guidance. *Curr. Biol.* **14,** 499–504 (2004).

19.   Häcker, U., Nybakken, K. & Perrimon, N. Heparan sulphate proteoglycans: the sweet side of development. *Nat. Rev. Mol. Cell Biol.* **6,** 530–541 (2005).

20.   Maeda, N., Ishii, M., Nishimura, K. & Kamimura, K. Functions of chondroitin sulfate and heparan sulfate in the developing brain. *Neurochem. Res.* **36,** 1228–40 (2011).

21.   Yamaguchi, Y. Lecticans: organizers of the brain extracellular matrix. *Cell. Mol. Life Sci.* **57,** 276–89 (2000).

22.   Lundell, A. *et al.* Structural basis for interactions between tenascins and lectican C-type lectin domains: evidence for a crosslinking role for tenascins. *Structure* **12,** 1495–506 (2004).

23.   Kalamajski, S. & Oldberg, A. The role of small leucine-rich proteoglycans in collagen fibrillogenesis. *Matrix Biol.* **29,** 248–53 (2010).

24.   Dellett, M., Hu, W., Papadaki, V. & Ohnuma, S. Small leucine rich proteoglycan family regulates multiple signalling pathways in neural development and maintenance. *Dev. Growth Differ.* **54,** 327–40 (2012).

25.   McEwan, P. A., Scott, P. G., Bishop, P. N. & Bella, J. Structural correlations in the family of small leucine-rich repeat proteins and proteoglycans. *J. Struct. Biol.* **155,** 294–305 (2006).

26.   Schaefer, L. & Iozzo, R. V. Biological functions of the small leucine-rich proteoglycans: from genetics to signal transduction. *J. Biol. Chem.* **283,** 21305–9 (2008).

27.   Chen, S. & Birk, D. E. The regulatory roles of small leucine-rich proteoglycans in extracellular matrix assembly. *FEBS J.* **280,** 2120–37 (2013).

28.   Oohira, A., Matsui, F., Tokita, Y., Yamauchi, S. & Aono, S. Molecular interactions of neural chondroitin sulfate proteoglycans in the brain development. *Arch. Biochem. Biophys.* **374,** 24–34 (2000).

29.   Timpl, R. & Brown, J. C. The laminins. *Matrix Biol.* **14,** 275–81 (1994).

30.   Aumailley, M. *et al.* A simplified laminin nomenclature. *Matrix Biol.* **24,** 326–32 (2005).

31.   Miner, J. H. & Yurchenco, P. D. Laminin functions in tissue morphogenesis. *Annu. Rev. Cell Dev. Biol.* **20,** 255–84 (2004).

32.   Mercurio, A. M. & Shaw, L. M. Laminin binding proteins. *Bioessays* **13,** 469–73 (1991).

33.   Yurchenco, P. D., Smirnov, S. & Mathus, T. Analysis of basement membrane self-assembly and cellular interactions with native and recombinant glycoproteins. *Methods Cell Biol.* **69,** 111–44 (2002).

34.   Schwarzbauer, J. E. & DeSimone, D. W. Fibronectins, their fibrillogenesis, and in vivo functions. *Cold Spring Harb. Perspect. Biol.* **3,** (2011).

35.   Singh, P., Carraher, C. & Schwarzbauer, J. E. Assembly of fibronectin extracellular matrix. *Annu. Rev. Cell Dev. Biol.* **26,** 397–419 (2010).

36.   Hynes, R. O. *Fibronectins*. (Springer New York, 1990). doi:10.1007/978-1-4612-3264-3

37.   García, A. J., Schwarzbauer, J. E. & Boettiger, D. Distinct Activation States of α5β1 Integrin Show Differential Binding to RGD and Synergy Domains of Fibronectin †. *Biochemistry* **41,** 9063–9069 (2002).

38.   Ilić, D. *et al.* FAK promotes organization of fibronectin matrix and fibrillar adhesions. *J. Cell Sci.* **117,** 177–87 (2004).

39.   Mouw, J. K., Ou, G. & Weaver, V. M. Extracellular matrix assembly: a multiscale deconstruction.

Nat. Rev. Mol. Cell Biol. **15,** 771–785 (2014).

40.   Yamada, K. M. & Cukierman, E. Modeling tissue morphogenesis and cancer in 3D. *Cell* **130,** 601–10 (2007).

41.   Cukierman, E., Pankov, R., Stevens, D. R. & Yamada, K. M. Taking cell-matrix adhesions to the third dimension. *Science* **294,** 1708–12 (2001).

42.   Sutherland, R. M. & Durand, R. E. Radiation response of multicell spheroids--an in vitro tumour model. *Curr. Top. Radiat. Res. Q.* **11,** 87–139 (1976).

43.   Zahir, N. & Weaver, V. M. Death in the third dimension: apoptosis regulation and tissue architecture. *Curr. Opin. Genet. Dev.* **14,** 71–80 (2004).

44.   Wang, F. *et al.* Reciprocal interactions between β1-integrin and epidermal growth factor receptor in three-dimensional basement membrane breast cultures: A different perspective in epithelial biology. *Proc. Natl. Acad. Sci.* **95,** 14821–14826 (1998).

45.   Bell, S. E. *et al.* Differential gene expression during capillary morphogenesis in 3D collagen matrices: regulated expression of genes involved in basement membrane matrix assembly, cell cycle progression, cellular differentiation and G-protein signaling. *J. Cell Sci.* **114,** 2755–73 (2001).

46.   Tsuboi, N. *et al.* Three-dimensional matrix suppresses E2F-controlled gene expression in glomerular mesangial cells. *Kidney Int.* **57,** 1581–9 (2000).

47.   Ghosh, S. *et al.* Three-dimensional culture of melanoma cells profoundly affects gene expression profile: A high density oligonucleotide array study. *J. Cell. Physiol.* **204,** 522–531 (2005).

48.   Lelièvre, S., Weaver, V. M. & Bissell, M. J. Extracellular Matrix Signaling from the Cellular Membrane Skeleton to the Nuclear Skeleton: A Model of Gene Regulation. *Recent Prog. Horm. Res.* **51,** 417–432 (1996).

49.   Weaver, V. M. *et al.* beta4 integrin-dependent formation of polarized three-dimensional architecture confers resistance to apoptosis in normal and malignant mammary epithelium. *Cancer Cell* **2,** 205–16 (2002).

50.   Bhalla, U. S. Signaling in small subcellular volumes. I. Stochastic and diffusion effects on individual

pathways. *Biophys. J.* **87,** 733–44 (2004).

51. Dehmelt, L. & Bastiaens, P. I. H. Spatial organization of intracellular communication: insights from imaging. *Nat. Rev. Mol. Cell Biol.* **11,** 440–52 (2010).

52. DeWire, S. M., Ahn, S., Lefkowitz, R. J. & Shenoy, S. K. Beta-arrestins and cell signaling. *Annu. Rev. Physiol.* **69,** 483–510 (2007).

53. Kolch, W. Coordinating ERK/MAPK signalling through scaffolds and inhibitors. *Nat. Rev. Mol. Cell Biol.* **6,** 827–37 (2005).

54. Kholodenko, B. N., Hancock, J. F. & Kolch, W. Signalling ballet in space and time. *Nat. Rev. Mol. Cell Biol.* **11,** 414–26 (2010).

55. Webb, D. J. *et al.* FAK-Src signalling through paxillin, ERK and MLCK regulates adhesion disassembly. *Nat. Cell Biol.* **6,** 154–61 (2004).

56. Calalb, M. B., Zhang, X., Polte, T. R. & Hanks, S. K. Focal adhesion kinase tyrosine-861 is a major site of phosphorylation by Src. *Biochem. Biophys. Res. Commun.* **228,** 662–8 (1996).

57. Ishibe, S., Joly, D., Liu, Z.-X. & Cantley, L. G. Paxillin serves as an ERK-regulated scaffold for coordinating FAK and Rac activation in epithelial morphogenesis. *Mol. Cell* **16,** 257–67 (2004).

58. Morén, A., Raja, E., Heldin, C.-H. & Moustakas, A. Negative regulation of TGFβ signaling by the kinase LKB1 and the scaffolding protein LIP1. *J. Biol. Chem.* **286,** 341–53 (2011).

59. Morrison, D. K. KSR: a MAPK scaffold of the Ras pathway? *J. Cell Sci.* **114,** 1609–12 (2001).

60. Kortum, R. L. & Lewis, R. E. The Molecular Scaffold KSR1 Regulates the Proliferative and Oncogenic Potential of Cells. *Mol. Cell. Biol.* **24,** 4407–4416 (2004).

61. Kubow, K. E., Conrad, S. K. & Horwitz, A. R. Matrix microarchitecture and myosin II determine adhesion in 3D matrices. *Curr. Biol.* **23,** 1607–19 (2013).

62. Petroll, W. M. *et al.* Mechanotransduction of mesenchymal melanoma cell invasion into 3D collagen lattices: Filopod-mediated extension–relaxation cycles and force anisotropy. *Exp. Cell Res.* **319,** 2424–2433 (2013).

63. Chung, I. *et al.* Spatial control of EGF receptor activation by reversible dimerization on living cells.

Nature **464,** 783–787 (2010).

64.   Pickl, M. & Ries, C. H. Comparison of 3D and 2D tumor models reveals enhanced HER2 activation in 3D associated with an increased response to trastuzumab. *Oncogene* **28,** 461–8 (2009).

65.   Weigelt, B., Lo, A. T., Park, C. C., Gray, J. W. & Bissell, M. J. HER2 signaling pathway activation and response of breast cancer cells to HER2-targeting agents is dependent strongly on the 3D microenvironment. *Breast Cancer Res. Treat.* **122,** 35–43 (2010).

66.   Youle, R. J. & Strasser, A. The BCL-2 protein family: opposing activities that mediate cell death. *Nat. Rev. Mol. Cell Biol.* **9,** 47–59 (2008).

67.   Lovell, J. F. *et al.* Membrane binding by tBid initiates an ordered series of events culminating in membrane permeabilization by Bax. *Cell* **135,** 1074–84 (2008).

68.   de Jonge, N. & Ross, F. M. Electron microscopy of specimens in liquid. *Nat. Nanotechnol.* **6,** 695–704 (2011).

69.   Vic, P., Vignon, F., Derocq, D. & Rochefort, H. Effect of Estradiol on the Ultrastructure of the MCF7 Human Breast Cancer Cells in Culture. *Cancer Res.* **42,** 667–673 (1982).

70.   Loessner, D. *et al.* Bioengineered 3D platform to explore cell-ECM interactions and drug resistance of epithelial ovarian cancer cells. *Biomaterials* **31,** 8494–506 (2010).

71.   Stenoien, D. L. *et al.* FRAP reveals that mobility of oestrogen receptor-alpha is ligand- and proteasome-dependent. *Nat. Cell Biol.* **3,** 15–23 (2001).

72.   Chan, S. W. *et al.* TEADs mediate nuclear retention of TAZ to promote oncogenic transformation. *J. Biol. Chem.* **284,** 14347–58 (2009).

73.   Gaborit, N. *et al.* Time-resolved fluorescence resonance energy transfer (TR-FRET) to analyze the disruption of EGFR/HER2 dimers: a new method to evaluate the efficiency of targeted therapy using monoclonal antibodies. *J. Biol. Chem.* **286,** 11337–45 (2011).

74.   Vilardaga, J.-P., Bünemann, M., Krasel, C., Castro, M. & Lohse, M. J. Measurement of the millisecond activation switch of G protein-coupled receptors in living cells. *Nat. Biotechnol.* **21,** 807–12 (2003).

75. Grashoff, C. *et al.* Measuring mechanical tension across vinculin reveals regulation of focal adhesion dynamics. *Nature* **466,** 263–266 (2010).

76. Berezin, M. Y. & Achilefu, S. Fluorescence lifetime measurements and biological imaging. *Chem. Rev.* **110,** 2641–84 (2010).

77. Vogel, V. & Sheetz, M. Local force and geometry sensing regulate cell functions. *Nat. Rev. Mol. Cell Biol.* **7,** 265–275 (2006).

78. Chen, C. S. Geometric Control of Cell Life and Death. *Science (80-.).* **276,** 1425–1428 (1997).

79. Zamir, E. *et al.* Molecular diversity of cell-matrix adhesions. *J. Cell Sci.* **112,** 1655–1669 (1999).

80. Aplin, A. E. Cell adhesion molecule regulation of nucleocytoplasmic trafficking. *FEBS Lett.* **534,** 11–14 (2003).

81. Juliano, R. L. SIGNAL TRANSDUCTION BY CELL ADHESION RECEPTORS AND THE CYTOSKELETON: Functions of Integrins, Cadherins, Selectins, and Immunoglobulin-Superfamily Members. *Annu. Rev. Pharmacol. Toxicol.* **42,** 283–323 (2002).

82. Ochsner, M., Textor, M., Vogel, V. & Smith, M. L. Dimensionality controls cytoskeleton assembly and metabolism of fibroblast cells in response to rigidity and shape. *PLoS One* **5,** e9445 (2010).

83. Ghibaudo, M., Di Meglio, J.-M., Hersen, P. & Ladoux, B. Mechanics of cell spreading within 3D-micropatterned environments. *Lab Chip* **11,** 805–12 (2011).

84. McBeath, R., Pirone, D. M., Nelson, C. M., Bhadriraju, K. & Chen, C. S. Cell shape, cytoskeletal tension, and RhoA regulate stem cell lineage commitment. *Dev. Cell* **6,** 483–95 (2004).

85. Engler, A. J., Sen, S., Sweeney, H. L. & Discher, D. E. Matrix Elasticity Directs Stem Cell Lineage Specification. *Cell* **126,** 677–689 (2006).

86. Raucher, D. & Sheetz, M. P. Cell Spreading and Lamellipodial Extension Rate Is Regulated by Membrane Tension. *J. Cell Biol.* **148,** 127–136 (2000).

87. Sheetz, M. P. & Dai, J. Modulation of membrane dynamics and cell motility by membrane tension. *Trends Cell Biol.* **6,** 85–89 (1996).

88. Dai, J. & Sheetz, M. P. Regulation of Endocytosis, Exocytosis, and Shape by Membrane Tension.

Cold Spring Harb. Symp. Quant. Biol. **60,** 567–571 (1995).

89.   Tarricone, C. *et al.* The structural basis of Arfaptin-mediated cross-talk between Rac and Arf signalling pathways. *Nature* **411,** 215–9 (2001).

90.   Williger, B.-T., Ostermann, J. & Exton, J. H. Arfaptin 1, an ARF-binding protein, inhibits phospholipase D and endoplasmic reticulum/Golgi protein transport. *FEBS Lett.* **443,** 197–200 (1999).

91.   Van Aelst, L., Joneson, T. & Bar-Sagi, D. Identification of a novel Rac1-interacting protein involved in membrane ruffling. *EMBO J.* **15,** 3778–86 (1996).

92.   Kubo, T. *et al.* A Novel FERM Domain Including Guanine Nucleotide Exchange Factor Is Involved in Rac Signaling and Regulates Neurite Remodeling. *J. Neurosci.* **22,** 8504–8513 (2002).

93.   Stefanova, N. *et al.* Cell culturing in a three-dimensional matrix affects the localization and properties of plasma membrane cholesterol. *Cell Biol. Int.* **33,** 1079–86 (2009).

94.   Caswell, P. T., Vadrevu, S. & Norman, J. C. Integrins: masters and slaves of endocytic transport. *Nat. Rev. Mol. Cell Biol.* **10,** 843–53 (2009).

95.   Lingwood, D. & Simons, K. Lipid rafts as a membrane-organizing principle. *Science* **327,** 46–50 (2010).

96.   McAuliffe, P. F., Meric-Bernstam, F., Mills, G. B. & Gonzalez-Angulo, A. M. Deciphering the role of PI3K/Akt/mTOR pathway in breast cancer biology and pathogenesis. *Clin. Breast Cancer* **10 Suppl 3,** S59–65 (2010).

97.   Vara, J. Á. F. *et al.* PI3K/Akt signalling pathway and cancer. *Cancer Treat. Rev.* **30,** 193–204 (2004).

98.   Gao, X. *et al.* PI3K/Akt signaling requires spatial compartmentalization in plasma membrane microdomains. *Proc. Natl. Acad. Sci. U. S. A.* **108,** 14509–14 (2011).

99.   Balasubramanian, N., Scott, D. W., Castle, J. D., Casanova, J. E. & Schwartz, M. A. Arf6 and microtubules in adhesion-dependent trafficking of lipid rafts. *Nat. Cell Biol.* **9,** 1381–91 (2007).

100.   Mañes, S., Ana Lacalle, R., Gómez-Moutón, C. & Martínez-A, C. From rafts to crafts: membrane

asymmetry in moving cells. *Trends Immunol.* **24,** 319–325 (2003).

101. Matsuoka, T. *et al.* PI3K/Akt signalling is required for the attachment and spreading, and growth in vivo of metastatic scirrhous gastric carcinoma. *Br. J. Cancer* **106,** 1535–42 (2012).

102. Flusberg, D. A., Numaguchi, Y. & Ingber, D. E. Cooperative control of Akt phosphorylation, bcl-2 expression, and apoptosis by cytoskeletal microfilaments and microtubules in capillary endothelial cells. *Mol. Biol. Cell* **12,** 3087–94 (2001).

103. Oinuma, I., Kawada, K., Tsukagoshi, K. & Negishi, M. Rnd1 and Rnd3 targeting to lipid raft is required for p190 RhoGAP activation. *Mol. Biol. Cell* **23,** 1593–604 (2012).

104. Mammoto, A., Huang, S. & Ingber, D. E. Filamin links cell shape and cytoskeletal structure to Rho regulation by controlling accumulation of p190RhoGAP in lipid rafts. *J. Cell Sci.* **120,** 456–67 (2007).

105. Nikolov, D. B., Xu, K. & Himanen, J. P. Eph/ephrin recognition and the role of Eph/ephrin clusters in signaling initiation. *Biochim. Biophys. Acta - Proteins Proteomics* **1834,** 2160–2165 (2013).

106. Salaita, K. *et al.* Restriction of receptor movement alters cellular response: physical force sensing by EphA2. *Science* **327,** 1380–5 (2010).

107. Malek, A. M. & Izumo, S. Mechanism of endothelial cell shape change and cytoskeletal remodeling in response to fluid shear stress. *J. Cell Sci.* **109 (Pt 4,** 713–26 (1996).

108. Huveneers, S. *et al.* Vinculin associates with endothelial VE-cadherin junctions to control force-dependent remodeling. *J. Cell Biol.* **196,** 641–52 (2012).

109. Gee, E., Milkiewicz, M. & Haas, T. L. p38 MAPK activity is stimulated by vascular endothelial growth factor receptor 2 activation and is essential for shear stress-induced angiogenesis. *J. Cell. Physiol.* **222,** 120–6 (2010).

110. Jalali, S. *et al.* Shear stress activates p60src-Ras-MAPK signaling pathways in vascular endothelial cells. *Arterioscler. Thromb. Vasc. Biol.* **18,** 227–34 (1998).

111. McEver, R. P. & Zhu, C. Rolling cell adhesion. *Annu. Rev. Cell Dev. Biol.* **26,** 363–96 (2010).

112. Sorokin, L. The impact of the extracellular matrix on inflammation. *Nat. Rev. Immunol.* **10,** 712–23

(2010).

113. Srinivasan, S. *et al.* Rac and Cdc42 play distinct roles in regulating PI(3,4,5)P3 and polarity during neutrophil chemotaxis. *J. Cell Biol.* **160,** 375–85 (2003).

114. Chow, D., Nunalee, M. L., Lim, D. W., Simnick, A. J. & Chilkoti, A. Peptide-based Biopolymers in Biomedicine and Biotechnology. *Mater. Sci. Eng. R. Rep.* **62,** 125–155 (2008).

115. Stevenson, M. D. *et al.* A self-assembling peptide matrix used to control stiffness and binding site density supports the formation of microvascular networks in three dimensions. *Acta Biomater.* **9,** 7651–61 (2013).

116. Mi, K. *et al.* Influence of a self-assembling peptide, RADA16, compared with collagen I and Matrigel on the malignant phenotype of human breast-cancer cells in 3D cultures and in vivo. *Macromol. Biosci.* **9,** 437–43 (2009).

117. Miroshnikova, Y. A. *et al.* Engineering strategies to recapitulate epithelial morphogenesis within synthetic three-dimensional extracellular matrix with tunable mechanical properties. *Phys. Biol.* **8,** 026013 (2011).

118. Levental, K. R. *et al.* Matrix Crosslinking Forces Tumor Progression by Enhancing Integrin Signaling. *Cell* **139,** 891–906 (2009).

119. Willits, R. K. & Skornia, S. L. Effect of collagen gel stiffness on neurite extension. *J. Biomater. Sci. Polym. Ed.* **15,** 1521–31 (2004).

120. Ashe, H. L. & Briscoe, J. The interpretation of morphogen gradients. *Development* **133,** 385–394 (2006).

121. Lander, A. D., Nie, Q. & Wan, F. Y. . Do Morphogen Gradients Arise by Diffusion? *Dev. Cell* **2,** 785–796 (2002).

122. Bollenbach, T. *et al.* Precision of the Dpp gradient. *Development* **135,** 1137–1146 (2008).

123. Yu, S. R. *et al.* Fgf8 morphogen gradient forms by a source-sink mechanism with freely diffusing molecules. *Nature* **461,** 533–536 (2009).

124. Jaeger, J. *et al.* Dynamic control of positional information in the early Drosophila embryo. *Nature*

430, 368–371 (2004).

125. Houchmandzadeh, B., Wieschaus, E. & Leibler, S. Establishment of developmental precision and proportions in the early Drosophila embryo. *Nature* **415,** 798–802 (2002).

126. Dpp Gradient Formation in the Drosophila Wing Imaginal Disc. *Cell* **103,** 971–980 (2000).

127. Belenkaya, T. Y. *et al.* Drosophila Dpp morphogen movement is independent of dynamin-mediated endocytosis but regulated by the glypican members of heparan sulfate proteoglycans. *Cell* **119,** 231–44 (2004).

128. Rogers, K. W. & Schier, A. F. Morphogen gradients: from generation to interpretation. *Annu. Rev. Cell Dev. Biol.* **27,** 377–407 (2011).

129. Tucker, J. A., Mintzer, K. A. & Mullins, M. C. The BMP signaling gradient patterns dorsoventral tissues in a temporally progressive manner along the anteroposterior axis. *Dev. Cell* **14,** 108–119 (2008).

130. Hogan, B. L. Bone morphogenetic proteins: multifunctional regulators of vertebrate development. *Genes Dev.* **10,** 1580–1594 (1996).

131. Yu, S. R. *et al.* Fgf8 morphogen gradient forms by a source-sink mechanism with freely diffusing molecules. *Nature* **461,** 533–536 (2009).

132. Dessaud, E. *et al.* Interpretation of the sonic hedgehog morphogen gradient by a temporal adaptation mechanism. *Nature* **450,** 717–720 (2007).

133. Kretzschmar, K. & Watt, F. M. Lineage Tracing. *Cell* **148,** 33–45 (2012).

134. Swartz, M. A. & Fleury, M. E. Interstitial Flow and Its Effects in Soft Tissues. *Annu. Rev. Biomed. Eng.* **9,** 229–256 (2007).

135. Pouysségur, J., Volmat, V. & Lenormand, P. Fidelity and spatio-temporal control in MAP kinase (ERKs) signalling. *Biochem. Pharmacol.* **64,** 755–763 (2002).

136. Vaupel, P. & Mayer, A. Hypoxia in cancer: significance and impact on clinical outcome. *Cancer Metastasis Rev.* **26,** 225–239 (2007).

137. Harris, A. L. Hypoxia — a key regulatory factor in tumour growth. *Nat. Rev. Cancer* **2,** 38–47

(2002).

138. Warburton, D. *et al.* Molecular mechanisms of early lung specification and branching morphogenesis. *Pediatr. Res.* **57,** 26R–37R (2005).

139. Fleury, M. E., Boardman, K. C. & Swartz, M. A. Autologous Morphogen Gradients by Subtle Interstitial Flow and Matrix Interactions. *Biophys. J.* **91,** 113–121 (2006).

140. Fischbach, C. *et al.* Cancer cell angiogenic capability is regulated by 3D culture and integrin engagement. *Proc. Natl. Acad. Sci. U.S.A.* **106,** 399–404 (2009).

141. Liu, H., Radisky, D. C., Wang, F. & Bissell, M. J. Polarity and proliferation are controlled by distinct signaling pathways downstream of PI3-kinase in breast epithelial tumor cells. *J. Cell Biol.* **164,** 603–612 (2004).

142. Khademhosseini, A. *et al.* Co-culture of human embryonic stem cells with murine embryonic fibroblasts on microwell-patterned substrates. *Biomaterials* **27,** 5968–5977 (2006).

143. Ludwig, T. E. *et al.* Derivation of human embryonic stem cells in defined conditions. *Nat. Biotechnol.* **24,** 185–187 (2006).

144. Amit, M. & Itskovitz-Eldor, J. in (Irina Klimanskaya and Robert Lanza) **Volume 420,** 37–49 (Academic Press, 2006).

145. Xu, C. *et al.* Feeder-free growth of undifferentiated human embryonic stem cells. *Nat. Biotechnol.* **19,** 971–974 (2001).

146. Ludwig, T. E. *et al.* Feeder-independent culture of human embryonic stem cells. *Nat. Methods* **3,** 637–646 (2006).

147. Alvarez-Maubecin, V., García-Hernández, F., Williams, J. T. & Bockstaele, E. J. Van. Functional Coupling between Neurons and Glia. *J. Neurosci.* **20,** 4091–4098 (2000).

148. Huang, H., Kamm, R. D. & Lee, R. T. Cell mechanics and mechanotransduction: pathways, probes, and physiology. *Am. J. Physiol. - Cell Physiol.* **287,** C1–C11 (2004).

149. Halassa, M. M. & Haydon, P. G. Integrated Brain Circuits: Astrocytic Networks Modulate Neuronal Activity and Behavior. *Annu. Rev. Physiol.* **72,** 335–355 (2010).

150. Haydon, P. G. Neuroglial networks: Neurons and glia talk to each other. *Curr. Biol.* **10,** R712–R714 (2000).

151. Ullian, E. M., Christopherson, K. S. & Barres, B. A. Role for glia in synaptogenesis. *Glia* **47,** 209–216 (2004).

152. Zhang, M. Y. *et al.* Microfluidic environment for high density hepatocyte culture. *Biomed. Microdevices* **10,** 117–121 (2008).

153. Powers, M. J. *et al.* Functional Behavior of Primary Rat Liver Cells in a Three-Dimensional Perfused Microarray Bioreactor. *Tissue Eng.* **8,** 499–513 (2002).

154. Powers, M. J. *et al.* A microfabricated array bioreactor for perfused 3D liver culture. *Biotechnol. Bioeng.* **78,** 257–269 (2002).

155. Lee, P. J., Hung, P. J. & Lee, L. P. An artificial liver sinusoid with a microfluidic endothelial-like barrier for primary hepatocyte culture. *Biotechnol. Bioeng.* **97,** 1340–1346 (2007).

156. Tibbitt, M. W. & Anseth, K. S. Hydrogels as extracellular matrix mimics for 3D cell culture. *Biotechnol. Bioeng.* **103,** 655–63 (2009).

157. Whitesides, G. M., Ostuni, E., Takayama, S., Jiang, X. & Ingber, D. E. Soft lithography in biology and biochemistry. *Annu. Rev. Biomed. Eng.* **3,** 335–73 (2001).

158. Kane, R. S., Takayama, S., Ostuni, E., Ingber, D. E. & Whitesides, G. M. Patterning proteins and cells using soft lithography. *Biomaterials* **20,** 2363–2376 (1999).

159. Sung, J. H., Kam, C. & Shuler, M. L. A microfluidic device for a pharmacokinetic–pharmacodynamic (PK–PD) model on a chip. *Lab Chip* **10,** 446–455 (2010).

160. Miller, J. S. *et al.* Rapid casting of patterned vascular networks for perfusable engineered three-dimensional tissues. *Nat. Mater.* **11,** 768–774 (2012).

161. Huh, D. *et al.* Reconstituting Organ-Level Lung Functions on a Chip. *Science (80-.).* **328,** 1662–1668 (2010).

162. Nakao, Y., Kimura, H., Sakai, Y. & Fujii, T. Bile canaliculi formation by aligning rat primary hepatocytes in a microfluidic device. *Biomicrofluidics* **5,** 022212 (2011).

163. Allen, J. W., Khetani, S. R. & Bhatia, S. N. In Vitro Zonation and Toxicity in a Hepatocyte Bioreactor. *Toxicol. Sci.* **84,** 110–119 (2005).

164. Jang, K.-J. & Suh, K.-Y. A multi-layer microfluidic device for efficient culture and analysis of renal tubular cells. *Lab Chip* **10,** 36–42 (2010).

165. Weaver, V. M. *et al.* Reversion of the Malignant Phenotype of Human Breast Cells in Three-Dimensional Culture and In Vivo by Integrin Blocking Antibodies. *J. Cell Biol.* **137,** 231 –245 (1997).

166. Streuli, C. H. Control of mammary epithelial differentiation: basement membrane induces tissue-specific gene expression in the absence of cell-cell interaction and morphological polarity. *J. Cell Biol.* **115,** 1383–1395 (1991).

167. Hwang, N. S. *et al.* Effects of three-dimensional culture and growth factors on the chondrogenic differentiation of murine embryonic stem cells. *Stem Cells* **24,** 284–91 (2006).

168. Streuli, C. Extracellular matrix remodelling and cellular differentiation. *Curr. Opin. Cell Biol.* **11,** 634–640 (1999).

169. Fischer, A. R., Elliot, H., Waterman, C. & Danuser, G. Myosin II Controls Cellular Branching Morphogenesis and Migration in 3D by Minimizing Plasma Membrane Curvature. *Biophys. J.* **106,** (2014).

170. Petrie, R. J., Gavara, N., Chadwick, R. S. & Yamada, K. M. Nonpolarized signaling reveals two distinct modes of 3D cell migration. *J. Cell Biol.* **197,** 439–455 (2012).

171. Griffith, L. G. & Swartz, M. A. Capturing complex 3D tissue physiology in vitro. *Nat Rev Mol Cell Biol* **7,** 211–224 (2006).

172. Muthuswamy, S. K. 3D culture reveals a signaling network. *Breast Cancer Res.* **13,** 103 (2011).

173. Li, S. *et al.* Genomic analysis of smooth muscle cells in 3-dimensional collagen matrix. *FASEB J.* **17,** 97–9 (2003).

174. Meshel, A. S., Wei, Q., Adelstein, R. S. & Sheetz, M. P. Basic mechanism of three-dimensional collagen fibre transport by fibroblasts. *Nat. Cell Biol.* **7,** 157–64 (2005).

175. Bornens, M. Organelle positioning and cell polarity. *Nat. Rev. Mol. Cell Biol.* **9,** 874–86 (2008).

176. Gardel, M. L. *et al.* Prestressed F-actin networks cross-linked by hinged filamins replicate mechanical properties of cells. *Proc. Natl. Acad. Sci. U. S. A.* **103,** 1762–7 (2006).

177. Kasza, K. E. *et al.* Filamin A is essential for active cell stiffening but not passive stiffening under external force. *Biophys. J.* **96,** 4326–35 (2009).

178. Lynch, C. D. *et al.* Filamin depletion blocks endoplasmic spreading and destabilizes force-bearing adhesions. *Mol. Biol. Cell* **22,** 1263–73 (2011).

179. Tinevez, J.-Y. *et al.* Role of cortical tension in bleb growth. *Proc. Natl. Acad. Sci. U. S. A.* **106,** 18581–6 (2009).

180. Ramakrishnan, N., Sunil Kumar, P. B. & Radhakrishnan, R. Mesoscale computational studies of membrane bilayer remodeling by curvature-inducing proteins. *Phys. Rep.* **543,** 1–60 (2014).

181. Liu, J., Tourdot, R., Ramanan, V., Agrawal, N. J. & Radhakrishanan, R. Mesoscale simulations of curvature-inducing protein partitioning on lipid bilayer membranes in the presence of mean curvature fields. *Mol. Phys.* **110,** 1127–1137 (2012).

182. Zhao, Y. *et al.* Exo70 generates membrane curvature for morphogenesis and cell migration. *Dev. Cell* **26,** 266–78 (2013).

183. Morishige, M. *et al.* GEP100 links epidermal growth factor receptor signalling to Arf6 activation to induce breast cancer invasion. *Nat. Cell Biol.* **10,** 85–92 (2008).

184. Liu, H., Radisky, D. C., Wang, F. & Bissell, M. J. Polarity and proliferation are controlled by distinct signaling pathways downstream of PI3-kinase in breast epithelial tumor cells. *J. Cell Biol.* **164,** 603–612 (2004).

185. Friedland, J. C. *et al.* α6β4 integrin activates Rac-dependent p21-activated kinase 1 to drive NF-κB-dependent resistance to apoptosis in 3D mammary acini. *J. Cell Sci.* **120,** 3700–3712 (2007).

186. Donaldson, J. G. & Jackson, C. L. ARF family G proteins and their regulators: roles in membrane transport, development and disease. *Nat. Rev. Mol. Cell Biol.* **12,** 362–75 (2011).

187. Lundmark, R., Doherty, G. J., Vallis, Y., Peter, B. J. & McMahon, H. T. Arf family GTP loading is

activated by, and generates, positive membrane curvature. *Biochem. J.* **414,** 189–94 (2008).

188.   Paszek, M. J. *et al.* Tensional homeostasis and the malignant phenotype. *Cancer Cell* **8,** 241–254 (2005).

189.   Przybyla, L., Lakins, J. N., Sunyer, R., Trepat, X. & Weaver, V. M. Monitoring developmental force distributions in reconstituted embryonic epithelia. *Methods* **94,** 101–13 (2015).

190.   Tseng, Q. *et al.* Spatial organization of the extracellular matrix regulates cell-cell junction positioning. *Proc. Natl. Acad. Sci. U. S. A.* **109,** 1506–11 (2012).

191.   Hutter, J. L. & Bechhoefer, J. Calibration of atomic-force microscope tips. *Rev. Sci. Instrum.* **64,** 1868 (1993).

192.   Discher, D. E., Janmey, P. & Wang, Y. Tissue Cells Feel and Respond to the Stiffness of Their Substrate. *Science (80-.).* **310,** 1139–1143 (2005).

193.   Stylianopoulos, T. *et al.* Causes, consequences, and remedies for growth-induced solid stress in murine and human tumors. *Proc. Natl. Acad. Sci. U. S. A.* **109,** 15101–8 (2012).

194.   Stylianopoulos, T. *et al.* Coevolution of solid stress and interstitial fluid pressure in tumors during progression: implications for vascular collapse. *Cancer Res.* **73,** 3833–41 (2013).

195.   Paszek, M. J. *et al.* Tensional homeostasis and the malignant phenotype. *Cancer Cell* **8,** 241–254 (2005).

196.   Fernández-Sánchez, M. E. *et al.* Mechanical induction of the tumorigenic β-catenin pathway by tumour growth pressure. *Nature* **523,** 92–95 (2015).

197.   Mouw, J. K. *et al.* Tissue mechanics modulate microRNA-dependent PTEN expression to regulate malignant progression. *Nat. Med.* **20,** 360–7 (2014).

198.   Huang, S. & Ingber, D. E. Cell tension, matrix mechanics, and cancer development. *Cancer Cell* **8,** 175–6 (2005).

199.   Hanahan, D. & Weinberg, R. A. The Hallmarks of Cancer. *Cell* **100,** 57–70 (2000).

200.   Hanahan, D. & Weinberg, R. A. Hallmarks of Cancer: The Next Generation. *Cell* **144,** 646–674 (2011).

201. Hynes, R. O. Integrins: versatility, modulation, and signaling in cell adhesion. *Cell* **69,** 11–25 (1992).

202. Zhao, J. & Guan, J.-L. Signal transduction by focal adhesion kinase in cancer. *Cancer Metastasis Rev.* **28,** 35–49 (2009).

203. Samuel, M. S. *et al.* Actomyosin-mediated cellular tension drives increased tissue stiffness and β-catenin activation to induce epidermal hyperplasia and tumor growth. *Cancer Cell* **19,** 776–91 (2011).

204. Rubashkin, M. G. *et al.* Force engages vinculin and promotes tumor progression by enhancing PI3K activation of phosphatidylinositol (3,4,5)-triphosphate. *Cancer Res.* **74,** 4597–611 (2014).

205. Su, T. T. & O'Farrell, P. H. Size control: Cell proliferation does not equal growth. *Curr. Biol.* **8,** R687–R689 (1998).

206. Schrader, J. *et al.* Matrix stiffness modulates proliferation, chemotherapeutic response, and dormancy in hepatocellular carcinoma cells. *Hepatology* **53,** 1192–205 (2011).

207. Klein, E. A. *et al.* Cell-cycle control by physiological matrix elasticity and in vivo tissue stiffening. *Curr. Biol.* **19,** 1511–8 (2009).

208. Delarue, M. *et al.* Compressive stress inhibits proliferation in tumor spheroids through a volume limitation. *Biophys. J.* **107,** 1821–8 (2014).

209. Akimoto, S., Mitsumata, M., Sasaguri, T. & Yoshida, Y. Laminar Shear Stress Inhibits Vascular Endothelial Cell Proliferation by Inducing Cyclin-Dependent Kinase Inhibitor p21Sdi1/Cip1/Waf1. *Circ. Res.* **86,** 185–190 (2000).

210. Riddle, R. C., Taylor, A. F., Genetos, D. C. & Donahue, H. J. MAP kinase and calcium signaling mediate fluid flow-induced human mesenchymal stem cell proliferation. *Am. J. Physiol. Cell Physiol.* **290,** C776–84 (2006).

211. Ueba, H., Kawakami, M. & Yaginuma, T. Shear Stress as an Inhibitor of Vascular Smooth Muscle Cell Proliferation : Role of Transforming Growth Factor- 1 and Tissue-Type Plasminogen Activator. *Arterioscler. Thromb. Vasc. Biol.* **17,** 1512–1516 (1997).

212. Collins, K., Jacks, T. & Pavletich, N. P. The cell cycle and cancer. *Proc. Natl. Acad. Sci.* **94,** 2776–2778 (1997).

213. Norbury, C. & Nurse, P. Animal Cell Cycles and Their Control. *Annu. Rev. Biochem.* **61,** 441–468 (1992).

214. Hunter, T. & Pines, J. Cyclins and cancer. II: Cyclin D and CDK inhibitors come of age. *Cell* **79,** 573–82 (1994).

215. Assoian, R. K. & Klein, E. A. Growth control by intracellular tension and extracellular stiffness. *Trends Cell Biol.* **18,** 347–352 (2008).

216. Schwartz, M. A. & Assoian, R. K. Integrins and cell proliferation: regulation of cyclin-dependent kinases via cytoplasmic signaling pathways. *J. Cell Sci.* **114,** 2553–60 (2001).

217. Bae, Y. H. *et al.* A FAK-Cas-Rac-lamellipodin signaling module transduces extracellular matrix stiffness into mechanosensitive cell cycling. *Sci. Signal.* **7,** ra57 (2014).

218. Oktay, M., Wary, K. K., Dans, M., Birge, R. B. & Giancotti, F. G. Integrin-mediated activation of focal adhesion kinase is required for signaling to Jun NH2-terminal kinase and progression through the G1 phase of the cell cycle. *J. Cell Biol.* **145,** 1461–9 (1999).

219. Lopez-Bergami, P. *et al.* Rewired ERK-JNK signaling pathways in melanoma. *Cancer Cell* **11,** 447–60 (2007).

220. Dow, L. E. *et al.* Apc Restoration Promotes Cellular Differentiation and Reestablishes Crypt Homeostasis in Colorectal Cancer. *Cell* **161,** 1539–1552 (2015).

221. Conacci-Sorrell, M., Zhurinsky, J. & Ben-Ze'ev, A. The cadherin-catenin adhesion system in signaling and cancer. *J. Clin. Invest.* **109,** 987–991 (2002).

222. Morin, P. J. beta-catenin signaling and cancer. *Bioessays* **21,** 1021–30 (1999).

223. Benham-Pyle, B. W., Pruitt, B. L. & Nelson, W. J. Mechanical strain induces E-cadherin-dependent Yap1 and -catenin activation to drive cell cycle entry. *Science (80-.).* **348,** 1024–1027 (2015).

224. Whitehead, J. *et al.* Mechanical factors activate beta-catenin-dependent oncogene expression in APC mouse colon. *HFSP J.* **2,** 286–94 (2008).

225. Samuel, M. S. *et al.* Actomyosin-mediated cellular tension drives increased tissue stiffness and β-catenin activation to induce epidermal hyperplasia and tumor growth. *Cancer Cell* **19,** 776–91 (2011).

226. Ocadiz, R., Sauceda, R., Cruz, M., Graef, A. M. & Gariglio, P. High correlation between molecular alterations of the c-myc oncogene and carcinoma of the uterine cervix. *Cancer Res.* **47,** 4173–7 (1987).

227. Pérez-Roger, I., Solomon, D. L., Sewing, A. & Land, H. Myc activation of cyclin E/Cdk2 kinase involves induction of cyclin E gene transcription and inhibition of p27(Kip1) binding to newly formed complexes. *Oncogene* **14,** 2373–81 (1997).

228. Lam, W. A. *et al.* Extracellular matrix rigidity modulates neuroblastoma cell differentiation and N-myc expression. *Mol. Cancer* **9,** 35 (2010).

229. Coppé, J.-P., Desprez, P.-Y., Krtolica, A. & Campisi, J. The senescence-associated secretory phenotype: the dark side of tumor suppression. *Annu. Rev. Pathol.* **5,** 99–118 (2010).

230. Tam, K. W. *et al.* CDKN2A/p16 inactivation mechanisms and their relationship to smoke exposure and molecular features in non-small-cell lung cancer. *J. Thorac. Oncol.* **8,** 1378–88 (2013).

231. Herman, J. G. *et al.* Inactivation of the CDKN2/p16/MTS1 gene is frequently associated with aberrant DNA methylation in all common human cancers. *Cancer Res.* **55,** 4525–30 (1995).

232. Collado, M. & Serrano, M. Senescence in tumours: evidence from mice and humans. *Nat. Rev. Cancer* **10,** 51–7 (2010).

233. Levine, A. J. & Oren, M. The first 30 years of p53: growing ever more complex. *Nat. Rev. Cancer* **9,** 749–758 (2009).

234. Polager, S. & Ginsberg, D. p53 and E2f: partners in life and death. *Nat. Rev. Cancer* **9,** 738–48 (2009).

235. Rayess, H., Wang, M. B. & Srivatsan, E. S. Cellular senescence and tumor suppressor gene p16. *Int. J. Cancer* **130,** 1715–25 (2012).

236. Levine, A. J. p53, the Cellular Gatekeeper for Growth and Division. *Cell* **88,** 323–331 (1997).

237. Carvajal, L. A., Hamard, P.-J., Tonnessen, C. & Manfredi, J. J. E2F7, a novel target, is up-regulated by p53 and mediates DNA damage-dependent transcriptional repression. *Genes Dev.* **26,** 1533–45 (2012).

238. Aksoy, O. *et al.* The atypical E2F family member E2F7 couples the p53 and RB pathways during cellular senescence. *Genes Dev.* **26,** 1546–57 (2012).

239. Ohtani, N., Yamakoshi, K., Takahashi, A. & Hara, E. The p16INK4a-RB pathway: molecular link between cellular senescence and tumor suppression. *J. Med. Invest.* **51,** 146–53 (2004).

240. Lim, S.-T. *et al.* Nuclear FAK promotes cell proliferation and survival through FERM-enhanced p53 degradation. *Mol. Cell* **29,** 9–22 (2008).

241. Chang, S.-F. *et al.* Tumor cell cycle arrest induced by shear stress: Roles of integrins and Smad. *Proc. Natl. Acad. Sci. U. S. A.* **105,** 3927–32 (2008).

242. Igney, F. H. & Krammer, P. H. Death and anti-death: tumour resistance to apoptosis. *Nat. Rev. Cancer* **2,** 277–88 (2002).

243. Berthelet, J. & Dubrez, L. Regulation of Apoptosis by Inhibitors of Apoptosis (IAPs). *Cells* **2,** 163–87 (2013).

244. YANG, Y. L. & LI, X. M. The IAP family: endogenous caspase inhibitors with multiple biological activities. *Cell Res.* **10,** 169–177 (2000).

245. Rampino, N. Somatic Frameshift Mutations in the BAX Gene in Colon Cancers of the Microsatellite Mutator Phenotype. *Science (80-.).* **275,** 967–969 (1997).

246. Meijerink, J. P. *et al.* Hematopoietic malignancies demonstrate loss-of-function mutations of BAX. *Blood* **91,** 2991–7 (1998).

247. Yin, C., Knudson, C. M., Korsmeyer, S. J. & Van Dyke, T. Bax suppresses tumorigenesis and stimulates apoptosis in vivo. *Nature* **385,** 637–40 (1997).

248. Soengas, M. S. Apaf-1 and Caspase-9 in p53-Dependent Apoptosis and Tumor Inhibition. *Science (80-.).* **284,** 156–159 (1999).

249. Soengas, M. S. *et al.* Inactivation of the apoptosis effector Apaf-1 in malignant melanoma. *Nature*

409, 207–11 (2001).

250. Rufini, A., Tucci, P., Celardo, I. & Melino, G. Senescence and aging: the critical roles of p53. *Oncogene* **32,** 5129–43 (2013).

251. Wang, J. Y. J. Nucleo-cytoplasmic communication in apoptotic response to genotoxic and inflammatory stress. *Cell Res.* **15,** 43–48 (2005).

252. Leight, J. L., Wozniak, M. A., Chen, S., Lynch, M. L. & Chen, C. S. Matrix rigidity regulates a switch between TGF-β1-induced apoptosis and epithelial-mesenchymal transition. *Mol. Biol. Cell* **23,** 781–91 (2012).

253. Van Antwerp, D. J., Martin, S. J., Kafri, T., Green, D. R. & Verma, I. M. Suppression of TNF-alpha -Induced Apoptosis by NF-kappa B. *Science (80-.).* **274,** 787–789 (1996).

254. Khandelwal, N. *et al.* Nucleolar NF-κB/RelA mediates apoptosis by causing cytoplasmic relocalization of nucleophosmin. *Cell Death Differ.* **18,** 1889–903 (2011).

255. Mukhopadhyay, T., Roth, J. A. & Maxwell, S. A. Altered expression of the p50 subunit of the NF-kappa B transcription factor complex in non-small cell lung carcinoma. *Oncogene* **11,** 999–1003 (1995).

256. Beg, A. A. & Baltimore, D. An Essential Role for NF-kappa B in Preventing TNF-alpha -Induced Cell Death. *Science (80-.).* **274,** 782–784 (1996).

257. Bours, V., Dejardin, E., Goujon-Letawe, F., Merville, M. P. & Castronovo, V. The NF-kappa B transcription factor and cancer: high expression of NF-kappa B- and I kappa B-related proteins in tumor cell lines. *Biochem. Pharmacol.* **47,** 145–9 (1994).

258. Karin, M., Cao, Y., Greten, F. R. & Li, Z.-W. NF-kappaB in cancer: from innocent bystander to major culprit. *Nat. Rev. Cancer* **2,** 301–10 (2002).

259. Wipff, P.-J., Rifkin, D. B., Meister, J.-J. & Hinz, B. Myofibroblast contraction activates latent TGF-beta1 from the extracellular matrix. *J. Cell Biol.* **179,** 1311–23 (2007).

260. Wei, S. C. *et al.* Matrix stiffness drives epithelial-mesenchymal transition and tumour metastasis through a TWIST1-G3BP2 mechanotransduction pathway. *Nat. Cell Biol.* **17,** 678–88 (2015).

261. Allen, J. L., Cooke, M. E. & Alliston, T. ECM stiffness primes the TGFβ pathway to promote chondrocyte differentiation. *Mol. Biol. Cell* **23,** 3731–3742 (2012).

262. Ishihara, S. *et al.* Substrate stiffness regulates temporary NF-κB activation via actomyosin contractions. *Exp. Cell Res.* **319,** 2916–27 (2013).

263. Sero, J. E. *et al.* Cell shape and the microenvironment regulate nuclear translocation of NF-κB in breast epithelial and tumor cells. *Mol. Syst. Biol.* **11,** 790 (2015).

264. Weber, G. *et al.* Roles of the RAF/MEK/ERK and PI3K/PTEN/AKT pathways in malignant transformation and drug resistance. *Adv. Enzyme Regul.* **46,** 249–279 (2006).

265. McCubrey, J. A. *et al.* ROLES OF THE RAF/MEK/ERK PATHWAY IN CELL GROWTH, MALIGNANT TRANSFORMATION AND DRUG RESISTANCE. *Biochim. Biophys. Acta* **1773,** 1263–1284 (2007).

266. Mayo, L. D. & Donner, D. B. The PTEN, Mdm2, p53 tumor suppressor–oncoprotein network. *Trends Biochem. Sci.* **27,** 462–467 (2002).

267. Huang, W.-C., Ju, T.-K., Hung, M.-C. & Chen, C.-C. Phosphorylation of CBP by IKKα Promotes Cell Growth by Switching the Binding Preference of CBP from p53 to NF-κB. *Mol. Cell* **26,** 75–87 (2007).

268. Mungamuri, S. K., Yang, X., Thor, A. D. & Somasundaram, K. Survival signaling by Notch1: mammalian target of rapamycin (mTOR)-dependent inhibition of p53. *Cancer Res.* **66,** 4715–24 (2006).

269. Bos, J. L. ras oncogenes in human cancer: a review. *Cancer Res.* **49,** 4682–9 (1989).

270. Boucher, M.-J. *et al.* MEK/ERK signaling pathway regulates the expression of Bcl-2, Bcl-XL, and Mcl-1 and promotes survival of human pancreatic cancer cells. *J. Cell. Biochem.* **79,** 355–369 (2000).

271. Frödin, M. & Gammeltoft, S. Role and regulation of 90 kDa ribosomal S6 kinase (RSK) in signal transduction. *Mol. Cell. Endocrinol.* **151,** 65–77 (1999).

272. Zhang, Z., Vuori, K., Reed, J. C. & Ruoslahti, E. The alpha 5 beta 1 integrin supports survival of

cells on fibronectin and up-regulates Bcl-2 expression. *Proc. Natl. Acad. Sci.* **92,** 6161–6165 (1995).

273. Bowman, T., Garcia, R., Turkson, J. & Jove, R. STATs in oncogenesis. *Oncogene* **19,** 2474–88 (2000).

274. Buettner, R., Mora, L. B. & Jove, R. Activated STAT Signaling in Human Tumors Provides Novel Molecular Targets for Therapeutic Intervention. *Clin. Cancer Res.* **8,** 945–954 (2002).

275. Quaglino, A., Salierno, M., Pellegrotti, J., Rubinstein, N. & Kordon, E. C. Mechanical strain induces involution-associated events in mammary epithelial cells. *BMC Cell Biol.* **10,** 55 (2009).

276. Chaudhuri, O. *et al.* Extracellular matrix stiffness and composition jointly regulate the induction of malignant phenotypes in mammary epithelium. *Nat. Mater.* **13,** 970–8 (2014).

277. Zahir, N. Spatial-mechanical regulation of mammary morphogenesis and therapeutic resistance. (2006).

278. Levental, K. R. *et al.* Matrix Crosslinking Forces Tumor Progression by Enhancing Integrin Signaling. *Cell* **139,** 891–906 (2009).

279. Erler, J. T. *et al.* Lysyl oxidase is essential for hypoxia-induced metastasis. *Nature* **440,** 1222–1226 (2006).

280. Hynes, R. O. Integrins: Bidirectional, Allosteric Signaling Machines. *Cell* **110,** 673–687 (2002).

281. Galbraith, C. G., Yamada, K. M. & Sheetz, M. P. The relationship between force and focal complex development. *J. Cell Biol.* **159,** 695–705 (2002).

282. Chrzanowsk-Wodnicka, M. & Burridge, K. Rho-stimulated contractility drives the formation of stress fibers and focal adhesions. *J. Cell Biol.* **133,** 1403–1415 (1996).

283. Schaller, M. D. *et al.* Autophosphorylation of the focal adhesion kinase, pp125FAK, directs SH2-dependent binding of pp60src. *Mol. Cell. Biol.* **14,** 1680–1688 (1994).

284. Schlaepfer, D. D., Hanks, S. K., Hunter, T. & van der Geer, P. Integrin-mediated signal transduction linked to Ras pathway by GRB2 binding to focal adhesion kinase. *Nature* **372,** 786–791 (1994).

285. Schlaepfer, D. D., Jones, K. C. & Hunter, T. Multiple Grb2-Mediated Integrin-Stimulated Signaling Pathways to ERK2/Mitogen-Activated Protein Kinase: Summation of Both c-Src- and Focal

Adhesion Kinase-Initiated Tyrosine Phosphorylation Events. *Mol. Cell. Biol.* **18,** 2571–2585 (1998).

286. Thomas, J. W. *et al.* SH2- and SH3-mediated Interactions between Focal Adhesion Kinase and Src. *J. Biol. Chem.* **273,** 577–583 (1998).

287. Sackin, H. Stretch-activated ion channels. *Kidney Int* **48,** 1134–1147 (1995).

288. Tomonaga, N. *et al.* Analysis of Intratumor Heterogeneity of EGFR Mutations in Mixed Type Lung Adenocarcinoma. *Clin. Lung Cancer* (2013). doi:10.1016/j.cllc.2013.04.005

289. Kaneda, H., Yoshida, T. & Okamoto, I. Molecularly targeted approaches herald a new era of non-small-cell lung cancer treatment. *Cancer Manag. Res.* **5,** 91–101 (2013).

290. Krawczyk, P. *et al.* Predictive and prognostic factors in second- and third-line erlotinib treatment in NSCLC patients with known status of the EGFR gene. *Oncol. Rep.* (2013). doi:10.3892/or.2013.2553

291. Yamashita-Kashima, Y., Shu, S., Harada, N. & Fujimoto-Ouchi, K. Enhanced antitumor activity of trastuzumab emtansine (T-DM1) in combination with pertuzumab in a HER2-positive gastric cancer model. *Oncol. Rep.* (2013). doi:10.3892/or.2013.2547

292. Matsumoto, S. *et al.* Frequent EGFR mutations in brain metastases of lung adenocarcinoma. *Int. J. Cancer* **119,** 1491–1494 (2006).

293. Gilbertson, R. J. *et al.* ERBB1 Is Amplified and Overexpressed in High-grade Diffusely Infiltrative Pediatric Brain Stem Glioma. *Clin. Cancer Res.* **9,** 3620–3624 (2003).

294. Yarden, Y. & Sliwkowski, M. X. Untangling the ErbB signalling network. *Nat. Rev. Mol. Cell Biol.* **2,** 127–137 (2001).

295. Zhan, L., Xiang, B. & Muthuswamy, S. K. Controlled Activation of ErbB1/ErbB2 Heterodimers Promote Invasion of Three-Dimensional Organized Epithelia in an ErbB1-Dependent Manner: Implications for Progression of ErbB2-Overexpressing Tumors. *Cancer Res.* **66,** 5201–5208 (2006).

296. Citri, A. & Yarden, Y. EGF–ERBB signalling: towards the systems level. *Nat. Rev. Mol. Cell Biol.* **7,** 505–516 (2006).

297. Jackman, D. M. *et al.* Phase II Clinical Trial of Chemotherapy-Naïve Patients ≥ 70 Years of Age

Treated With Erlotinib for Advanced Non–Small-Cell Lung Cancer. *J. Clin. Oncol.* **25,** 760–766 (2007).

298.   Burgos Fuster, L. M. & Sandler, A. B. Select Clinical Trials of Erlotinib (OSI-774) in Non–Small-Cell Lung Cancer with Emphasis on Phase III Outcomes. *Clin. Lung Cancer* **6, Supplem,** S24–S29 (2004).

299.   Voldborg, B. R., Damstrup, L., Spang-Thomsen, M. & Poulsen, H. S. Epidermal growth factor receptor (EGFR) and EGFR mutations, function and possible role in clinical trials. *Ann. Oncol.* **8,** 1197–1206 (1997).

300.   Moy, B. & Goss, P. E. Lapatinib: Current Status and Future Directions in Breast Cancer. *Oncologist* **11,** 1047–1057 (2006).

301.   Ahmad, Z. K., Brown, C. M., Cueva, R. A., Ryan, A. F. & Doherty, J. K. ErbB expression, activation, and inhibition with lapatinib and tyrphostin (AG825) in human vestibular schwannomas. *Otol. Neurotol. Off. Publ. Am. Otol. Soc. Am. Neurotol. Soc. [and] Eur. Acad. Otol. Neurotol.* **32,** 841–847 (2011).

302.   Spector, N. L. *et al.* Study of the Biologic Effects of Lapatinib, a Reversible Inhibitor of ErbB1 and ErbB2 Tyrosine Kinases, on Tumor Growth and Survival Pathways in Patients With Advanced Malignancies. *J. Clin. Oncol.* **23,** 2502–2512 (2005).

303.   McHugh, L. A. *et al.* Lapatinib, a dual inhibitor of ErbB-1/-2 receptors, enhances effects of combination chemotherapy in bladder cancer cells. *Int. J. Oncol.* **34,** 1155–1163 (2009).

304.   Kim, J.-H. & Asthagiri, A. R. Matrix stiffening sensitizes epithelial cells to EGF and enables the loss of contact inhibition of proliferation. *J. Cell Sci.* **124,** 1280–1287 (2011).

305.   Linardou, H., Dahabreh, I. J., Bafaloukos, D., Kosmidis, P. & Murray, S. Somatic EGFR mutations and efficacy of tyrosine kinase inhibitors in NSCLC. *Nat. Rev. Clin. Oncol.* **6,** 352–366 (2009).

306.   Schmidt, M. H. H., Furnari, F. B., Cavenee, W. K. & Bogler, O. Epidermal growth factor receptor signaling intensity determines intracellular protein interactions, ubiquitination, and internalization. *Proc. Natl. Acad. Sci. U. S. A.* **100,** 6505–6510 (2003).

307.   Haugh, J. M., Schooler, K., Wells, A., Wiley, H. S. & Lauffenburger, D. A. Effect of Epidermal Growth Factor Receptor Internalization on Regulation of the Phospholipase C-γ1 Signaling Pathway. *J. Biol. Chem.* **274,** 8958–8965 (1999).

308.   Goh, L. K., Huang, F., Kim, W., Gygi, S. & Sorkin, A. Multiple mechanisms collectively regulate clathrin-mediated endocytosis of the epidermal growth factor receptor. *J. Cell Biol.* **189,** 871–883 (2010).

309.   Caswell, P. T. *et al.* Rab-coupling protein coordinates recycling of α5β1 integrin and EGFR1 to promote cell migration in 3D microenvironments. *J. Cell Biol.* **183,** 143–155 (2008).

310.   Engler, A. J., Sen, S., Sweeney, H. L. & Discher, D. E. Matrix Elasticity Directs Stem Cell Lineage Specification. *Cell* **126,** 677–689 (2006).

311.   Paszek, M. J. *et al.* Tensional homeostasis and the malignant phenotype. *Cancer Cell* **8,** 241–254 (2005).

312.   Butcher, D. T., Alliston, T. & Weaver, V. M. A tense situation: forcing tumour progression. *Nat. Rev. Cancer* **9,** 108–22 (2009).

313.   Zhang, Y.-H., Zhao, C.-Q., Jiang, L.-S. & Dai, L.-Y. Substrate stiffness regulates apoptosis and the mRNA expression of extracellular matrix regulatory genes in the rat annular cells. *Matrix Biol.* **30,** 135–44 (2011).

314.   Welsh, C. F. *et al.* Timing of cyclin D1 expression within G1 phase is controlled by Rho. *Nat. Cell Biol.* **3,** 950–957 (2001).

315.   Price, L. S., Leng, J., Schwartz, M. A. & Bokoch, G. M. Activation of Rac and Cdc42 by Integrins Mediates Cell Spreading. *Mol. Biol. Cell* **9,** 1863–1871 (1998).

316.   Thakar, R. G. *et al.* Contractility-Dependent Modulation of Cell Proliferation and Adhesion by Microscale Topographical Cues. *Small* **4,** 1416–1424 (2008).

317.   Burdick, J. A. & Prestwich, G. D. Hyaluronic Acid Hydrogels for Biomedical Applications. *Adv. Mater.* **23,** H41–H56 (2011).

318.   Shroff, H., Galbraith, C. G., Galbraith, J. A. & Betzig, E. Live-cell photoactivated localization

microscopy of nanoscale adhesion dynamics. *Nat. Methods* **5,** 417–23 (2008).

319. Paszek, M. J. *et al.* The cancer glycocalyx mechanically primes integrin-mediated growth and survival. *Nature* **511,** 319–25 (2014).

320. Doksani, Y., Wu, J. Y., de Lange, T. & Zhuang, X. Super-resolution fluorescence imaging of telomeres reveals TRF2-dependent T-loop formation. *Cell* **155,** 345–56 (2013).

321. Paszek, M. J. *et al.* Scanning angle interference microscopy reveals cell dynamics at the nanoscale. *Nat. Methods* **9,** 825–7 (2012).

322. Lambacher, A. & Fromherz, P. Fluorescence interference-contrast microscopy on oxidized silicon using a monomolecular dye layer. *Appl. Phys. A* **63,** 207–216 (1996).

323. Ajo-Franklin, C. M., Ganesan, P. V & Boxer, S. G. Variable incidence angle fluorescence interference contrast microscopy for z-imaging single objects. *Biophys. J.* **89,** 2759–69 (2005).

324. Gutierrez, E. *et al.* High Refractive Index Silicone Gels for Simultaneous Total Internal Reflection Fluorescence and Traction Force Microscopy of Adherent Cells. *PLoS One* **6,** e23807 (2011).

325. Koschwanez, J. H., Carlson, R. H. & Meldrum, D. R. Thin PDMS films using long spin times or tert-butyl alcohol as a solvent. *PLoS One* **4,** e4572 (2009).

326. Schindelin, J. *et al.* Fiji: an open-source platform for biological-image analysis. *Nat. Methods* **9,** 676–82 (2012).

327. Levental, I., Georges, P. C. & Janmey, P. A. Soft biological materials and their impact on cell function. *Soft Matter* **3,** 299–306 (2007).

328. Katsidis, C. C. & Siapkas, D. I. General transfer-matrix method for optical multilayer systems with coherent, partially coherent, and incoherent interference. *Appl. Opt.* **41,** 3978–87 (2002).

329. Kanchanawong, P. *et al.* Nanoscale architecture of integrin-based cell adhesions. *Nature* **468,** 580–4 (2010).

330. Schermelleh, L., Heintzmann, R. & Leonhardt, H. A guide to super-resolution fluorescence microscopy. *J. Cell Biol.* **190,** 165–75 (2010).

331. Huang, B., Wang, W., Bates, M. & Zhuang, X. Three-dimensional super-resolution imaging by

stochastic optical reconstruction microscopy. *Science* **319,** 810–3 (2008).

332. Wildanger, D., Medda, R., Kastrup, L. & Hell, S. W. A compact STED microscope providing 3D nanoscale resolution. *J. Microsc.* **236,** 35–43 (2009).

333. D'Souza, R. C. J. *et al.* Time-resolved dissection of early phosphoproteome and ensuing proteome changes in response to TGF-β. *Sci. Signal.* **7,** rs5 (2014).

APPENDIX 1: AN IMAGE-PROCESSING PIPELINE FOR ADHESIONS AND NUCLEAR LOCALIZATION OF PROTEINS

SUMMARY:

Adhesions runs "process_imgages.py" as its main module process_images.py should be run from the command line or in an IDE that allows entering arguments.

example run:

python process_images.py '/home/exampledata/cell1/' cell1 _c .tif '/home/randomdir/csvs/'

DETAILED INSTRUCTIONS:

This code is setup to process an entire data set of time series images, for each time point of which a stack of size "num" was taken

Arguments:

It takes five arguments:

##directory## -- where images should be -- that is, if there are images c1.tif, c2.tif, etc at

/home/dir/images/cell1/t1/cell1t1_c1.tif,/home/dir/images/c2.tif...,

home_dir = '/home/dir/images/cell1/'

##dataset##--which identifies the label for the data set being processed; it assumes that there is a naming scheme for each image that includes the dataset name, then the subfolder name under which the image is stored--in our example, dataset = 'cell1'

##basename## -- in our example, this would be '_c'; it is whatever identifier might be added onto dataset+subfolder, like NIS elements does when collecting stacks

an optional "##num##" -- the default is 25 images in the stack

##heightsdir## -- directory where a set of csvs, corresponding to each time point, are stored. There's given to where this directory might be because it often happens that we process our adhesion heights in a completely separate workflow. so it's not tied to be under the same home directory as the images themselves.

Dependencies:

numpy

scipy

PIL (Image, matplotlib)

mahotas and pymorph-- available through easy_install or pip, on PyPI

--these are well documented computer vision libraries

https://pypi.python.org/pypi/pymorph

https://pypi.python.org/pypi/mahotas/1.0.3

can   also   be   installed   from   source,   see   instructions:

http://mahotas.readthedocs.org/en/latest/

Python version used: 2.7.3

(as long as it's not Python 3.x, it's fine)

run with EPD (Enthought Python Distribution) v7.3.2--had buffer overflow issues with python2.7

development done in Ubuntu 12.04 'Precise Pangolin', IDE = Eclipse
v3.7.2, pydev through Aptana

Modules

ImageStackgou.py sets up classes Image and ImageStack (with initials at
the end for disambiguation), which represent single images and a stack
of images, respectively.

****

zproject.py takes a stack of images and "z-projects" them into a single
tif image, per ImageJ/FIJI's average intensity algorithm, where all
values for a given pixel in a stack are added and averaged over the
number of slices in the stack.

scroll   down   to   'z   project':
http://rsb.info.nih.gov/ij/docs/menus/image.html#stacks

****

segmentation_watershed.py uses the implementation of the Watershed
algorithm in pymorph to identify individual segments (in our case
adhesions) in the zprojected image. It applies a Gaussian filter first
to smooth out some features. It basically convolves the input signal
with the Gaussian distribution and is used to reduce noise.

See more information:

http://en.wikipedia.org/wiki/Watershed_%28image_processing%29

http://en.wikipedia.org/wiki/Gaussian_filter   and

http://docs.scipy.org/doc/scipy-

0.7.x/reference/generated/scipy.ndimage.filters.gaussian_filter.html

segmentation_watershed.py returns an ndarray with the same dimensions
as the input image. At every location (corresponding to every pixel)
there is either a '0' or a number corresponding to which segment the
pixel is determined to belong to.

****

tabulate_adh_props.py compares the output of the segmentation with a
heights csv that is formatted the same, but has values corresponding
with adhesion protein height--calculated in another program. It
populates a new ndarray with height values only at places where there
was a height value and a segment number assignment. It also groups
segment heights together to calculate the average adhesion height.

It returns the cross-referenced heights array as well as average adhesion
height values and adhesion size (pixel count).

****

histogram.py plots the average adhesion heights in a histogram and saves
it as a .png file in the corresponding time point folder.

****

readcsv.py and readwrite_file.py are utilities that read and write csvs and txt files.

****

compile_files.py is a utility that goes into a directory and assumes there are two layers of subfolders. It runs through all the files and collects all files that contain a given "keyword" (usually used to identify an extension type) into the topmost folder.

****

ImageStackgou.py

```python
'''
Created on Dec 10, 2013

@author: gou

sets up classes Image_gou and Stack_gou, which represent images and a stack
of multiple images from a given folder

stack pulls a set of images, number 1 through stacknum, from a given
directory, that all share a "basename" and image_extension

it is initialized with the directory, number of images in the stack,
basename, and imageextension


'''
import Image as im
import numpy as np
import matplotlib.pyplot as plt


class Image_gou(object):
    def __init__(self, imagelocation):
        self.directory = imagelocation
        self.name = self.directory
        #import the image pixel information as an numpy array
        #convert L -- greyscale
        self.array = plt.imread(imagelocation, format ='tif')
        self.image = im.open(imagelocation)
        self.size = self.image.size
    def __str__(self):
        return str(self.directory)


class Stack_gou(object):

    def __init__(self, directory, num, basename, imageext):
        self.directory = directory
        self.stacksize = num
        self.basename = basename
        self.images = []

        for i in range(num-1):
            num = str(i+1)
            img = Image_gou(directory+basename+num+imageext)
            self.images.append(img)

    def __str__(self):
        res=[]
        for image in self.images:
                res.append(str(image))
```

```python
        return '\n'.join(res)

    def add_image(self, image):
        #image needs to be an instance of Image_gou
        self.images.append(image)

    def access_slice(self, slicenum):
        return self.images[slicenum]
```

process_images.py

```
'''
Created on Dec 4, 2013

@author: gou
'''

import sys
from ImageStackgou import *
import Image
import zproject as zp
import segmentation_watershed as seg_wt
import readwrite_file as rd_wrt
import tabulate_adh_props as adh_p
import histogram as hist
import os
import compile_files as compilef
import draw_segment_image as draw
import re

def processStack(home_dir, basename, imageext, heightsdir, num = None):
    if num is None:
        num = 25
    #populate the stack based on the provided directory, basename, number of
images per stack, and their image extension
    stack=Stack_gou(home_dir, num, basename, imageext)
    #calls zproject to produce an average-intensity value for the stack
    zprojected =  zp.zproject(stack)
    #saves this image
    name =home_dir+basename+'_zprojected'+imageext

    plt.imsave(name, zprojected)

    #converts zprojected image to greyscale in preparation for segmentation
    image=Image.open(name).convert('L')
    #implements watershed segmentation from the mahotas/pymorph computer
vision library
    #*after contrast enhancement and gaussian blurring -- can change

    #add option = 'contrast' if want to run contrast enhancement on image
before processing
    #otherwise there will only be Gaussian filtering
    print 'about to segment'
    adhesions_array_labels, num_adhesions=seg_wt.segmentation(image,
home_dir, basename)

    #the output of segmentation is a csv of numbers corresponding with pixels
in the original image
    #if a pixel was found to belong to a segment, or adhesion
    #it was a number that groups with all other pixels in that adhesion
    #if not, it will have a value of 0
    rd_wrt.writecsv(adhesions_array_labels,home_dir, 'adhesion_nums.csv')
    heights_array = rd_wrt.readcsv(heightsdir + basename+'H.csv')

    #runs compare heights and adhesion segments
```

```python
    #basically cross-checks between two csvs, one with numbers corresponding
to the segmented adhesion number
    #one with heights from imaging data
    #if there is a value for a pixel in both csvs
    #it is recorded and entered into a new array
    #heights for each set of pixels belonging to a segmented adhesion are
collected and averaged
    #to find adhesion averaged heights
    #this is saved into adh_avg_heights
    #avg_heights saves all these heights in a list, to be graphed later
    print 'checking heights with segmented adhesions'
    segmented_heights_array, avg_heights, adh_avg_heights,
new_adhesions_segment_array =
adh_p.comp_heights_segments(adhesions_array_labels, heights_array,
minAdh_size=1)

    #writes a csv of the heights data that only shows heights where an
adhesion was found
    #in the segmentation
    rd_wrt.writecsv(segmented_heights_array, home_dir,
'segmented_heights.csv')


    rd_wrt.writecsv(new_adhesions_segment_array, home_dir,
'new_adh_segm.csv')

    #writes a csv that has the following columns:
    #adhesion number--based on the segmentation
    #adhesion size (pixel number)
    #height from Scanning Angle Interference Microscopy data
    rd_wrt.writecsv(adh_avg_heights, home_dir, 'avg_heights.csv')


    #produces a histogram of average adhesion heights
    hist.histogram(avg_heights, home_dir, basename)

    csv=rd_wrt.readcsv('new_adh_segm.csv')
    png_output_name = home_dir+basename+'adhesions'+'.bmp'
    draw.makeImage(png_output_name, csv, scalingFactor = 2)

def main():
    if len(sys.argv)<6:
        print 'not enough inputs--please enter source directory, data set
name, base filename,  image extension, and heights directory\nfor example:
"/home/Documents/Images/", cell1, _c, .tif, /home/Documents/Images/'
        sys.exit()
    elif len(sys.argv)>6:
        print 'too many inputs, only used first five'

    home_dir=sys.argv[1]
    dataset = sys.argv[2]
    basename = sys.argv[3]
    imageext = sys.argv[4]
    heightsdir = sys.argv[5]

    folders = os.listdir(home_dir)
```

```python
        #cycles through folders and analyzes each stack within the subfolders
        for folder in folders:
            #practical processes to get the right directory to feed into
processStack
            directory = home_dir + folder + '/'
            newbasename = dataset +folder+basename
            new_heightsdir = heightsdir + dataset+'/'+folder+'/'
            print 'processing ' + newbasename + ' in ' + new_heightsdir

            processStack(directory, newbasename, imageext, new_heightsdir)


        #compilef.move(home_dir,'histogram', home_dir)

if __name__ == '__main__':
    main()
```

compile_files.py

```python
'''
Created on Dec 12, 2013

@author: gou
'''


import sys
import shutil
import os

def move(home_dir,keyword, new_dir):

    #pulls the filenames of all files and folders within the given directory
    folders = os.listdir(home_dir)
    print folders
    for folder in folders:
        if '.' in folder:
            continue
        else:
            files=os.listdir(home_dir+folder+"/")
            for file in files:
                if keyword in file:
                    current = home_dir+folder+"/"+file
                    new = new_dir+folder+"_"+file
                    #print file
                    shutil.copy(current,new)
    return 1
```

readcsv.py

```python
'''
Created on Dec 10, 2013

@author: gou
'''
import numpy as np
def readcsv(filename):
    print filename
    f=open(filename,'rb')
    lines = f.readlines()
    size =[512,512]
    csv_data= np.zeros(size)

    #enumerate numbers the lines, the 1 specifies that n starts at 1 instead
of 0
    for n, line in enumerate(lines, 1):

        #strips away the \n delimiter at end of each line that makes a new
line
        lineagain = line.rstrip()
        #uses ',' as delimiter to separate out the relevant information
        line_split = lineagain.split(',')
        csv_data [n-1,:] = line_split

    return csv_data
```

readwrite_file.py

```
'''
Created on Dec 11, 2013

@author: gou
'''
import os
import csv
import numpy as np

def readcsv(filename):
    print filename
    f=open(filename,'rb')
    lines = f.readlines()
    size =[512,512]
    csv_data= np.zeros(size)

    #enumerate numbers the lines, the 1 specifies that n starts at 1 instead
of 0
    for n, line in enumerate(lines, 1):

        #strips away the \n delimiter at end of each line that makes a new
line
        lineagain = line.rstrip()
        #uses ',' as delimiter to separate out the relevant information
        line_split = lineagain.split(',')
        csv_data [n-1,:] = line_split

    return csv_data
def writecsv(array,end_dir,outputname):

    #change the directory
    os.chdir(end_dir)
    #open the file
    f = open(outputname, 'wb')
    #create a writer object
    writer = csv.writer(f)

    #iterate through each row of the array and populate a matrix
    #corresponding to the data in the array
    for i in range(len(array)):
        writer.writerow(array[i,:])
    return 1

def writetxt(array, end_dir, outputname):


    return 1
```

segmentation_watershed.py

```python
'''
Created on Dec 11, 2013

@author: gou
'''
import numpy as np
import matplotlib.pyplot as plt
from scipy import ndimage
import pylab
import Image
import mahotas
import ImageEnhance
import pymorph

def segmentation(image, directory, basename, option = None):
    if option != None:

        image=ImageEnhance.Contrast(image)
        image=image.enhance(1.5)
        #enhance contrast by 50%

        #save enhanced image for calling as array later
        image.save(directory+basename+'_zprojected_enhanced.tif')
        image=mahotas.imread(directory+basename+'_zprojected_enhanced.tif')
    else:
        image = image
    #gaussian filter based on sigma (secondar argument), standard deviation
of surrounding pixels
    imagef = ndimage.gaussian_filter(image, 3)
    #OTSU thresholding --cluster based thresholding; minimizes intra-class
variance and maximizes inter-class variance
    #between groups of objects
    #binarizes
    T = mahotas.thresholding.otsu(imagef)
    #count distinct objects in binarized image
    labeled,nr_objects = ndimage.label(imagef > T)

    #generate seeds for Watershed algorithm
    rmax = pymorph.regmax(imagef)
    seeds, nr_adhesion = ndimage.label(rmax)


    #applies distance transform to thresholded image
    #the distance transform labels each pixel with its distance from the
nearest "obstacle"
    #in a binary image, this would be a boundary pixel where the values
change from 0 to 1 or vice versa
    dist=ndimage.distance_transform_edt(imagef>T)
    dist = dist.max()-dist
    dist-=dist.min()
    dist = dist/float(dist.ptp())*255
    dist = dist.astype(np.uint8)
```

```
adhesions = pymorph.cwatershed(dist,seeds)
#pylab.imshow(adhesions)
#pylab.show()
#clears the memory of the opened Figure, so for large data sets, you
don't run out
plt.close()
return adhesions, np.amax(adhesions)
```

tabulate_adh_props.py

```python
'''
Created on Dec 11, 2013

@author: gou
'''
import numpy as np
def comp_heights_segments(segment_array, heights_array, minAdh_size=5):
    size = [512, 512]
    row = size[0]
    column = size[1]
    new_adhesions_segment_array = np.zeros(size)
    segmented_heights_array = np.zeros(size)
    adhesion_array = np.zeros([180000,4])
    #cycle through the segment array and if the value is not zero, go to the
        #heights csv at the same position, and populate the segmented_heights
array with that number
    adh_row=0

    for k in range(row):
        for j in range(column):
            rownum=k
            colnum=j
            if segment_array[rownum,colnum]>0 and
heights_array[rownum,colnum]>0:
                segmented_heights_array[rownum,colnum] = heights_array
[rownum,colnum]
                new_adhesions_segment_array[rownum,
colnum]=segment_array[rownum,colnum]
                #print 'row '+str(rownum+1) +' column ' + str(colnum+1)

                #also populate the 4 column array with adhesion number, row
number, column number
                #print rownum, colnum
                adhesion_array[adh_row,0] = segment_array[rownum,colnum]
                adhesion_array[adh_row,1] = rownum+1
                adhesion_array[adh_row,2] = colnum+1
                adhesion_array[adh_row,3] =
segmented_heights_array[rownum,colnum]

                #increment the row of the adhesion_array that we will be
writing to
                adh_row+=1
            else:
                continue
    adhesion_array = adhesion_array[0:adh_row]

    #pull out the unique adhesions by number using the separate_adhesions
function
    adh_nums= separate_adhesions(adhesion_array,0)

    #creates key for adhesion number to number of pixels in adhesion
    adh_pixel_count = {}

    #creates key for adhesion number to sum of all pixel heights
```

```
    adh_total_height = {}

    #creates key for adhesion number to average height
    adh_avg_heights = {}

    row_count = -1

    #allocate space that will later be populated with the average heights of
each adhesion
    #there are two lists/arrays because the avg_heights list will be used to
generate the histogram
    #the array will be used to output a csv, and is the repository for the
more complete information
    #it includes pixel count and average height for each adhesion number
    adh_avg_heights_array = np.zeros([len(adh_nums),3])
    avg_heights =np.zeros([len(adh_nums),1])


    #cycle through each adhesion number in the unique list we created
    for adh in adh_nums:

        for m in range(adh_row):

            #to deal with the way python treats arrays, we have to pull out
each row separately
            #in order to access individual entries within the row
            #so we cycle through each row individually

            adhesion_row = adhesion_array[m]

            #first we compare the first value to our adhesion number of
interest
            #if they're not the same, we move on
            if adhesion_row[0]!=adh:
                continue

            #if the adhesion number is the same as the adhesion number of the
row (first entry)
            else:

                # if there's already a mapping for this adhesion number
                if adh in adh_pixel_count:

                    #increment pixel count for the adhesion
                    adh_pixel_count[adh]+=1

                    #pull old height number
                    adh_height_total_old = adh_total_height[adh]
                    adh_height_total_new = adh_height_total_old+
adhesion_row[3]
                    adh_total_height[adh]=adh_height_total_new

                #if there isn't a mapping for this adhesion number to pixel
count, which means
                #it's the first time we're encountering it

                else:
```

```
                    #we initialize each mapping
                    adh_pixel_count[adh]=1
                    #the total height is just the height of this one
adhesion, which is the fourth entry in the row
                    #(recall that the row goes: adhesion number, x,y, height)
                    adh_total_height[adh]=adhesion_row[3]

        #we assign the pixel count and total height values so we can operate
on them later
        pixel_count = adh_pixel_count[adh]
        total_height = adh_total_height[adh]

        #use pixel count and heights sum to calculate average height
        adh_avg_heights[adh]=total_height/pixel_count

        #we set a minimum adhesion size, based on pixel count
        #this is defined in the input of this function, and is hard coded in
right now
        if adh_pixel_count[adh]>=minAdh_size:
            #we're keeping track of how many adhesions pass this cutoff
            row_count +=1

            #populating the average heights lists/arrays

            #each array row goes: adhesion number, pixel count, average
height of pixels in adhesion
            adh_avg_heights_array [row_count]= [adh,
adh_pixel_count[adh],adh_avg_heights[adh]]
            #the list is just the average adhesion heights in ascending order
of the adhesion number
            avg_heights[row_count]=[adh_avg_heights[adh]]


    adh_avg_heights_array=adh_avg_heights_array[0:row_count]
    avg_heights = avg_heights[0:row_count]
    #print adh_avg_heights_array
    return segmented_heights_array, avg_heights,
adh_avg_heights_array,new_adhesions_segment_array
def separate_adhesions(array,index):
    #need to hard code the pattern

    #pulling out all the unique adhesion numbers within the adhesion array
    s=set([e[index] for e in array])
    adh_nums= []

    for adh_num in s:
        adh_nums=adh_nums + [adh_num]
    #sorts from smallest to largest
    adh_nums.sort()

    return adh_nums
```

zproject.py

```
'''
Created on Dec 10, 2013

@author: gou
'''
import numpy as np
import scipy
import Image
import math
from scipy import stats
from ImageStackgou import *

def zproject(stack):

    size = stack.stacksize
    img=stack.access_slice(14)
    img_dim1 = int(img.size[0])
    img_dim2 = int(img.size[1])
    sum_array = np.zeros([img_dim1, img_dim2])

    for i in range(size-1):
        img = stack.access_slice(i)
        array = img.array
        sum_array = np.add(sum_array,array)
        i=+1
    averaged_array = sum_array/size
    #averaged_array= averaged_array.astype('uint8')
    return averaged_array
```

histogram.py

```python
'''
Created on Dec 11, 2013

@author: gou
'''
import numpy as np

import matplotlib.pyplot as plt
import pylab
import matplotlib.path as path
import matplotlib.patches as patches
def histogram(array, directory, basename):
#plot histogram
        fig=plt.figure()
        ax = fig.add_subplot(111)

        #we assign the data source (n) and number of bins
        n,bins = np.histogram(array,50)
        left = np.array(bins[:-1])
        right = np.array(bins[1:])
        bottom = np.zeros(len(left))
        top = bottom + n
        XY = np.array([[left,left,right,right], [bottom,top,top,bottom]]).T

        # get the Path object
        barpath = path.Path.make_compound_path_from_polys(XY)

        # make a patch out of it
        patch = patches.PathPatch(barpath, facecolor='blue',
edgecolor='gray', alpha=0.8)
        ax.add_patch(patch)

        # update the view limits
        ax.set_xlim(left[0], right[-1])
        ax.set_ylim(bottom.min(), top.max())

        #save the image
        pylab.savefig(directory+'histogram'+basename+'.png')
```

draw_segment_image.py

```python
'''
Created on Dec 12, 2013

@author: gou
'''
import ImageDraw
import Image
import random
# Create an image from a matrix
# scalingFactor is the scaling factor for the image. For example, 2 will
# create an image twice as big
# minClumpSize is the minimum size of a group of pixels to draw
def makeImage(imgName, matrix, scalingFactor=1, minClumpSize=1):

    # Get the dimensions of the image from the matrix
    height = len(matrix)
    width = len(matrix[0])
    #print height
    #print width

    # Initalize the image with a black background
    img = Image.new('RGB', (scalingFactor*width, scalingFactor*height),
'black')

    # This is the object we'll use to draw onto the image
    draw = ImageDraw.Draw(img)


    # This is a map of all the colors we use
    # For now, we know that 0 (no adhesion) shouldn't be colored
    # We'll fill in this map as we go
    colormap = {0:(0, 0, 0)};

    # This is a map that holds that sum of the x-y position of the pixels,
    # by adhesion value
    # We'll use this later to find the average position of the adhesion
    positions = {}

    # This is a map that simply keeps track of how many pixels were in
    # the adhesion.
    # This is also useful for computing the average position, and also
    # deciding whether or not to draw the adhesion.
    val_n = {}



    # Let's first figure out what clumps are there


    # Iterate over every entry in the matrix
    for x in xrange(height):
        for y in xrange(width):

            # This is the value in the image
```

175

```
            val = matrix[x][y]


            # We don't care about 0's, so if we have a 0, ignore it and move
on
            #if val is 0:
            if val==0:
                #print x,y
                continue

            # If we haven't yet assigned a color for this value, do so now
            if not val in colormap:
                # Construct a random RGB color
                # I'm using a baseline of 100 so that we don't draw black
                # pixels, which would be hard to see on a black background

                #R = 100+random.randint(0, 156)
                #G = 100+random.randint(0, 156)
                #B = 100+random.randint(0, 156)
                #c = int(255*(val-40)/60.0)
                color=int(1000*(val-40)/60)

                #color = (R, G, B)
                #color = (c, c, c)
                print color

                # Store the color in our color for use later
                colormap[val] = color

            # We need to keep track of the positions of all the pixels, so we
can know
            # where to draw the text later
            pos = (x, y)
            if val in val_n:
                # If we already came across this value, increment the count
                # and update the sum of the x and y coordinates accordingly
                val_n[val] += 1

                # Grab the old position from the map, add in the new position
                # by x and y component, and stick it back in the map
                oldPos = positions[val]
                newPos = ( (pos[0]+oldPos[0]), (pos[1]+oldPos[1]) )
                positions[val] = newPos;


            else:
                # Otherwise, create the intial entry

                # This is the first one, so we only have 1 of this value
                val_n[val] = 1
                # This is the only position in the map so far, so just stick
it in
                positions[val] = pos


    #print val_n
    #raw_input()
```

176

```python
    # Now let's go through and actually draw in things
    for x in xrange(height):
        for y in xrange(width):

            # Grab the value at this position
            val = matrix[x][y]

            # We'll only draw something if it's nonzero (so, actually an
adhesion)
            # and it's bigger than the minimum size we're interested in
            if val!=0 and val_n[val] >= minClumpSize:

                # Grab the color we had previously assigned
                color = colormap[val]
                #color = (255,255,255)

                # Generate the box, according to the scaling factor
                # ( (top left corner y x), (bottom right corner y x) )
                # y and x are swapped, because that's how they're drawn
                topLeft = (scalingFactor*y, scalingFactor*x)
                bottomRight = (scalingFactor*(y+1), scalingFactor*(x+1))
                box = (topLeft, bottomRight)

                # Now draw the box that represents this matrix entry
                draw.rectangle(box, fill=1000)

    # Now let's actually label things
    for val in val_n.keys():

        # How many pixels of this value were there?
        n = val_n[val]

        # Only label if we had at least the minimum size
        if n > minClumpSize:
            # Compute the average position of all of the pixels we care about
            pos = positions[val]
            avg_pos = ( scalingFactor*pos[0]/n, scalingFactor*pos[1]/n)

            # Draw the label, with the text just being the adhesion number,
and the
            # position being in the middle of the adhesion itself
            draw.text( (avg_pos[1], avg_pos[0]), str(int(val)))
    # Save the image to the given filename
    img.save(imgName, 'BMP')
    return 1
```

APPENDIX 2: PROTOCOLS

RECYCLING ASSAY FOR ALPHA5 INTEGRIN AND EGFR, FROM J. NORMAN LAB

Solutions:

Ice-cold Ca- and Mg-free PBS.

pH 8.6 buffer for cell-surface reduction:

50ml 1M Tris pH7.5

32ml 3.2M NaCl (X20 saline)

Up to 1 litre with H2O. Correct to pH 8.6 with 10N NaCl (approx 1.77 ml) *after* buffer

has cooled to 4oC.

PBS-T :

PBS with 0.1% T-20 (Make up reasonably fresh and do not leave in bright light)

Citrate/PO4 buffer for ELISA

5.22g Citric Acid

7.2g Na2HPO4 or 8.9g Na2HPO4.2H2O

Correct to pH 5.5

Lysis buffer

200 mM NaCl, 75 mM Tris, 15 mM NaF, 1.5 mM Na_3VO_4, 7.5 mM EDTA and 7.5mM EGTA,

1.5% Triton X-100, 0.75 % Igepal CA-630, 50 μg/ml leupeptin, 50 μg/ml aprotinin and 1mM

4-(2-Aminoethyl)benzynesulphonyl fluoride (AEBSF)

Pre-weigh into universals:

2X 405mg MesNa (one for 1st reduction; one for 2nd reduction)

1X 450 mg IAA

10ml of 5% BSA in PBS-T for blocking ELISA plate

Day before:

Coat ELISA plate. Maxisorb 96 well plates (Life Technologies Inc.) to be coated overnight with 5 μg/ml

anti-human α5 integrin antibodies (use Pharmingen #555651) in 0.05 M Na$_2$CO$_3$ pH 9.6 at 4 °C. 50 ul/well.

Day of assay:

1. Label bottom of plates (not lids!!) with marker pen

2. A typical recycling assay should require 24 X **10cm plates** of cells at approx. 80% confluence. This will

give you the following conditions, and can be numbered as follows:

1 Total

2-3   Blank

4-8   Internal pool

9-12   Recycling point 1

13-16   Recycling point 2

17-20   Recycling point 3

21-24   Recycling point 4

3. Feed cells with prewarmed medium, place in incubator for 30 min-1hr

4. Starve Cells in serum-free medium for 1hr-1.5hr

5. Wash cells X2 with PBS (5ml/plate) on ice.

6. Label cells with sulfo-NHS-SS-Biotin (10mg sulfo-NHS-SS-Biotin/75ml PBS); 3ml per plate. Place on gentle rocker (approx. 7 see-saw movements per minute) in cold room for 30min

7. Wash cells X2 with PBS (5ml/plate) on ice.

8. Allow internalisation. Add 5ml/plate of medium at 12-14ºC (serum-free) to plates 4-24 and incubate for 30 min at 37ºC. Place plates in direct contact with shelve of incubator and not in piles to ensure even temperature distribution. Leave plates 1-3 on ice.

9. Remove medium with sucker. Place cells on ice. Wash cells X1 with PBS (5ml/plate) on ice. Then wash plates 2-24 x1 with pH 8.6 buffer. Suck off. Leave on ice.

10. Add 3 ml pH 8.6 buffer to plates 2-24.

11. Add 26ml pH 8.6 buffer to 405 mg MesNa, then 39 ul 10N NaOH. Mix to dissolve and immediately add 1 ml of this to plates 2-24. Leave plate #1 in PBS on ice or cold room till lysis.

12. Place cells on slow rocker in cold room for 30 min to allow reduction of cell surface label.

13. Wash cells X2 with PBS (5ml/plate) on ice.

14. Leave plates 2-8 on ice. Remove PBS from plates 9-24, add 5ml prewarmed medium (37ºC) and place in incubator for recycling period.

15. At appropriate time remove plates from incubator, suck-off medium, place quickly onto ice and add 5 ml ice-cold PBS.

16. Wash cells X1 with PBS (5ml/plate) on ice. Then wash plates 2-24 x1 with pH 8.6 buffer. Suck off. Leave on ice.

17. Add 3 ml pH 8.6 buffer to plates 2-24.

18. Add 26ml pH 8.6 buffer to 405 mg MesNa (preweighed in Universal), then 39 ul 10N NaOH to this. Mix to dissolve and immediately add 1 ml of this to plates 2-24. Again leave plate #1 in PBS on ice or cold room till lysis; don't reduce plate #1, this is the total!!!

19. Place cells on rocker in cold room for 30 min to allow reduction of cell surface label.

20. Quench reduction reaction by adding 1ml IAA (450 mg/26ml PBS) to each of plates 2-24. Leave for 10-20 mins.

21. At this point block the ELISA plate with 5% BSA in PBS-T

22. Wash all cells X2 with PBS (5ml/plate) on ice.

23. Lyse cells in 120ul/plate lysis buffer.

24. Scrape-off into Eppendorfs and syringe.

25. Spin lysate 13K for 10 min. Remove from pellet into fresh Eppendorf.

26. Remove BSA-block from ELISA plate, wash plate X2 with PBS-T, drain plate.

27. Add 50 ul lysate to each well. Incubate overnight at 4oC

Day after:

Develop ELISA plate:

1. Remove unbound material by extensive washing with PBS-T.

2. Add 50ul streptavidin-conjugated horseradish (1:1K) peroxidase in PBS-T containing 0.1 % BSA for 1 hr at 4 °C.

3. Wash plate again extensively with PBS-T.

4. Wash plate with PBS

5.   Add detection reagent.   Make up fresh; 12.25ml Citrate/PO4 buffer with 9mg orthophenylenediamine.HCl and 2ul H_2O_2 (warm this first in water bath to take the chill off it) at room temperature for 5-20 min as appropriate. Stop the reaction with 8 M H_2SO_4 when it looks done (absorbance of internal pools (4-8) should be easily visible approx. 0.l5-0.25 AU) and read absorbance at 490 nm.

6. Use spread-sheet to calculate results.

Suck-off warm medium before putting cells on ice and then adding ice-cold PBS. This will cool the cells quickly and this is ideal. Don't place plates full of warm medium on ice as this will cool the cells slowly and lead to increased internalisation.

Make up the reduction buffer (ie. Dissolve the MesNa in pH8.6 buffer and add 39ul NaOH) as soon as possible before pippetting this onto the cells.

Some batches of Nunc ELISA plates are dodgy. Try to check the batch first by sticking a primary to the plate and dectecting directly with HRP-secondary.

This assay works well for A2780, HUVEC, NIH and Swiss3T3, H1299 and A431s. Other cell types may need longer reduction periods to effectively remove cell-surface label.

You should aim to run the ELISA under conditions where the integrin is in excess of the integrin-binding capacity of the antibody on the plate (ie. **<u>antibody limiting</u>**). This gives better duplication as small differences in the amount of integrin in the lysate (ie. slightly differing lysate volumes or some integrin degradation) will not affect the signal, as in this way you are measuring is the proportion of integrin biotinylated (not the amount of biotinylated integrin). However, it is possible that certain treatments will cause degradation of integrins which, if extensive, may artifactually read as increase recycling; ie diminution of signal during the recycling period. **To control for this it is important to perform an experiment in which the 2nd reduction step has been omitted.**

When perforing the assay with a new cell-type or a different receptor, it is important to confirm by running the immunoisolates from the ELISA wells on a Western and then blotting with streptavidin-HRP to confirm that the only bands detected are those of interest (ie. in this case alpha5 and beta1).

Sometimes tween-20 can cause problems of poor duplication at the detection stage, particularly if the PBS-T has been made up for some time and left in bright light. To minimise this wash the plate extensively (X3) with PBS (no tween) prior to adding the ortho-phenylenediamine reagent.

Some cell lines (eg certain MEFs) are not particularly adhesive and have a tendency to detach during the course of the assay. We find that using an ice-cold Krebs-based buffer, rather than PBS, keeps them happier and can prevent this from occurring. Recipe: 118mM NaCl, 25mM NaHCO3, 4.8mM KCl, 1.2mM KH2PO4, 1.2mM MgSO4, 11mM Glucose, 1.5mM CaCl2 and 1.5mM sodium pyruvate. This buffer was used during the following steps: #5 (1st wash only), #7, #9 (1st wash only), #13, #15, #16 (1st wash only) and #22

Solutions:

Ice-cold Ca- and Mg-free PBS.

pH 8.6 buffer for cell-surface reduction:

50ml 1M Tris pH7.5

32ml 3.2M NaCl (X20 saline)

Up to 1 litre with H2O. Correct to pH 8.6 with 10N NaCl (approx 1.4 ml) *after* buffer has

cooled to 4oC.

PBS-T :

PBS with 0.1% T-20

ELISA development reagent

25.4 mM Na_2HPO_4, 12.3 mM citric acid, pH 5.4

Lysis buffer

200 mM NaCl, 75 mM Tris, 15 mM NaF, 1.5 mM Na_3VO_4, 7.5 mM EDTA and 7.5mM EGTA,

1.5% Triton X-100, 0.75 % Igepal CA-630, 50 μg/ml leupeptin, 50 μg/ml aprotinin and 1mM

4-(2-Aminoethyl)benzynesulphonyl fluoride (AEBSF)

Pre-weigh into universals:

2X 390mg MesNa (one for 1st reduction; one for 2nd reduction)

1X 442 mg IAA

10ml of 5% BSA in PBS-T for blocking ELISA plate

Day before:

Coat ELISA plate. Maxisorb 96 well plates (Life Technologies Inc.) to be coated overnight with 5 μg/ml

anti-human α5 integrin antibodies (use Pharmingen #555651) in 0.05 M Na_2CO_3 pH 9.6 at 4 °C.

Day of assay:

1. Label bottom of plates (not lids!!) with marker pen

A typical internalisation assay should require 20 X **10cm plates** of cells at approx. 80% confluence. This

will give you the following conditions, and can be numbered as follows:

1-2	*Total*
3-4	*Blank*
5-8	*Internalisation point 1*
9-12	*Internalisation point 2*
13-16	*Internalisation point 3*
17-20	*Internalisation point 4*

2. Block ELISA plate in PBS containing 0.1 % Tween-20 (PBS-T) with 5 % BSA for 1 hour at room

temperature.

3. Feed cells with prewarmed medium, place in incubator for 30 min-1hr

4. Starve Cells in serum-free medium for 30min-1hr

5. Wash cells X2 with PBS (5ml/plate) on ice.

6. Label cells with sulfo-NHS-SS-Biotin (10mg sulfo-NHS-SS-Biotin/75ml PBS); 3ml per plate. Place on gentle rocker (approx. 7 see-saw movements per minute) in cold room for 30min

7. Wash cells X2 with PBS (5ml/plate) on ice.

8. Allow internalisation. Add 5ml/plate of medium (serum-free) to plates 5-20 and incubate for required times. Normally we do 5 and 10 min with and without 0.6 mM primaquine. Place plates in direct contact with shelve of incubator and not in piles to ensure even temperature distribution. Leave plates 1-4 on ice.

9. After required internalisation time remove medium with sucker. Place cells on ice. Wash cells X1 with PBS (5ml/plate) on ice. Then wash plates 3-24 x1 with pH 8.6 buffer. Suck off. Leave on ice.

10. Add 3 ml pH 8.6 buffer to plates 3-24.

11. Add 26ml pH 8.6 buffer to 390 mg MesNa, then 39 ul 10N NaOH. Mix to dissolve and immediately add 1 ml of this to plates 3-24. Leave plates #1and 2 in PBS on ice or cold room till lysis.

12. Place cells on slow rocker in cold room for 30-60 min to allow reduction of cell surface label. After 30-60 min reduction – add 1ml of IAA in PBS to each plate on the rocker, and leave in the cold room for another 10 mins or so.

13. Wash cells X2 with PBS (5ml/plate) on ice.

14. Lyse cells in 100ul/plate lysis buffer.

15. Scrape-off into Eppendorfs and syringe.

16. Spin lysate 13K for 10 min. Remove from pellet into fresh Eppendorf.

17. Remove BSA-block from ELISA plate, wash plate X2 with PBS-T, drain plate.

18. Add 50 ul lysate to each well. Incubate overnight at 4oC

Day after:

Develop ELISA plate:

1. Remove unbound material by extensive washing with PBS-T.

2. Add 50ul streptavidin-conjugated horseradish (1:1K) peroxidase in PBS-T containing 1 % BSA for 1 hr at 4 °C.

3. Wash plate again extensively with PBS-T.

4. Wash plate with PBS

5. Add detection reagent. 0.56 mg/ml ortho-phenylenediamine in a buffer containing 25.4 mM Na_2HPO_4, 12.3 mM citric acid, pH 5.4 with 0.003 % H_2O_2. at room temperature for 5-20 min as appropriate. Stop the reaction with 8 M H_2SO_4 when it looks done (absorbance of total should be approx. 1.0 AU) and read absorbance at 490 nm.

6. Use spread-sheet to calculate results.

NBs

Suck-off warm medium before putting cells on ice and then adding ice-cold PBS. This will cool the cells quickly and this is ideal. Don't place plates full of warm medium on ice as this will cool the cells slowly and lead to increased internalisation.

Make up the reduction buffer (ie. Dissolve the MesNa in pH8.6 buffer and add 39ul NaOH) as soon as possible before pippetting this onto the cells.

Some batches of Nunc ELISA plates are dodgy. Try to check the batch first by sticking a primary to the plate and dectecting directly with HRP-secondary.

This assay works well for A2780, HUVEC, NIH and Swiss3T3, H1299 and A431s. Other cell types may need longer reduction periods to effectively remove cell-surface label.

You should aim to run the ELISA under conditions where the integrin is in excess of the integrin-binding capacity of the antibody on the plate (ie. **<u>antibody limiting</u>**). This gives better duplication as small differences in the amount of integrin in the lysate (ie. slightly differing lysate volumes or some integrin degradation) will not affect the signal, as in this way you are measuring is the proportion of integrin biotinylated (not the amount of biotinylated integrin). However, it is possible that certain treatments will cause degradation of integrins which, if extensive, may artifactually read as increase recycling; ie diminution of signal during the recycling period. **To control for this it is important to perform an experiment in which the 2nd reduction step has been ommitted.**

When perforing the assay with a new cell-type or a different receptor, it is important to confirm by running the immunoisolates from the ELISA wells on a Western and then blotting with streptavidin-HRP to confirm that the only bands detected are those of interest (ie. in this case alpha5 and beta1).

Sometimes tween-20 can cause problems of poor duplication at the detection stage. To minimise this wash the plate extensively with PBS (no tween) prior to adding the ortho-phenylenediamine reagent.

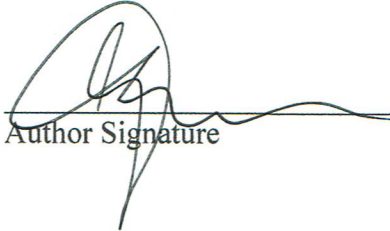*We use these reagents regularly and have validated them for the following applications*

To detect (human)	Recognises	Company (Cat #)	Surface biotinylation/IP/streptavidin blot	ELISA	Western blotting	Immunofluorescence
αvβ3	β3	BD Pharmingen #555752	Yes	Yes	Yes, but only with non-reduced samples	Yes, very good
αvβ5	αvβ5 heterodimer	Chemicon #MAB20192	Yes	Yes	No	Yes
αvβ6	β6	Chemicon #MAB20762	Yes	Yes	?	?
α5β1	α5	BD Pharmingen #555651	Yes	Yes	No	Yes, very good, but doesn't work for IHC
α5β1	α5	BD Transduction Labs #610633	Yes	?	Yes, with reduced samples	Bad for IF, but works really well for IHC
All β1s	β1	BD Transduction Labs #610467	Yes	?	Yes, with reduced samples	Not great
α6	α6 (A&B)	BD Pharmingen #555734	Yes	Yes	?	?
β4	β4	BD Pharmingen #555722	Yes	Yes	?	?
EGFR1	EGFR1	BD Pharmingen #555996	Yes	Yes	No	Yes, very good
EGFR1	EGFR1	BD Transduction Labs #610017	OK	No	Yes, very good	Bad
(mouse)						
αvβ3	β3	Pharmingen #01861D	Yes	Yes	No	Yes (hamster monoclonal; use BD Pharmingen mouse anti-hamster bridging antibody followed by fluorescent anti-mouse)
αv	αv	Pharmingen #01521D	No	No	No	Yes
α5β1	α5	Pharmingen #553319	Yes	Yes	No	Yes (rat monoclonal; use PDPharmingen secondary)

Publishing Agreement

It is the policy of the University to encourage the distribution of all theses, dissertations, and manuscripts. Copies of all UCSF theses, dissertations, and manuscripts will be routed to the library via the Graduate Division. The library will make all theses, dissertations, and manuscripts accessible to the public and will preserve these to the best of their abilities, in perpetuity.

Please sign the following statement:

I hereby grant permission to the Graduate Division of the University of California, San Francisco to release copies of my thesis, dissertation, or manuscript to the Campus Library to provide access and preservation, in whole or in part, in perpetuity.

_____
Author Signature

8/1/16
_____
Date